

ARTIFICIAL MATURATION OF OIL SHALE:
THE IRATI FORMATION FROM THE
PARANÁ BASIN, BRAZIL

by
James L. Gayer

© Copyright by James L. Gayer, 2015

All Rights Reserved

A thesis submitted to the Faculty and the Board of Trustees of the Colorado School of Mines in partial fulfillment of the requirements for the degree of Master of Science (Geophysics).

Golden, Colorado

Date _____

Signed: _____

James L. Gayer

Signed: _____

Dr. Manika Prasad
Thesis Advisor

Golden, Colorado

Date _____

Signed: _____

Dr. Terence K. Young
Professor and Head
Department of Geophysics

ABSTRACT

Oil shale samples from the Irati Formation in Brazil were evaluated from an outcrop block, denoted Block 003. The goals of this thesis include: 1) Characterizing the Irati Formation, 2) Comparing the effects of two different types of pyrolysis, anhydrous and hydrous, and 3) Utilizing a variety of geophysical experiments to determine the changes associated with each type of pyrolysis. Primary work included determining total organic carbon, source rock analysis, mineralogy, computer tomography x-ray scans, and scanning electron microscope images before and after pyrolysis, as well as acoustic properties of the samples during pyrolysis. Two types of pyrolysis (hydrous and anhydrous) were performed on samples cored at three different orientations (0° , 45° , and 90°) with respect to the axis of symmetry, requiring six total experiments. During pyrolysis, the overall effective pressure was maintained at 800 psi, and the holding temperature was 365° . The changes and deformation in the hydrous pyrolysis samples were greater compared to the anhydrous pyrolysis. The velocities gave the best indication of changes occurring during pyrolysis, but it was difficult to maintain the same amplitude and quality of waveforms at higher temperatures. The velocity changes were due to a combination of factors, including thermal deformation of the samples, fracture porosity development, and the release of adsorbed water and bitumen from the sample. Anhydrous pyrolysis in this study did not reduce TOC, while TOC was reduced due to hydrous pyrolysis by 5%, and velocities in the hydrous pyrolysis decreased by up to 30% at 365°C compared to room temperature. Data from this study and future data that can be acquired with the improved high-temperature, high-pressure experiment will assist in future economic production from oil shale at lower temperatures under hydrous pyrolysis conditions.

TABLE OF CONTENTS

ABSTRACT	iii
LIST OF FIGURES	v
LIST OF TABLES	vi
LIST OF SYMBOLS	vii
LIST OF ABBREVIATIONS.....	viii
ACKNOWLEDGMENTS	ix
DEDICATION	x
CHAPTER 1 INTRODUCTION.....	1
1.1 Oil Shale.....	3
1.2 Geologic History	5
1.3 Current Infrastructure for Production	9
1.4 Previous Work	11
CHAPTER 2 METHODS	13
2.1 Total Organic Content and Source Rock Analysis	13
2.2 X-Ray Diffraction.....	15
2.3 Computer Tomography.....	16
2.4 Scanning Electron Microscope	16
2.5 Anisotropy	18
2.6 High Temperature High Pressure Experiment	26
CHAPTER 3 RESULTS	34

3.1	TOC and SRA Results	34
3.2	XRD Mineralogy Results.....	37
3.3	Computer Tomography Results.....	40
3.4	SEM Results	45
3.5	Waveform Analysis and Results	57
CHAPTER 4 DISCUSSION.....		66
4.1	Error Analysis.....	66
4.2	Data Analysis	69
4.3	Data Comparison	72
CHAPTER 5 CONCLUSIONS AND RECOMMENDATIONS.....		78
5.1	Conclusions.....	78
5.2	Future Work	80
REFERENCES CITED.....		82
APPENDIX A - EQUIPMENT SPECIFICATIONS		85
A.1	X-Ray diffraction	85
A.2	Micro CT.....	85
A.3	SEM	85
APPENDIX B - VELOCITY DATA.....		86

LIST OF FIGURES

Figure 1.1	Paraná Basin in Brazil (South America)	2
Figure 1.2	Irati Lithologic Log	6
Figure 1.3	Lithostratigraphy of the Paraná Basin	8
Figure 1.4	Paraná Basin tectonic map	8
Figure 1.5	Shell in-situ oil shale production method	9
Figure 1.6	Paraná Basin, Brazil	10
Figure 1.7	Petrobras Petrosix Surface Retort System	11
Figure 2.1	Programmed pyrolysis diagram	14
Figure 2.2	Example of a Van Krevlen Diagram	15
Figure 2.3	CT Scanner	17
Figure 2.4	3D CT scans of sample cored at 0° to symmetry axis	17
Figure 2.5	SEM basic Diagram	18
Figure 2.6	ESEM and FESEM example images	19
Figure 2.7	Backscatter analysis of pyrite	19
Figure 2.8	VTI Assumptions	20
Figure 2.9	Three core plugs taken from a VTI Medium	21
Figure 2.10	Velocities derived from the three different orientations of core plugs	21
Figure 2.11	Diagram of bulk modulus and shear modulus	24
Figure 2.12	Diagram of Young's modulus	24
Figure 2.13	Diagram of Poisson's Ratio	25

Figure 2.14	Compressional and shear wave propagation	25
Figure 2.15	High-temperature, high-pressure apparatus	27
Figure 2.16	Stainless steel confining jacket assembly	28
Figure 2.17	Lithium Niobate (LiNbO ₃) transducer.....	29
Figure 2.18	Calibration of Equipment.....	31
Figure 3.1	Results of Programmed Pyrolysis	35
Figure 3.2	XRD mineralogy bar graph.....	39
Figure 3.3	Range of 3D CT tomography.	40
Figure 3.4	C_{13} and δ vs. bedding angle	41
Figure 3.5	CT scans of 0° top view cross sections before and after	42
Figure 3.6	CT scans of 45° top view cross sections before and after.....	43
Figure 3.7	CT scans of 90° top view cross sections	44
Figure 3.8	CT scans of 0° side view cross sections	46
Figure 3.9	CT scans of 45° side view cross sections.....	47
Figure 3.10	CT scans of 90° side view cross sections.....	48
Figure 3.11	Angle between cross section and line perpendicular to bedding plane	49
Figure 3.12	Apparent dip used to calculate the true dip of the bedding plane.....	49
Figure 3.13	Pre-pyrolysis sample ESEM	50
Figure 3.14	Pre-pyrolysis sample ESEM	51
Figure 3.15	Pre-pyrolysis sample ESEM	51
Figure 3.16	ESEM of samples after pyrolysis	52
Figure 3.17	Pre-pyrolysis sample FESEM 10 μ m and 1 μ m	52
Figure 3.18	Post-pyrolysis (anhydrous) sample FESEM 100 μ m.....	53

Figure 3.19	Post-pyrolysis (anhydrous) sample FESEM $10\mu m$	54
Figure 3.20	Post-pyrolysis (hydrous) sample FESEM 1mm	55
Figure 3.21	Post-pyrolysis (hydrous) sample FESEM $100\mu m$	56
Figure 3.22	Post-pyrolysis (hydrous) sample $10\mu m$	56
Figure 3.23	EDS	57
Figure 3.24	Ramp up and cool down plot for anhydrous pyrolysis compressional velocities	58
Figure 3.25	Ramp up and cool down plot for hydrous pyrolysis compressional velocities	59
Figure 3.26	Ramp up and cool down plot for anhydrous pyrolysis shear velocities	59
Figure 3.27	Ramp up and cool down plot for hydrous pyrolysis shear velocities	59
Figure 3.28	Bulk modulus as a function of temperature	60
Figure 3.29	Shear modulus as a function of temperature	61
Figure 3.30	Poissons Ratio as a function of temperature	62
Figure 3.31	Epsilon as a function of temperature	64
Figure 3.32	Gamma as a function of temperature	64
Figure 3.33	Delta as a function of temperature	65
Figure 4.1	Recorded velocity data	67
Figure 4.2	BSE-SEM images of kerogen maturation before pyrolysis (top) and after (bottom)	68
Figure 4.3	Summary of velocity changes observed in the ramp-up and cool-down portions of anhydrous and hydrous pyrolysis	70
Figure 4.4	Comparison of before and after hydrous pyrolysis CT scans with hydrous compressional velocity measurements	71
Figure 4.5	Comparison of before and after hydrous pyrolysis CT scans with hydrous shear velocity measurements	71

Figure 4.6	Comparison of before and after hydrous pyrolysis SEM with hydrous compressional velocity measurements.....	72
Figure 4.7	Shear modulus shown with 0° oriented hydrous sample CT scan.....	73
Figure 4.8	Increase in velocities at lower temperatures after hydrous pyrolysis.....	74
Figure 4.9	Relationship between organic content and velocities	75
Figure 4.10	Stiffness coefficients C_{44} and C_{66} compared to Gamma (γ) from previous works.....	77

LIST OF TABLES

Table 2.1	Copper Calibration	33
Table 3.1	Rock-Eval of Block 003 samples (AR).	36
Table 3.2	Density and Porosity of Block 003 samples (AR).	36
Table 3.3	Mineralogy of Brazilian oil shale samples for Block 003 (weight percent).....	38
Table 3.4	Assumed densities of minerals in Block 003.	38
Table 3.5	Mineralogy of Brazilian oil shale samples for Block 003 (volume percent). ...	39
Table B.1	Anhydrous Ramp Up	87
Table B.2	Anhydrous Cool Down.....	88
Table B.3	Hydrous Ramp Up	89
Table B.4	Hydrous Cool Down	90

LIST OF SYMBOLS

Bulk Modulus	K
Delta (Thomsen Parameter)	δ
Epsilon (Thomsen Parameter)	ε
Gamma (Thomsen Parameter)	γ
Poisson's ratio (Vertical)	ν_V
Poisson's ratio (Vertical-Horizontal)	ν_{VH}
Poisson's ratio (Horizontal-Horizontal)	ν_{HH}
Shear Modulus (Vertical)	μ_V
Shear Modulus (Horizontal)	μ_H
Stress Tensor	σ_{ij}
Stiffness Tensor	C_{ijkl}
Strain Tensor	ϵ_{kl}
Young's Modulus (Vertical)	E_V
Young's Modulus (Horizontal)	E_H

LIST OF ABBREVIATIONS

American Association of Petroleum Geologists	APPG
as-received	AR
Computer Tomography	CT
Energy dispersive x-ray spectrometer	EDS
Environmental Scanning Electron Microscopy	ESEM
Field Emission Scanning Electron Microscopy	FESEM
gallons per ton	gal/ton
gas chromatography	GC
GigaPascal	GPa
hydrocarbon	HC
Hydrogen Index	HI
kilovolts	kV
milliamperes	mA
mass spectrometry	MS
milligrams of HC per gram of rock	mg HC/g rock
milligrams of CO ₂ per gram of rock	mg CO ₂ /g rock
Nuclear Magnetic Resonance	NMR
Oxygen Index	OI
Production Index	PI
pounds per square inch	psi

Rock Evaluation	Rock-Eval
Saturates, Asphaltines, Resins, Aromatics.....	SARA
Scanning Electron Microscopy.....	SEM
Source Rock Analysis	SRA
Total Organic Carbon.....	TOC
vertical transverse isotropy	VTI

ACKNOWLEDGMENTS

I would like to thank the Geophysics Department, my advisor Dr. Manika Prasad, my committee members Dr. Jerry Boak, Dr. Jeff Andrews-Hanna, and Dr. Terry Young. I would also like to thank George Radziszewski for teaching me to operate the equipment used in the high temperature set up. Finally, I would like to thank my colleagues in the Center for Rock abuse and in OCLASSH, my family, and Karen Moll for their assistance and support in obtaining my Master of Science degree.

In memory of Dr. Michael Batzle

CHAPTER 1

INTRODUCTION

Oil shale produces gas and liquid hydrocarbons when subjected to high temperatures and pressure. To better understand this process, a data set is presented here to better characterize oil shale, specifically in the Irati Formation from the Paraná Basin in the state of Paraná, Brazil (Figure 1.1). Changes in density, acoustic properties, macro- and microstructures, organic content, and mineralogy as a function of temperature and water content are observed, based on work by Elbaharia [2012]. Results from this study will help improve current surface-retorting methods. This data can be used to determine appropriate temperatures to heat specific sections of oil shale formations, as well as how to best incorporate water or brine into the pyrolysis system. Additionally, the experimental process for performing the high-temperature, high-pressure experiment has been streamlined and made more autonomous to reduce sample preparation time, acquire more reliable data, and to be more user friendly, which can be utilized in future work and experiments for different oil shale formations, such as the Green River formation.

By subjecting oil shale to high temperature and pressure, oil and gas are produced, thereby accelerating the natural geologic process of thermal maturation. Oil shale is a potentially large resource of hydrocarbon production. To make oil shale production economical, the properties of this resource must be properly understood to maximize production, while also reducing costs, environmental impact, and damage to the oil shale deposit itself.

This study presents a workflow to determine properties before, during, and after anhydrous and hydrous pyrolysis of oil shale. Yen [1976] defines pyrolysis of oil shale as thermally decomposing the organic materials (kerogen) within the shale and collecting the liquid products. Therefore, hydrous pyrolysis involves heating oil shale in the presence of water or brine, while anhydrous pyrolysis simply takes place in a dry, inert environment.

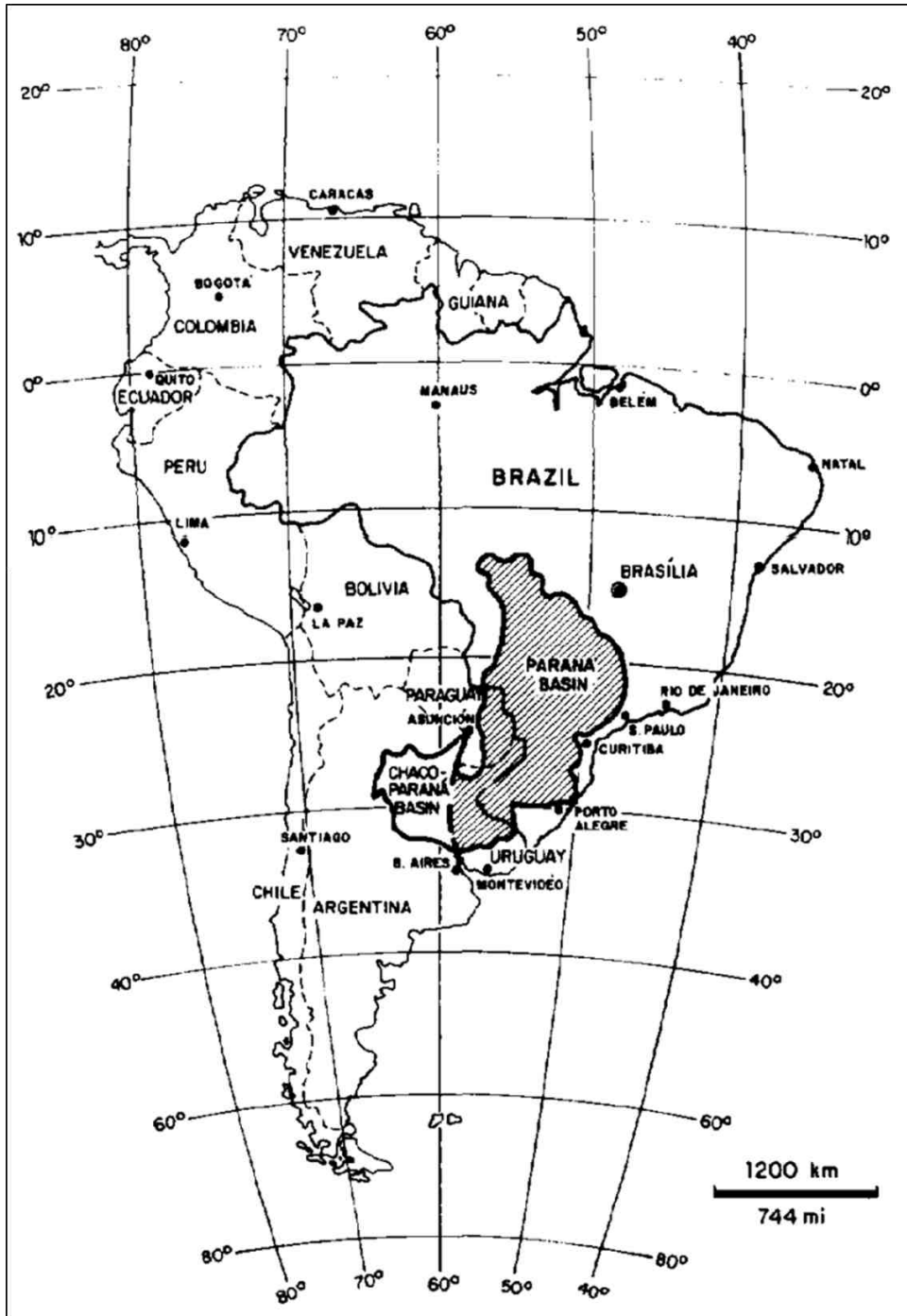


Figure 1.1: Paraná Basin in Brazil (South America)(figure from Zalán et al.)

The presence of water during pyrolysis has significant effects on hydrocarbon generation. Lewan et al. [2013] found a 38% vertical expansion on account of hydrous pyrolysis for unconfined oil shale cored perpendicular to the bedding plane. Lewan and Roy [2011] found that for Mahogany oil shale from the Green River formation, Total Organic Carbon (TOC) that remained in the hydrous rock was 34% lower compared to the anhydrous. Velocities should increase overall as a function of temperature, as any porosity should close within the samples due to confining pressure and conversion of organic matter to bitumen and hydrocarbons while subsequently being expelled from the samples. Because of this expulsion of organic matter, the TOC values should decrease more for the hydrous samples. Structurally, the core samples undergoing pyrolysis will likely compress vertically and expand laterally. Overall, it is expected that the hydrous pyrolysis will cause a more dramatic change in properties and structure compared to the anhydrous.

1.1 Oil Shale

Oil shale is commonly defined as a fine-grained rock with refractory organic matter that can be refined into fuel [Nowacki, 1981]. In immature oil shale, the organic matter is typically composed of relatively high amounts of type I kerogen and small percentage of bitumen, indicating that it is relatively immature. Yen [1976] found that the composition and oil yield of oil shale from São Paulo, Brazil, is 12.8 wt% organic carbon, 0.84 wt% sulfur, 0.41 wt% nitrogen, 75 wt% ash, and has an oil yield of 18 gal/ton. Most oil shale with type I kerogen forms in shallow waters with an abundance of organic matter sourcing. Common criteria from Cane [1976] and Hedberg [1964] for the genesis of large scale petroleum reservoirs are:

- Abundant production of organic matter
- Early development of an anaerobic environment
- Absence of total destructive organisms for oil maturation

In conventional oil reservoirs, sufficient thermal maturation and overburden pressures over time results in chemical breakdown of the organic structures in kerogen, which contributes to the formation of a hydrocarbon. When the carbon-carbon bonds in the kerogen break down, they turn first into bitumen, and subsequently into oil, coke, and gas [Cane, 1976]. Kerogen can be classified into four different types, depending on the source organic matter and the depositional environment.

Type I is formed in shallow marine, or lacustrine, environments, containing mostly algal organic matter [Cane, 1976], and has mostly oil prone hydrocarbon generation. Most existing literature data on the oil shale of Permian age in the Irati Formation has been found to contain type I kerogen. Da Silva and Cornford [1985] asserts that Irati shales contain predominantly degraded algal debris of fresh or brackish water origin, and a sub-bituminous/high volatile bituminous coal rank.

Other types of kerogen exist as well in more thermally mature rocks, each representing different hydrocarbon sources and thermal maturities. Type II kerogen is more common for petroleum source rocks, and is indicative of marine (reducing) depositional environments [Hantschel and Kauerauf, 2009], and can be sourced from marine algae, plankton, pollen spores, leaf waxes, and fossil resin [Yenugu, 2014]. It typically has a higher oxygen content compared to Type I kerogen, and therefore has both oil and gas hydrocarbon potential. Type III kerogen has even higher oxygen content, and a much lower hydrogen content. It is sourced from terrestrial plant matter in a shallow to deep marine environment. It has a lower hydrocarbon generative potential, and produces mostly dry gas if anything. Type IV kerogen is sourced from reworked organic debris and oxidized material [Yenugu, 2014]. It has a near zero hydrogen content, and therefore a near zero hydrocarbon generative potential.

Another comparative basin in South America, the Vaca Muerta, is also an organic rich source rock formation, but is more mature in general. Areas containing type I kerogen of marine origin have a maximum of 50mg HC/g. Additionally, S1, S2, and S3 values for the Vaca Muerta are lower, while Tmax values are much higher. This results in the Vaca Muerta

being a source rock for a more gas prone reservoir in the Nequina basin Garcia et al. [2013].

Ways to measure the thermal maturity of kerogen include vitrinite reflectance, source rock analysis (SRA), and total organic carbon (TOC). Vitrinite is formed from woody plant material, and gives a general indication of the thermal maturity of some kerogen types. A lithological column of the Irati Formation from a well bore in the area of interest can be seen in Figure 1.2 for portions of Irati oil shale that are buried. There are two main seams of oil shale, shown in the black areas. On average, the upper seam and lower seam has vitrinite reflectance (R_o) of 0.34% and 0.40%, respectively [Dyni, 2006]. These are low percentage values, and corresponding to a lower thermal maturity. Samples in this study were found to be type I using existing literature data [Da Silva and Cornford, 1985], and confirmed with SRA and TOC analysis.

There are three main members of the Irati formation from shallow to deep are the Sierra Alta, the Assistência, and the Taquaral. The upper and lower members consist of organic poor, dark to bluish gray claystones, while the Assistência member consists of dark gray to black bituminous shales interbedded with brown to light gray dolomite marls and claystones (Zalán et al.). TOC ranges for the Assistência are from 0.1-23%. Due to the composition and TOC, it is assumed that samples used in this study are from the Assistência member of the Irati Formation.

1.2 Geologic History

Zalán et al. describe the geologic evolution and sedimentary and structural formation of the Paraná basin. The intracratonic basin was formed during the Ordovician-to-Cretaceous period across Brazil, Paraguay, Uruguay, and Argentina, and was filled with mostly Paleozoic sediments. The Paraná Basin differs from basins such as the Williston Basin however in the following ways:

- The Paraná basin lacks consistent cap rocks at depths sufficient for thermal maturation

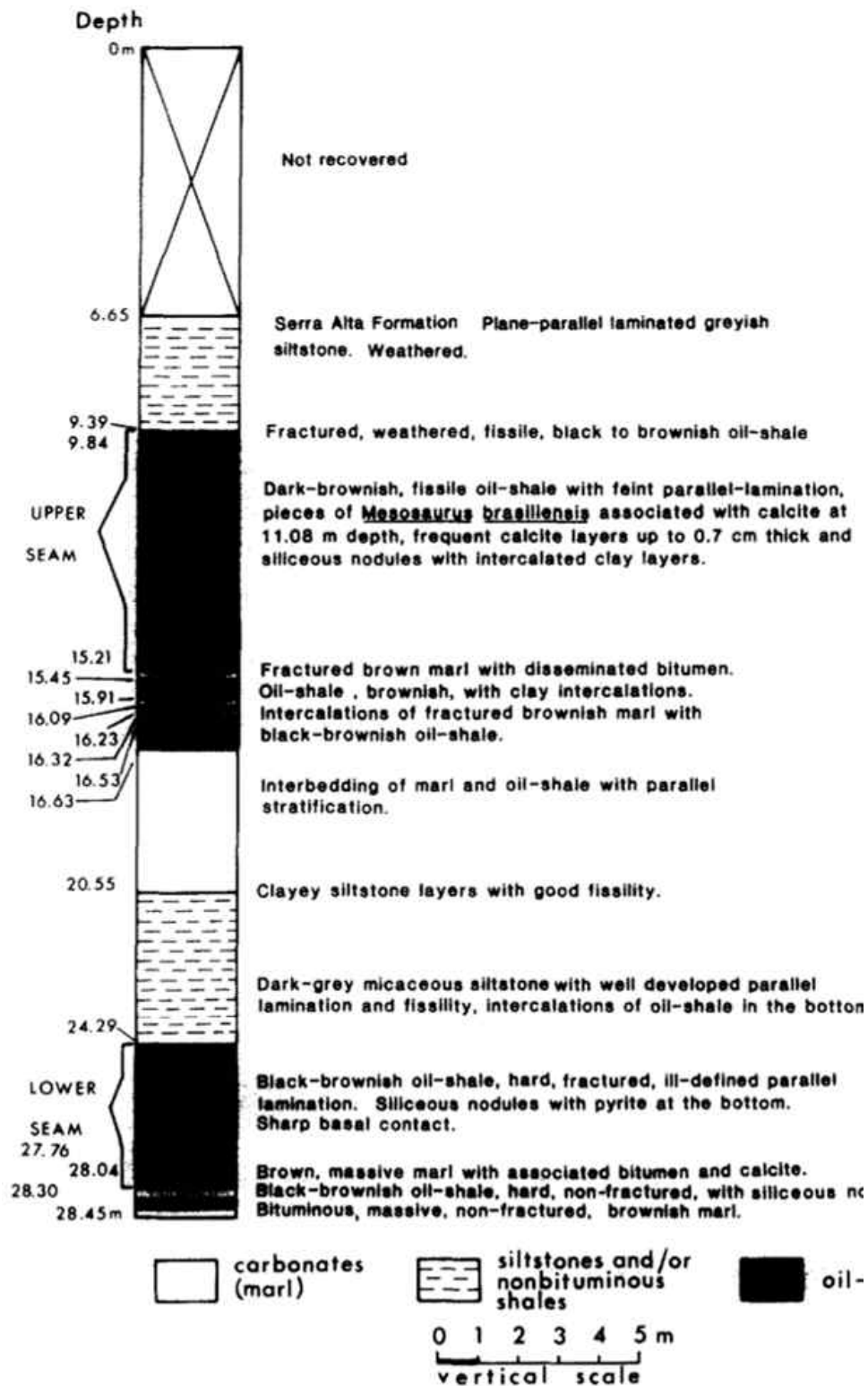


Figure 1.2: Irati Lithologic Log, showing the First and Second seam of oil shale (after Da Silva and Cornford [1985]).

- Dike intrusions and lava flows cause different levels of thermal maturation in the Irati Formation across the basin (TOC range from less than 1% to over 20%).
- The Paraná basin is a superposition of 3 different basins.
- The Origin of the Paraná basin is unclear, with lack of evidence for a central underlying rift.

Most of the basin is covered in Jurassic-Cretaceous basaltic lava flows up to 1700 meters thick, while a third of the basin contains outcrops of older sedimentary rocks, up to 6000 meters thick. Varying levels of TOC are seen in the Irati based on whether areas underwent normal maturation or matured faster from diabase sill intrusion. Therefore, it is important to know the maturity of samples used in experiments.

About three different basins were developed in multiple tectonic environments to form the present basin, which is limited by either pinch-outs or tectonic uplifts. To the northeast, there is evidence of erosion resulting in geologic pinch-outs. To the west and south exist several uplifts. The basin itself is asymmetric in the direction of the Asunción arch (number 30 in Figure 1.4), dipping 1° to 4° , while the eastern section's regional dip is closer to 0.5° to 1° . To the north, another arch exists, indicating a flexural response to the crust to the sedimentary-plus-volcanic load of the Paraná basin [Zalán et al.].

Northwest-trending arches contain sites for dike swarms and igneous intrusions, and also indicate a level of tectonic control in the older zones. The southeast portion of the basin underwent the Serra do Mar uplift, leading to development of large coastal ranges in southeastern Brazil (Figure 1.4).

Five depositional sequences were responsible for the filling of the Paraná Basin, which Zalán et al. relates to periods of time during the most sedimentation: Silurian, Devonian, Permo-Carboniferous, Triassic, and Juro-Cretaceous. The Paleozoic sequences went through complete transgression and regression cycles, while Mesozoic sequences were controlled by continental tectonic events. A lithostratigraphic column of this geologic development can be

seen in Figure 1.3.

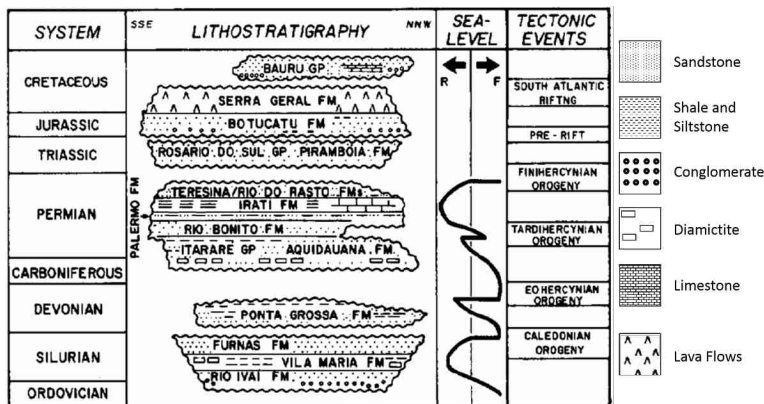


Figure 1.3: Lithostratigraphy of the Paraná Basin(After Zalán et al.). R and F are rising sea level and falling sea level, respectively.

1.3 Current Infrastructure for Production

A few different methods exist for producing from oil shale, but they can essentially be separated into two groups: 1) In-situ retorting and 2) above-ground retorting. In-situ retorting involves drilling boreholes and applying heat down hole to produce. Different methods have been tried by different companies, such as Shell and Exxon in the Piceance basin. These methods, while less environmentally destructive due to less surface material to handle and dispose of, are not as economically viable. For example, a method employed by Shell involves drilling several wells to both heat the oil shale and produce from it, as well as to preserve the quality of ground water, shown in Figure 1.5. This method is more effective for more deeply buried oil shale, but more shallow deposits are easier to mine and retort on the surface.

The Irati formation itself outcrops in Brazil in a sinuous ‘S’ shape along the northeastern portion in the state of Paraná, shown in Figure 1.6 [Dyini, 2006]. This outcrop allows for easy access for surface mining and retorting. The samples used in this study were specifically from the town of São Mateus do Sul, Paraná.

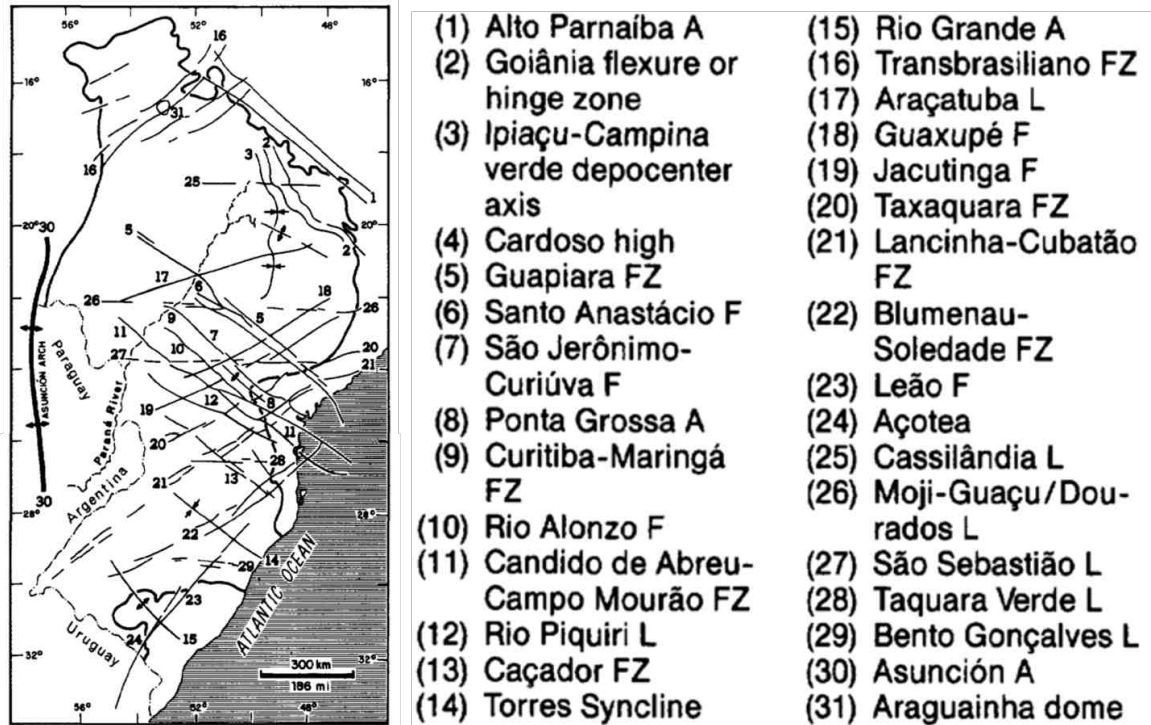


Figure 1.4: Paraná Basin tectonic map(After Zalán et al.). Numbers 1-31 represent different boundaries and faults that constrain the Paraná Basin. Numbers 1-15 represent Northwest trending tectonic elements. Numbers 16-24 represent Northeast trending tectonic elements. 30 is the North-South trending Asuncí on Arch, and 31 is the Araguinha dome, which is the remnant of a large crater.

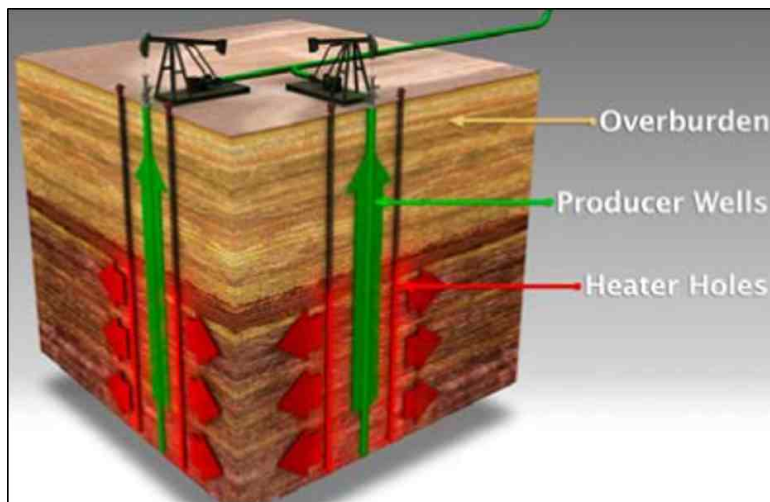


Figure 1.5: Shell in-situ oil shale production method, (after Boak [2007])

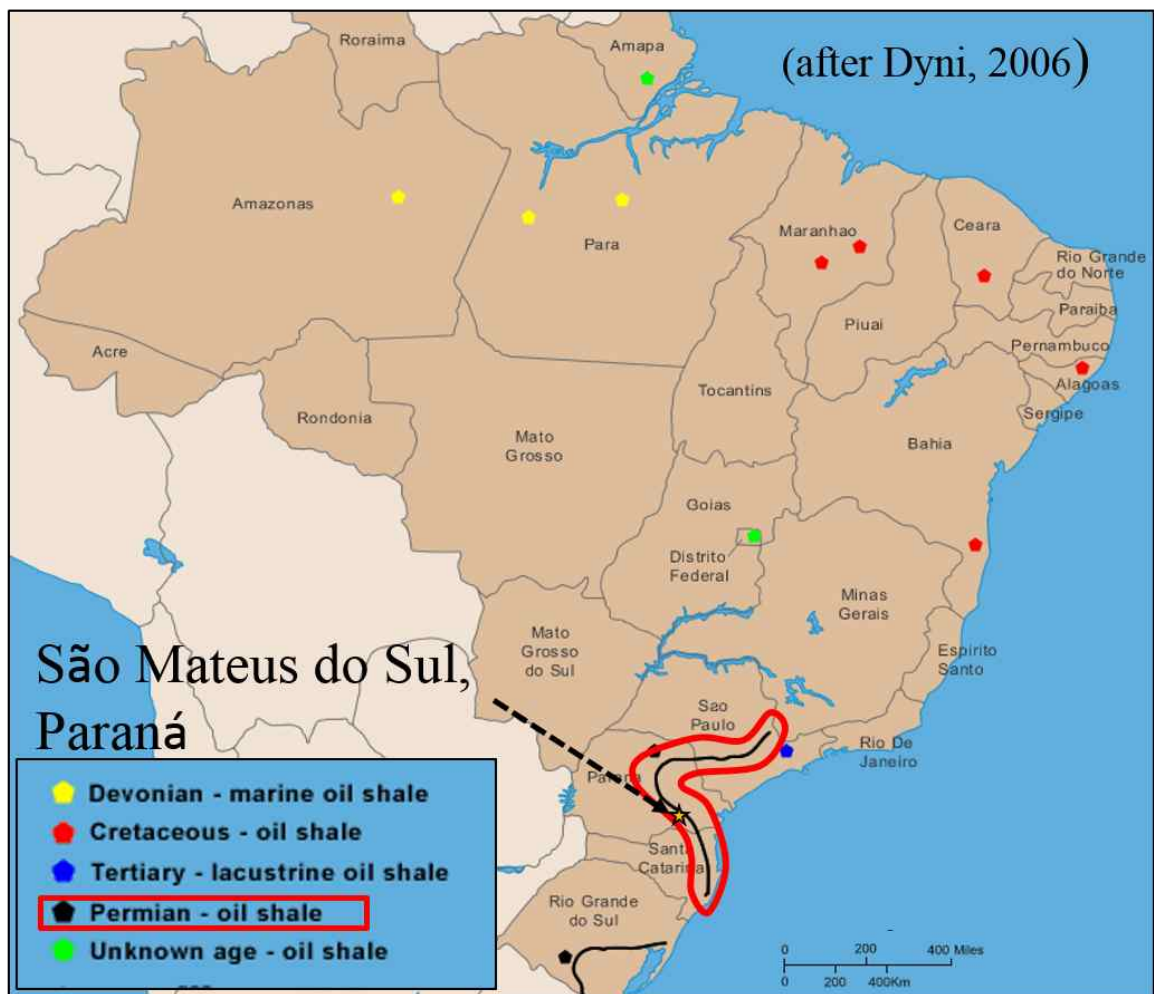


Figure 1.6: Paraná Basin, Brazil, showing Permian and Tertiary oil shale locations. (After Dyni [2006])

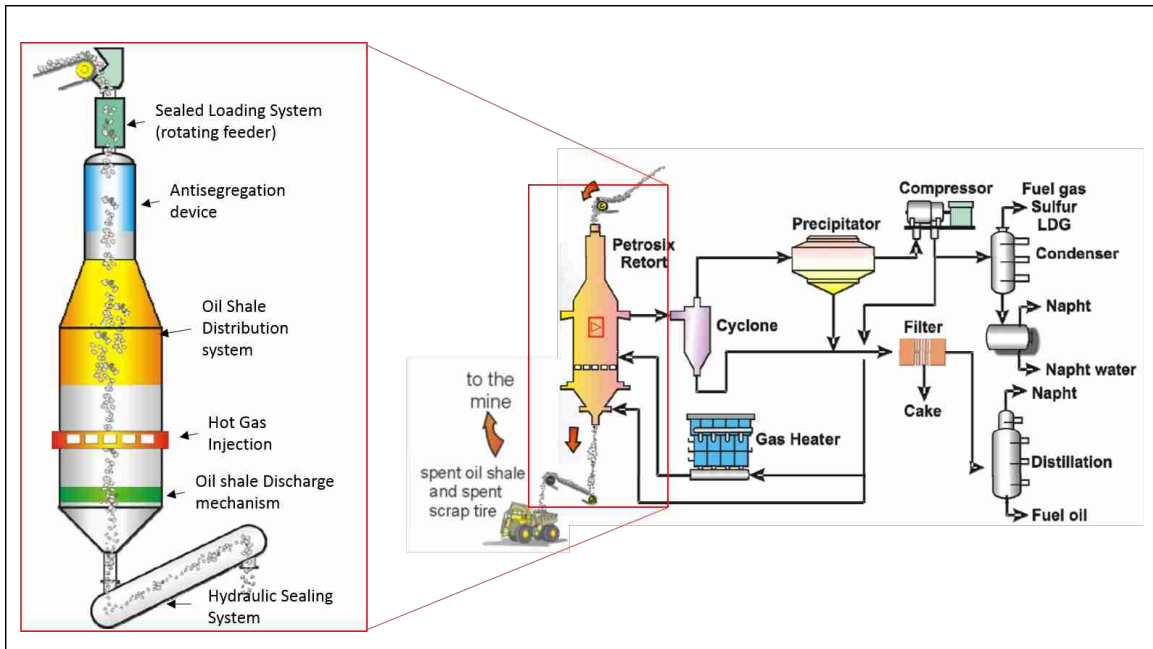


Figure 1.7: Petrobras Petrosix Surface Retort System (after Filho et al. [2008]).

The Petrosix method developed by Petrobras (Figure 1.7) is a vertical cylindrical retort system [Qian and Wang, 2006]. Yen [1976] and Qian and Wang [2006] describe the Petrosix surface-retorting method. Oil shale is mined, and crushed to pieces between 0.6 and 5 cm in size, and fed into the top of the retort. Gas is heated in an external furnace and put into the midpoint of the retort, getting as hot as 500° C. Additionally, another stream of cool gas is flushed through the lower portion of the retort to capture residual heat from spent oil shale (coke) coming out of the bottom, and then the newly hot gas travels back up to continue heating the middle of the retort. This dual heat system is a more efficient system for heating the oil shale. Any oil vapors and droplets are taken from the top, the oil is removed and sent to a sulfur-recovery plant, and the gas produced is recycled. A retort made in 1991 in the city of São Mateus do Sul can process up to 6,200 tons per day. The products typically contain 1% sulfur and 0.8% nitrogen. This system is efficient, but it could be improved by using techniques presented here to adjust temperatures for maximum thermal efficiency.

1.4 Previous Work

Recent developments in experimentation on oil shale are the basis for this work. Previous work on Green River Oil Shale by Elbaharia [2012] and Lewan and Roy [2011] have developed new ways of performing tests on oil shale as a function of temperature and water content during pyrolysis.

Elbaharia [2012] developed a method that can determine the change in compressional and shear velocities through small core samples as a function of temperature. This process works under the assumption that the anisotropy in the samples is vertically transverse, or having a single axis of symmetry. From these velocities, elastic moduli and Thomsen parameters were derived, which are useful in upscaling parameters for seismic acquisition and monitoring. For this study, these properties are necessary to understand change in rock properties as a function of temperature to determine if maximum efficiency is achieved during different types of pyrolysis. Elastic properties that can be derived include horizontal and vertical Young's modulus, bulk modulus, shear modulus, as well as Poisson's ratio.

Lewan et al. [2013] has performed several hydrous pyrolysis experiments on Green River oil shale. Experiments involved putting core samples in a uniaxial confining clamp, and subjecting the samples to hydrous and anhydrous pyrolysis. In one experiment, temperature on samples was increased to $350^{\circ}C$ for 72 hours in the presence of brine. This yielded 29% more hydrocarbon production compared to the anhydrous pyrolysis. Due to the similarity in kerogen type, and ultimately thermal maturity, the experimental design for hydrous and anhydrous pyrolysis is based on Elbaharia [2012], while the experimental process is based off of Lewan et al. [2013].

CHAPTER 2

METHODS

This chapter discusses the methods used to characterize the oil shale samples. All methods were performed on samples before and after pyrolysis. For the High-Temperature, High-Pressure experiment, data and analysis were collected during the experiment. These methods allow a comprehensive analysis of Irati oil shale.

2.1 Total Organic Content and Source Rock Analysis

The initial Rock Evaluation, or Rock-Eval, was determined through programmed pyrolysis, courtesy of Weatherford Labs. In this experiment, pyrolysis is performed under controlled conditions, and the maximum amounts of different hydrocarbon and oxygen compounds can be determined, known as S1, S2, and S3. The operating conditions (provided by Weatherford Labs) for programmed pyrolysis are:

- S1: 300°C for 3 minutes
- S2: 300°C to 600°C at 25°C/min; held at 600°C for 1 minute
- S3: Peak of released CO₂ trapped between 300 to 390°

This is illustrated in Figure 2.1. TOC is determined by burning a rock sample in an oxygen-rich environment and measuring the amount of carbon dioxide produced. The S1 peak corresponds to the highest amount of volatile, or free, hydrocarbon (HC) produced, in milligrams of HC per gram of rock (mg HC/g rock). A high S1 peak indicates either large amounts of kerogen-derived bitumen or the presence of migrated hydrocarbons. Given the immature nature of the samples in this study, a high S1 peak likely corresponds to kerogen-derived bitumen.

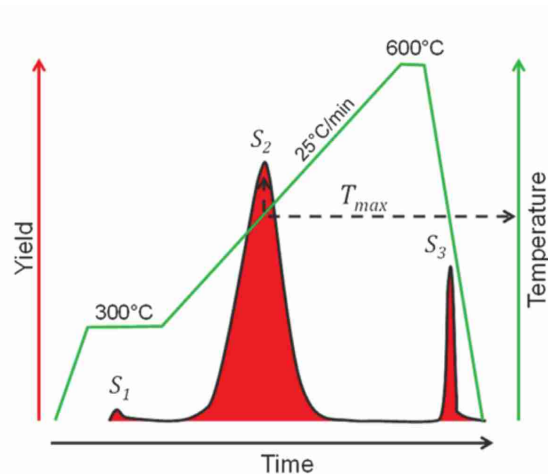


Figure 2.1: Programmed pyrolysis diagram, showing the S1, S2, and S3 peak in time (Figure from Hart and Steen [2015]).

The S2 peak corresponds to the remaining HC generative potential, also in mg HC/g rock. The S2 peak is also proportional to the amount of hydrogen-rich kerogen in the rock, and the maximum value on the S2 peak corresponds to the ‘Tmax’, and is indicative of source rock maturity. The last relevant peak is the S3 peak, corresponding to any molecules containing oxygen that are produced, specifically CO₂, in milligrams of CO₂ per gram of rock (mg CO₂/g rock). From these peak responses and the TOC content, it is possible to determine other important parameters that help determine the type of organic matter in the rock. The Hydrogen Index (HI) is the measure of hydrogen-to-carbon ratio in the shale, while the Oxygen Index (OI) is likewise the measurement of oxygen-to-carbon ratio. These indices can be cross plotted and used to characterize the type of kerogen in a rock, which will fall into 1 of 4 zones shown in the Van Krevlen Diagram in Figure 2.2. Typically, better producing organic rich rocks have a low OI compared to the HI, as HC generation requires anoxic conditions. Production index (PI) is a derived measurement from S1 and S2 values, relating the amount of hydrocarbons produced during the first and second stage of pyrolysis, and generally increases with burial depth [McCarthy et al., 2011]. These values are derived from the results of the programmed pyrolysis as shown below:

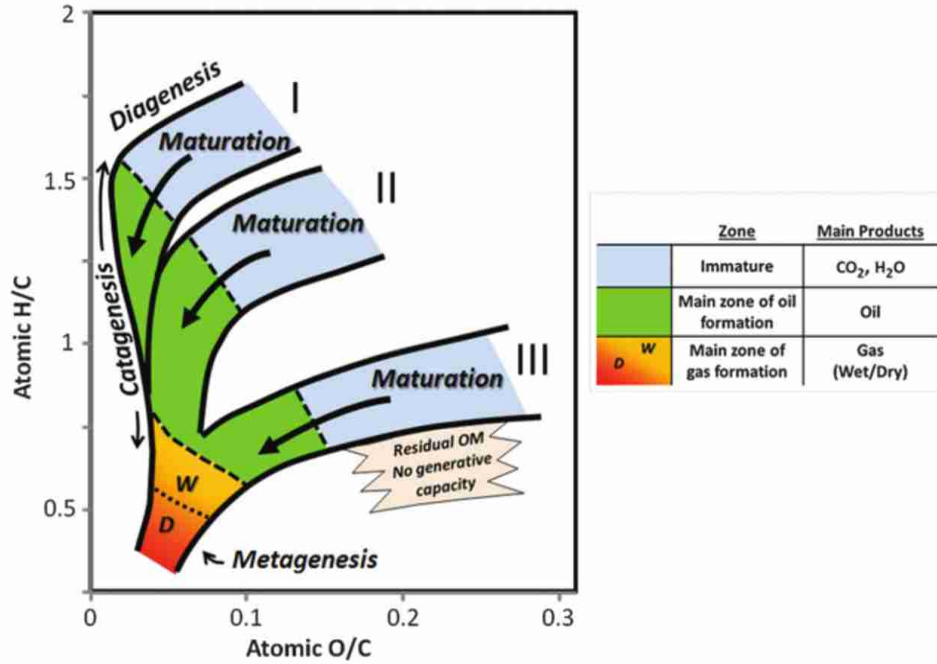


Figure 2.2: Example of a Van Krevlen Diagram(Figure from Hart and Steen [2015]).

$$HI = \frac{S2}{TOC} \times 100(mgHC/gTOC) \quad (2.1)$$

$$OI = \frac{S3}{TOC} \times 100(mgCO_2/gTOC) \quad (2.2)$$

$$PI = \frac{S1}{(S1 + S2)} \quad (2.3)$$

2.2 X-Ray Diffraction

X-ray diffraction (XRD) works by projecting x-rays towards crystalline material at an angle (θ), and measuring the scattering, or diffraction pattern off of the material. The diffraction can be quantified when the distance traveled by the reflected waves differs by n-number of wavelengths (λ). Essentially, x-rays are scattered as they hit electrons in a sample, and therefore the amount of scattering is proportional to the amount of electrons in the sample [Lavina et al., 2014]. The Bragg's representation of a crystal diffraction in a crystalline structure is defined by equation 2.4, in which h,k, and l are crystallographic

planes, d is the spacing of set planes, and θ is incident angle.

$$2d_{hkl}\sin(\theta)_{hkl} = n\lambda \quad (2.4)$$

To determine the mineralogy, XRD was performed on samples before and after pyrolysis. A portion of each sample is ground to 10-15 microns in size. Samples are scanned for at least one hour, using K-alpha radiation. It was important to determine mineralogy before and after pyrolysis experiments. An initial assumption made was that no mineralogical change would occur, but that the amorphous amount of material would decrease after pyrolysis.

2.3 Computer Tomography

Computer tomography (CT) scans were acquired on all samples before and after pyrolysis. This provided data for initial assumptions regarding the angle of the lamination in the samples with respect to the axis of symmetry. Additionally, CT scans provided good imaging for any existing fractures, developed fractures as a result of pyrolysis, or impurities that might interfere with subsequent assumptions (i.e., large pyrite nodules).

CT is performed by placing a cylindrical core sample into the scanner (Figure 2.3). A sample is rotated slowly 180 degrees, and an x-ray image is obtained at each small incremental rotation. Next, the images are reconstructed, to provide a full 3D x-ray volume through the sample. This can be seen in Figure 2.4.

2.4 Scanning Electron Microscope

To confirm porosity and structural changes on the micron scale, two types of scanning electron microscopy (SEM) were used. The first was an environmental electron microscope (ESEM). The ESEM did not have as high resolution, but allowed for low-vacuum conditions. The Field Emission Scanning Electron Microscope (FESEM) had higher resolution, but could only image in high-vacuum environments, and had more difficulty getting clear and consistent images of the oil shale. A basic diagram of how an SEM microscope works is shown in Figure 2.5.

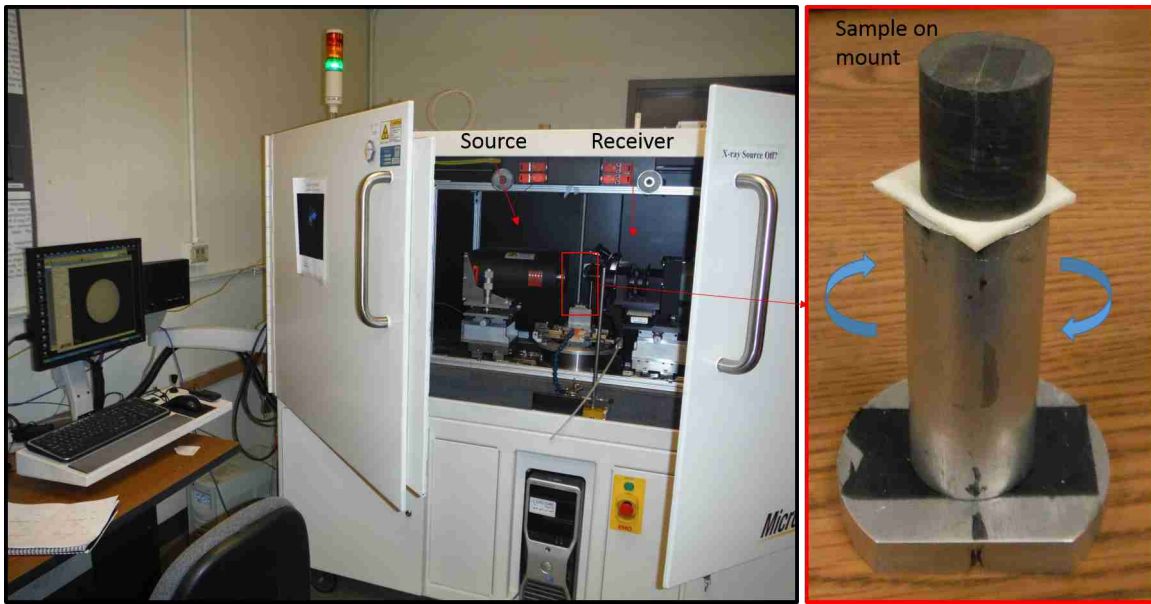


Figure 2.3: CT Scanner

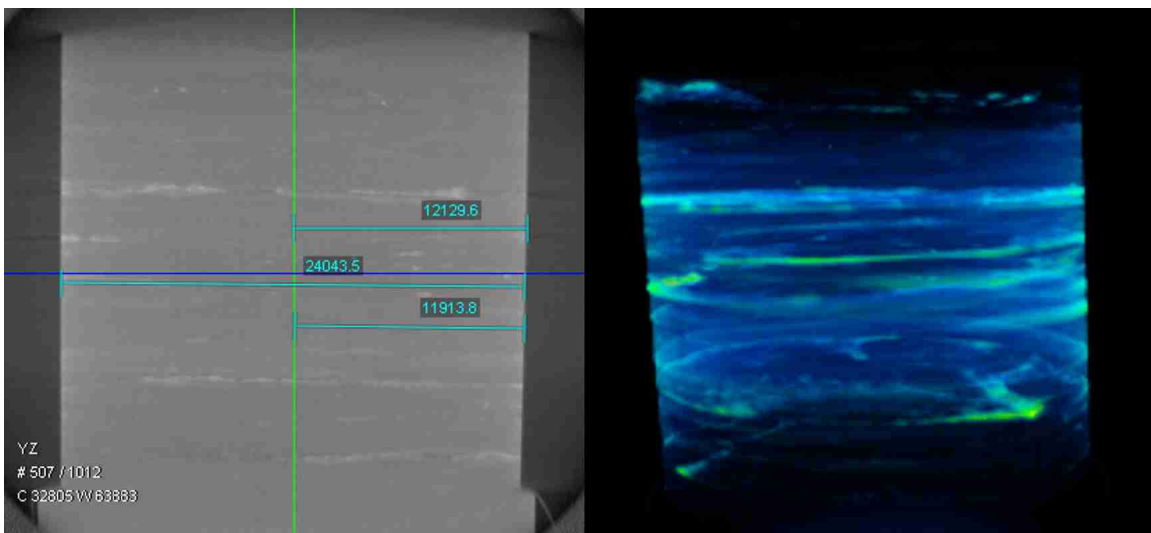


Figure 2.4: 3D CT scans of sample cored at 0° to symmetry axis. 2D cross section (left), and 3D volume (right)

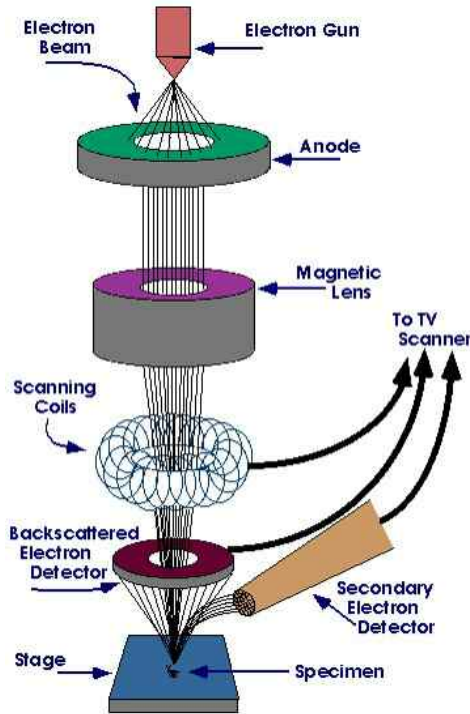


Figure 2.5: SEM basic Diagram. Image courtesy of Iowa State University SEM homepage

At the basic level, SEM works by projecting electrons onto a sample surface, and detecting the reflected electrons, which in turn make the image, as opposed to x-ray or optical imaging, such as images shown in Figure 2.6. In addition to creating high resolution images at the micron scale, it is also possible to perform some analysis using a backscatter detector. For example, elements and compounds in the pyrite framboid from the ESEM are shown below in Figure 2.7.

Being able to detect porosity and structural changes on a micron scale will help compare the difference between hydrous and anhydrous pyrolysis, and will result in better characterization of oil shale overall.

2.5 Anisotropy

For an arbitrary rock medium, there exists the conventional stress-strain relationship:

$$\sigma_{ij} = C_{ijkl}\epsilon_{kl} \quad (2.5)$$

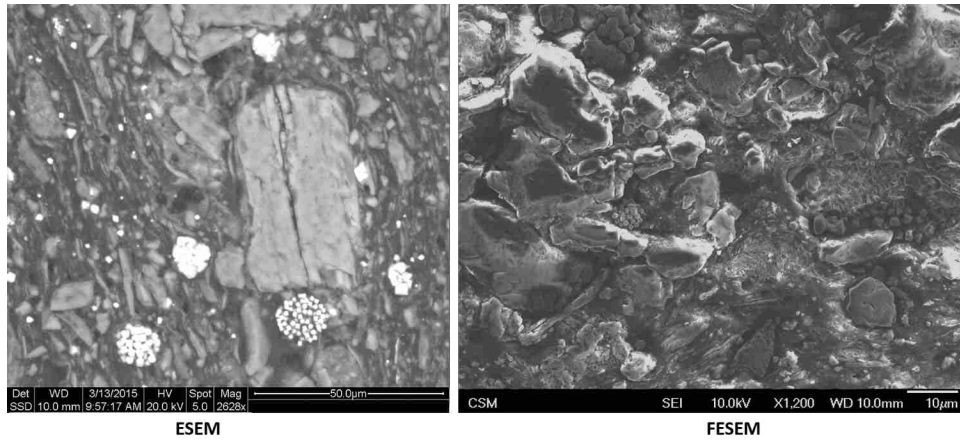


Figure 2.6: ESEM and FESEM example images ESEM (left), at approximately $50\mu m$ resolution, FESEM (right), at approximately $10\mu m$ resolution.

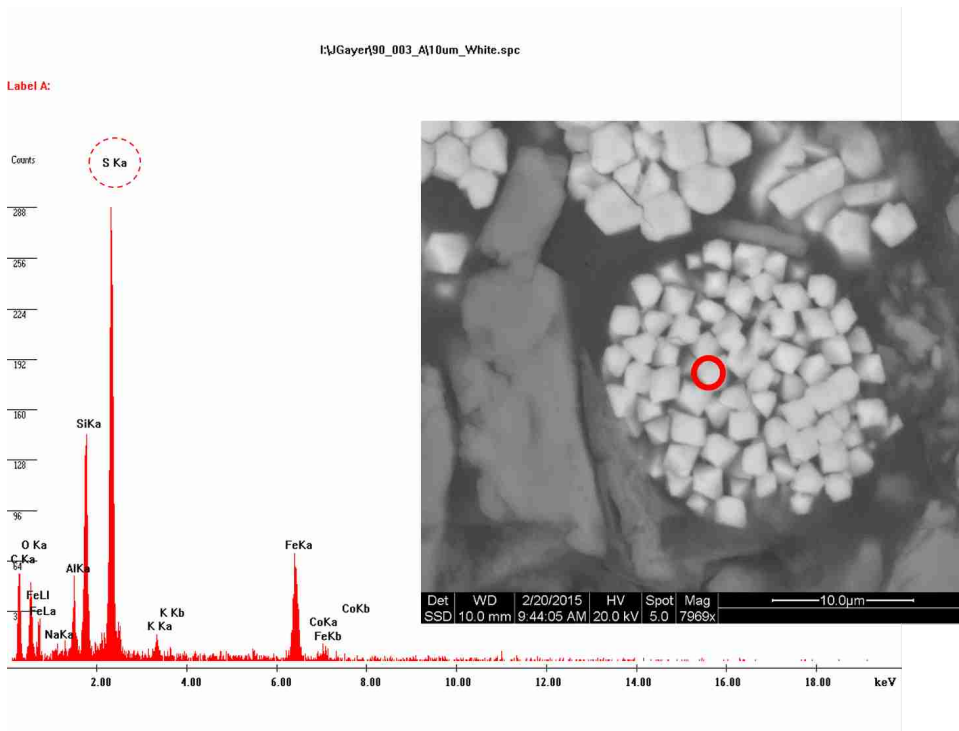


Figure 2.7: Backscatter analysis of pyrite. The tallest peak has detected a compound containing sulfur compound, “S Ka”, which indicates an iron sulfide, or pyrite

where σ_{ij} is the stress, C_{ijkl} is the stiffness coefficient, and ε_{kl} is the strain, or unitless ratio of deformation. C_{ijkl} can be thought of as the link between the deformation of a medium and an applied stress. Therefore, the higher the stiffness coefficient, the more stress it takes in the ij direction to cause a strain (deformation) in the kl direction. To account for every type of deformation possible as a result of stress, there are 81 independent stiffness coefficients.

In order to make consistent calculations for all oil shale samples, it is necessary to make assumptions about the structural properties of the rock. The oil shale samples described here (and most shale samples in general) can be said to be laminar on a macroscopic and even microscopic scale. Therefore, we can assume our samples exhibit vertical transverse isotropic (VTI). Under this assumption, we can reduce the number of independent stiffness coefficients from 81 to just 5 (Figure 2.8), and their notations can be shortened using Voigt notation. For example, C_{1111} would reduce to C_{11} . Additionally, these 5 stiffness coefficients can all be derived from measurements from three orientations of shale (Figure 2.9). These orientations are determined based on how the samples are cored with respect to the symmetry axis (axis 3). For example, the 0° sample is cored perpendicular to the bedding plane, but parallel to the symmetry axis. The necessary velocities to derive stiffness coefficients from the three orientations are shown in Figure 2.10.

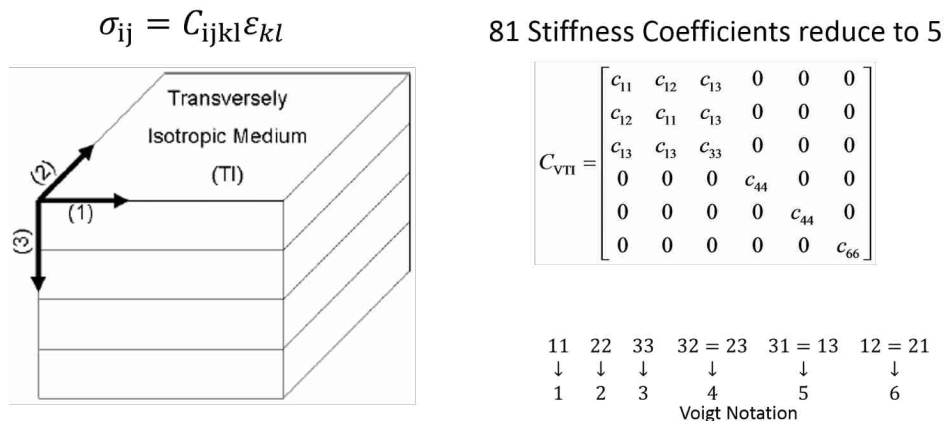


Figure 2.8: VTI Assumptions for reduced stiffness tensor.

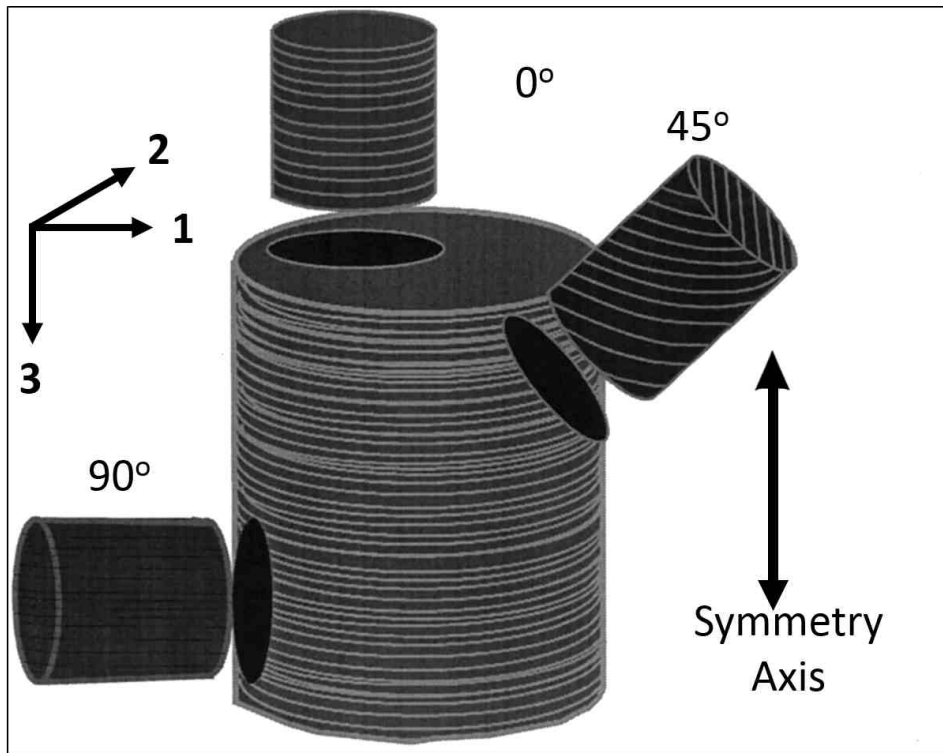


Figure 2.9: Three core plugs taken from a VTI Medium, after Wang [2002].

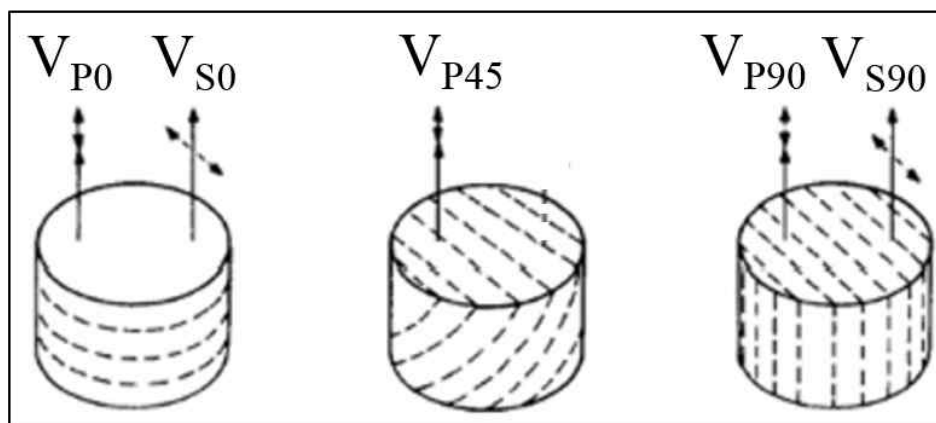


Figure 2.10: Velocities derived from the three different orientations of core plugs, after Elbaharia [2012]

The stiffness coefficients for a VTI medium can be calculated as follows, after Thomsen [1986]:

$$C_{11} = \rho V_{P90}^2 \quad (2.6)$$

$$C_{33} = \rho V_{P0}^2 \quad (2.7)$$

$$C_{44} = \rho V_{S0}^2 \quad (2.8)$$

$$C_{66} = \rho V_{S90}^2 \quad (2.9)$$

$$C_{12} = C_{11} - 2C_{66} \quad (2.10)$$

$$C_{13} = \sqrt{\frac{(4\rho V_{P45}^2 - C_{11} - C_{33} - 2C_{44})^2 - (C_{11} - C_{33})^2}{4}} - C_{44} \quad (2.11)$$

where V_{P0} is the

There are six total equations, but only five are independent, with C_{12} being derived from C_{11} and C_{66} . Additionally, 2.11 shows the dependence of C_{13} on the compressional velocity measured at a 45° angle. Often it is difficult to cut a sample to have an exact 45° to the symmetry plane. In that case, C_{13} can be calculated using equation 2.12 as follows from Yan et al. [2013]:

$$C_{13} = \csc(2\theta)(2\sqrt{D} - C_{44}\sin(2\theta)) \quad (2.12)$$

Where D is given by:

$$D = \frac{(C_{11}\sin^2\theta + C_{44}\cos^2\theta - \rho V_{P\theta}^2)}{(C_{33}\sin^2\theta + C_{44}\cos^2\theta - \rho V_{P\theta}^2)} \quad (2.13)$$

Once the stiffness coefficients have all been determined, elastic moduli and Thomsen parameters can be derived, based on Yan et al. [2013]:

$$K = \frac{C_{33}(C_{11} + C_{12}) - 2C_{13}^2}{C_{11} + 2C_{33} + C_{12} - 4C_{13}} \quad (2.14)$$

$$E_H = \frac{4C_{66}(C_{33}(C_{11} - C_{66})) - C_{13}^2}{C_{11}C_{33} - C_{13}^2} = E_3 \quad (2.15)$$

$$E_V = \frac{C_{33}(C_{11} - C_{66}) - C_{13}^2}{C_{11} - C_{66}} = E_1 = E_2 \quad (2.16)$$

$$\nu_V = \frac{C_{13}}{2(C_{11} - C_{66})} = \nu_{31} = \nu_{32} \quad (2.17)$$

$$\nu_{HV} = \frac{2C_{13}C_{66}}{(C_{11}C_{33} - C_{13}^2)} = \nu_{13} = \nu_{23} \quad (2.18)$$

$$\nu_{HH} = \frac{C_{33}(C_{11} - 2C_{66}) - C_{13}^2}{(C_{11}C_{33}) - C_{13}^2} = \nu_{12} = \nu_{21} \quad (2.19)$$

$$\mu_V = C_{44} = C_{55} \quad (2.20)$$

$$\mu_H = C_{66} \quad (2.21)$$

Where K is the bulk modulus (GPa), E_H and E_V are the horizontal and vertical Young's modulus (Gpa), respectively (Figure 2.11). ν_V , ν_{HV} , and ν_{HH} are the vertical, horizontal-vertical, and horizontal-horizontal Poisson's ratio, respectively. Three Poisson's ratios describe each possible axial strain to transverse strain relationship in a VTI medium. This is better illustrated in Figure 2.13. Likewise, two Young's moduli to describe VTI sample deformation Figure 2.12 vertically (E_V) and horizontally (E_H). Only one bulk modulus is necessary, as it describes the bulk deformation of whole sample. The shear modulus is a measure is a measure of the deformation occurring in an elastic medium when a stress is applied parallel to one face, while the opposite face is held fixed (ratio of shear stress to shear strain).

It is important to note that these figures exhibit large-scale deformation, and the moduli can be measured in axial confining tests. However, for the purposes of this study, elastic moduli and Thomsen parameters must be derived. Deformations exhibited in Figure 2.11, Figure 2.13, and Figure 2.12 are derived as a result particle deformations associated with waveform propagation in different directions through a VTI medium (Figure 2.14). For example, the vertical shear modulus and horizontal shear modulus are derived from polarization of the shear wave traveling in the 0° and 90° directions, respectively.

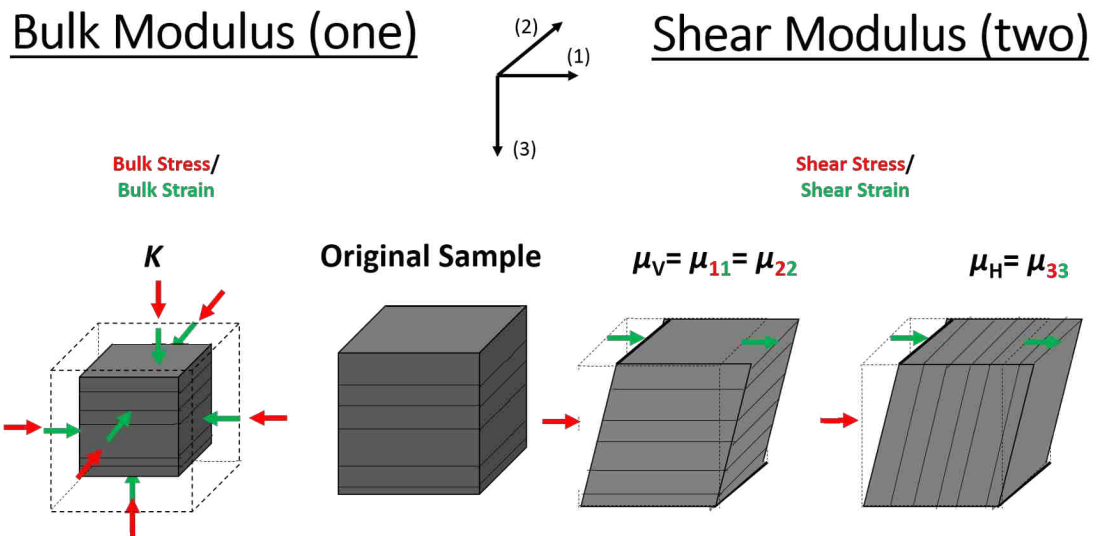


Figure 2.11: Diagram of bulk modulus and shear modulus

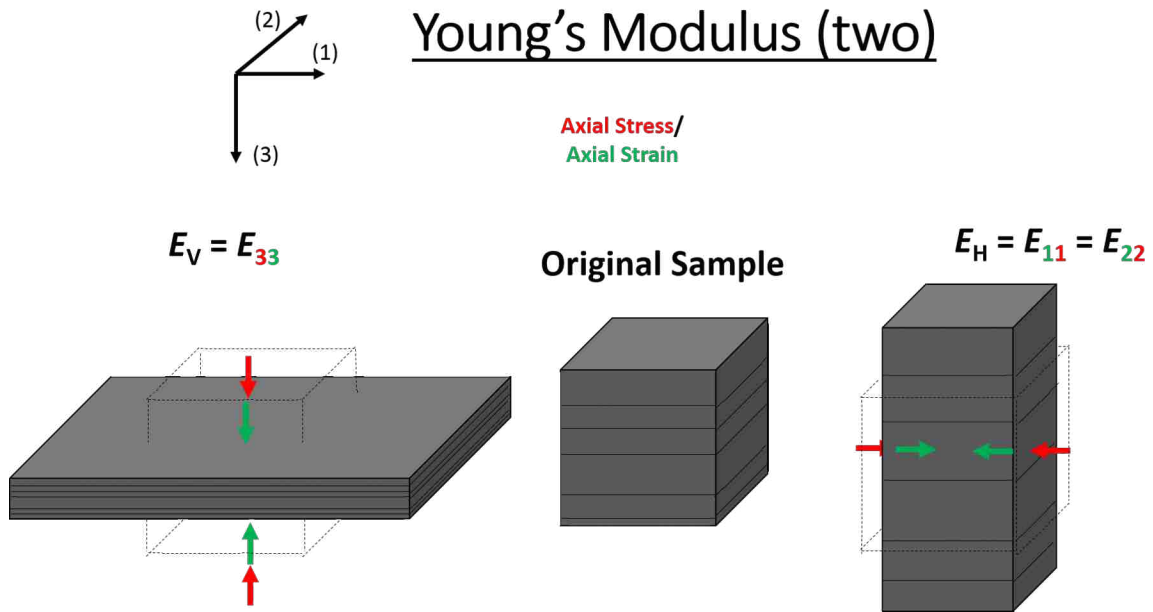


Figure 2.12: Diagram of Young's modulus

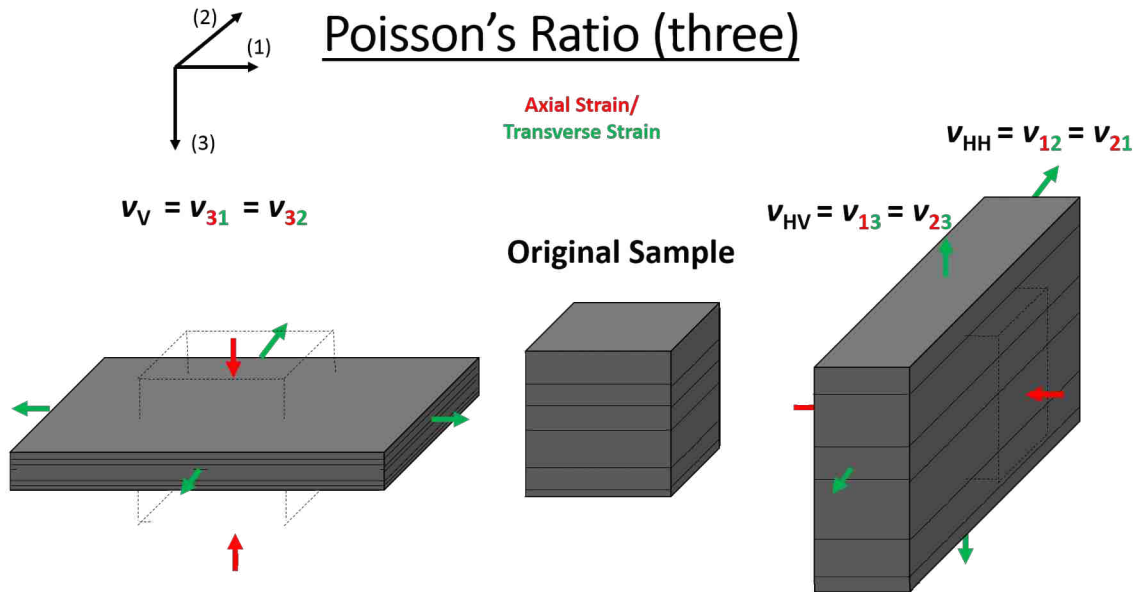


Figure 2.13: Diagram of Poisson's Ratio

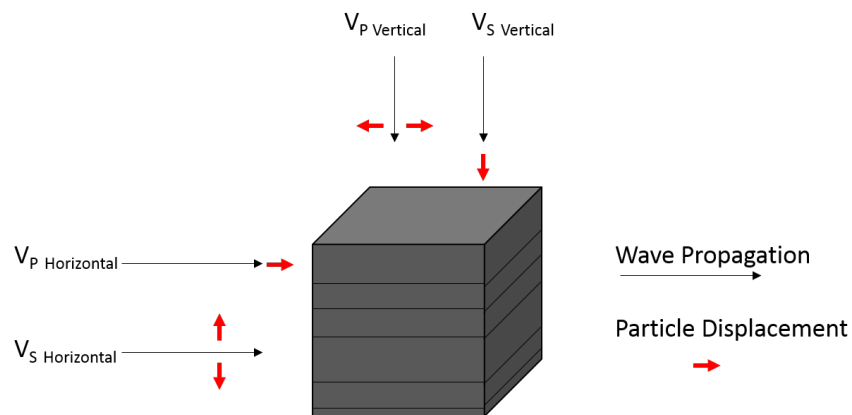


Figure 2.14: Compressional and shear wave propagation

In addition to elastic moduli, Thomsen parameters also play an important role in shale characterization. epsilon (ε) is mathematically equal to the fractional difference between the vertical and horizontal P wave, and gamma (γ) is similarly the fractional difference between the vertical and horizontal S waves [Thomsen, 1986]. Delta (δ) can be described from Tsvankin [1997] as the second derivative of P-wave phase velocity at vertical incidence in the $[x_1, x_3]$ plane. For the purposes of VTI media, this also would include vertical incidence in the $[x_2, x_3]$ plane.

$$\varepsilon = \frac{C_{11} - C_{33}}{2C_{33}} \quad (2.22)$$

$$\gamma = \frac{C_{66} - C_{44}}{2C_{44}} \quad (2.23)$$

$$\delta = \frac{(C_{13} + C_{44})^2 - (C_{33} - C_{44})^2}{2C_{33}(C_{33} - 4C_{44})} \quad (2.24)$$

2.6 High Temperature High Pressure Experiment

Samples are placed inside of the pressure vessel, providing a containment system to apply an initial confining pressure of 1000 pounds per square inch (psi) on a single sample. The Teledyne Isco-pump is connected directly to the sample, which is encased in a smaller closed container, in order to apply an internal pore pressure of 200 psi. Initial pressures were chosen such that throughout an experiment, approximately 800 to 900 psi of differential pressure was applied. Based on previous work for hydrous pyrolysis after Lewan and Roy [2011], the temperature is increased from 25°C at a rate of 10°C/10min, and maintained at 365°C for 48 hours, and subsequently cooled at a rate of 10°C/10min using a temperature controller connected to a computer. The experimental setup is based on recent thesis work from Elbaharia [2012]. All equipment was inspected and calibrated to produce the best and most consistent results. The overall setup is shown below in Figure 2.15.

The sample is then placed in a stainless steel confining jacket (Figure 2.16). Once the sample assembly is put together, it is placed inside the large green pressure vessel in Figure 2.15. Using an Teledyne-Isco pump, brine of known properties can be pumped into the

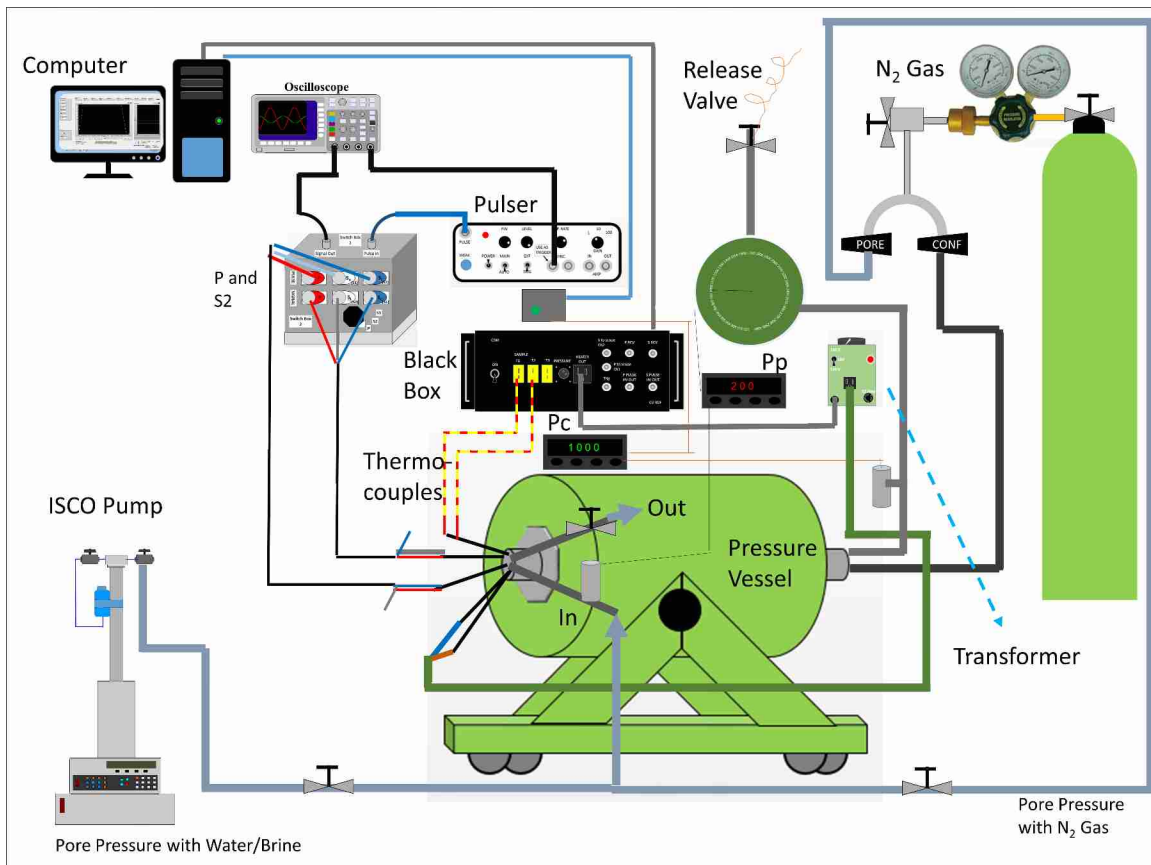


Figure 2.15: High-temperature, high-pressure apparatus for keeping desired pressure and temperature applied to samples while collecting waveform data



Figure 2.16: Stainless steel confining jacket assembly

stainless steel jacket, serving as both the pore pressure source as well as the means to keep the sample saturated for hydrous pyrolysis. During pyrolysis, one capillary is connected to the Teledyne-Isco pump, while the other is closed off to atmospheric pressure, but can be opened in the event of confining pressure leaks into the sample. For anhydrous pyrolysis comparison, the pore pressure will be reduced to atmospheric pressure by plugging the capillary connected to the visco-pump.

The temperature is monitored using K-type thermocouples, attached to a temperature control box (Black Box), which connects to a computer and can be monitored and controlled via a LabView program. Using this program, the temperature can not only be monitored, but also controlled in the starting and end temperatures, the increments, and the length of time at each of those increments of temperature. Two thermocouples are placed on opposite sides of the sample, to ensure that the sample is uniformly heated throughout.

Based on work from Elbaharia [2012], Lithium Niobate (LiNbO_3) transducers were used. These transducers are able to measure compressional and one orientation of shear waves through cylindrical core samples of approximately one inch diameter. Calibrations were performed by heating and collecting compressional and shear waves from a copper sample at 1" diameter, 1" height, , as illustrated in Figure 2.18. This calibration shows that at higher temperatures and over time, the arrival times and amplitudes of the compressional and shear velocities have remained approximately constant for a cylindrical copper sample. Therefore, when implementing this experiment on shale samples, changes in arrival times at higher temperatures are associated with shale property changes, and not equipment or couplant deterioration. A diagram of the LiNbO_3 design is shown in Figure 2.17. Gold foil pieces lie in between the compressional and shear crystal pieces, so as to maximize coupling and reduce noise, while also providing a good electrical contact.

A new implementation into the high-temperature, high-pressure set up is the Black Box. It is designed to be fully automated to monitor and control temperature changes using K-type thermocouples, apply voltage output to a transformer to heat the samples, and acquire waveform data for P-waves and S-waves through cylindrical core samples. Due to complications in the quality of the pulser housed in the Black Box, a separate pulser was implemented into the set up, also shown in Figure 2.15. This system is controlled from a program on the computer next to the set up shown in Figure 2.15.

With this set-up, a user can set the duration at incremental temperature, the start and end temperature, the number of measurement points at each step (i.e., 5 measurements in a 10 minute increment would provide a measurement every two minutes). The measurement at each step includes P and S wave data, temperature information from two thermocouples, and pressure data. However, given that the set up used in this study involved using separate P and S wave measurements and pressure data, the only relevant data points automatically generated in this study is the temperature information.

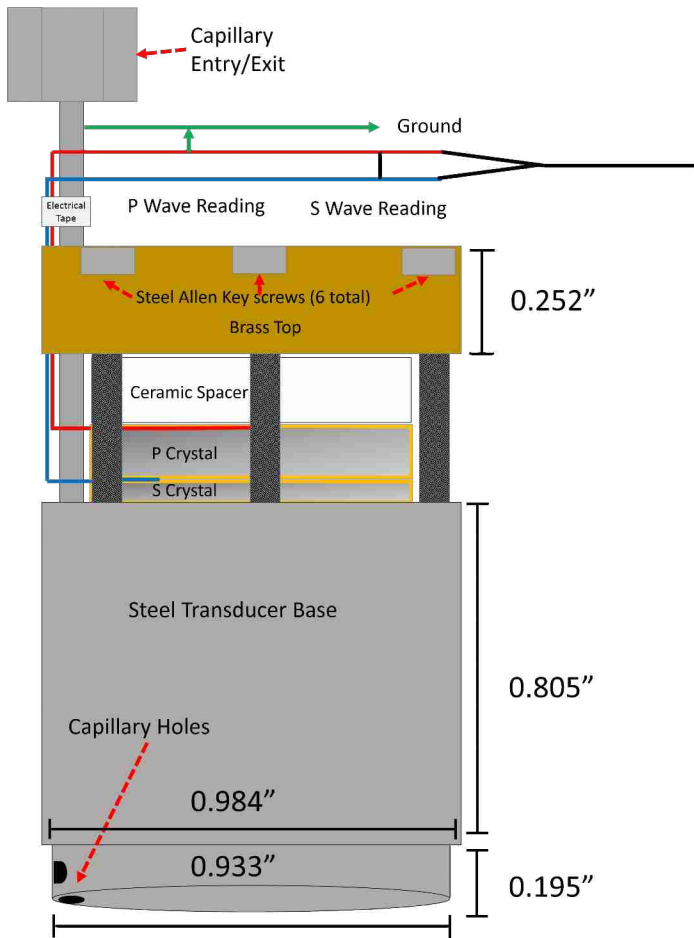
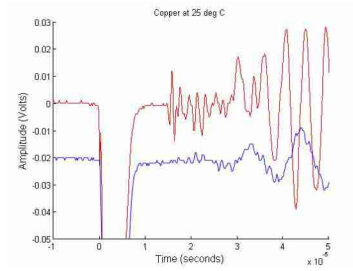


Figure 2.17: Lithium Niobate (LiNbO_3) transducer. Diagram (left) and actual transducer (right)

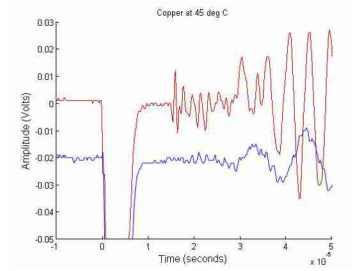
The equipment was calibrated by running the temperature ramp-up event on a cylindrical copper piece. The resulting waveforms are shown below in Figure 2.18, where figures Figure 2.18(a), Figure 2.18(b), Figure 2.18(c), Figure 2.18(d), Figure 2.18(e), Figure 2.18(f), Figure 2.18(g), Figure 2.18(h), Figure 2.18(i), and finally Figure 2.18(j) show waveforms for a copper sample throughout the ramp up process. The Krytox acoustic couplant was a custom-made synthetic lubricant, and was found to be insoluble in water, and therefore could be used in both anhydrous and hydrous pyrolysis. Due to the consistent amplitude held, as well as the similar arrival times to within $0.2\mu s$, we can make the following assumptions:

- The Krytox couplant does not break down at $365^{\circ}C$, on account of consistent amplitude of waveforms and arrival times.
- Equipment is able to stay running for at least 72 hours to run a full experiment
- Transducers remain consistent throughout the experiment

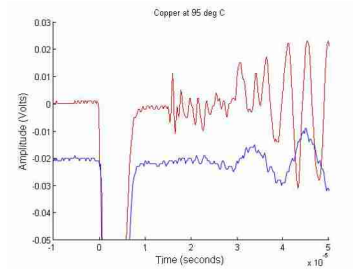
Using the waveforms collected on the copper sample, we can also calibrate the transducers to determine the delay time to an accuracy of no less than 8%. Knowing the exact length of the stainless steel base of the transducers, as well as the length of the copper sample, measure and derive the travel time through the copper sample, to confirm the quality of the waves produced by the transducers and the approximate shapes and phases of the waves at those arrival times. Table 2.1 shows the calculated and measured P and S arrival times, and shows the percent error between the two, which overall increased with higher temperatures. Arrival times were calculated using literature data and known lengths of the samples, and compared to measured data in which the arrival times were picked from plots in Figure 2.18. Due to the similar magnitudes of the amplitude from the waves shown in Figure 2.18, the increase in error is likely caused by the change in properties of the copper sample with temperature increase, as opposed to a decrease in signal quality and accuracy. The error is small enough however, that velocities can be derived from waveforms at temperatures of $365^{\circ}C$ for oil shale samples.



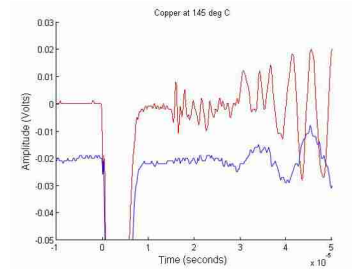
(a) 25C



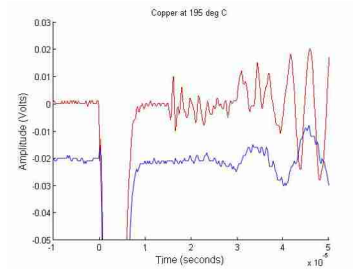
(b) 45C



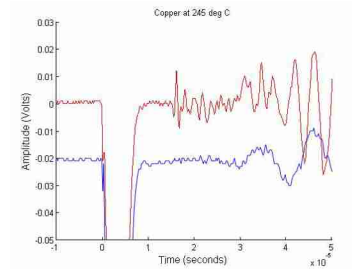
(c) 95C



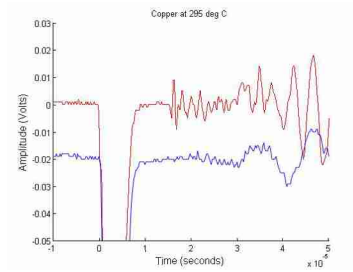
(d) 145C



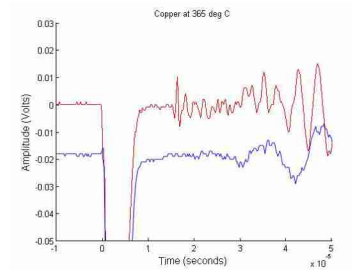
(e) 195C



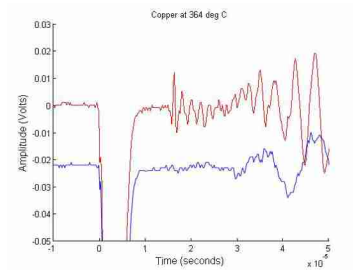
(f) 245C



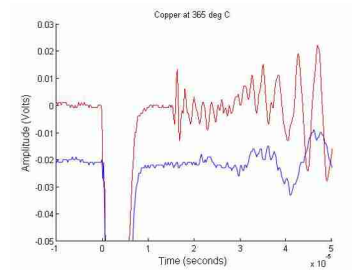
(g) 295C



(h) 365C



(i) 365C for 24 hours



(j) 365C for 48 hours

Figure 2.18: Calibration of Equipment

In summation, the high-temperature, high-pressure experiment is now optimally designed to have improved signal quality, user interface, and accuracy for determining velocities through oil shale samples as a function of temperature.

Table 2.1: Copper Calibration

	Steel	Copper	Total time		
length (km)	5.08E-05	2.54E-05			
Known S Velocity (km/s)	2.775	2.31			
Known P Velocity (km/s)	5.79	4.69			
S Wave Arrival Time (s)	1.83E-05	1.10E-05	2.93E-05		
P Wave Arrival Time (s)	8.77E-06	5.42E-06	1.42E-05		
Temp (deg C)	P Arrival time (s)	S Arrival time (s)	% Error P	% Error S	
25	1.48E-05	2.90E-05	4.30	1.03	
45	1.48E-05	2.90E-05	4.30	1.03	
95	1.48E-05	2.90E-05	4.30	1.03	
145	1.48E-05	2.92E-05	4.30	0.35	
195	1.50E-05	2.92E-05	5.71	0.35	
245	1.52E-05	2.98E-05	7.12	1.70	
295	1.52E-05	3.04E-05	7.12	3.75	
365	1.52E-05	3.06E-05	7.12	4.43	
365	1.52E-05	3.06E-05	7.12	4.43	
365	1.52E-05	3.06E-05	7.12	4.43	

CHAPTER 3

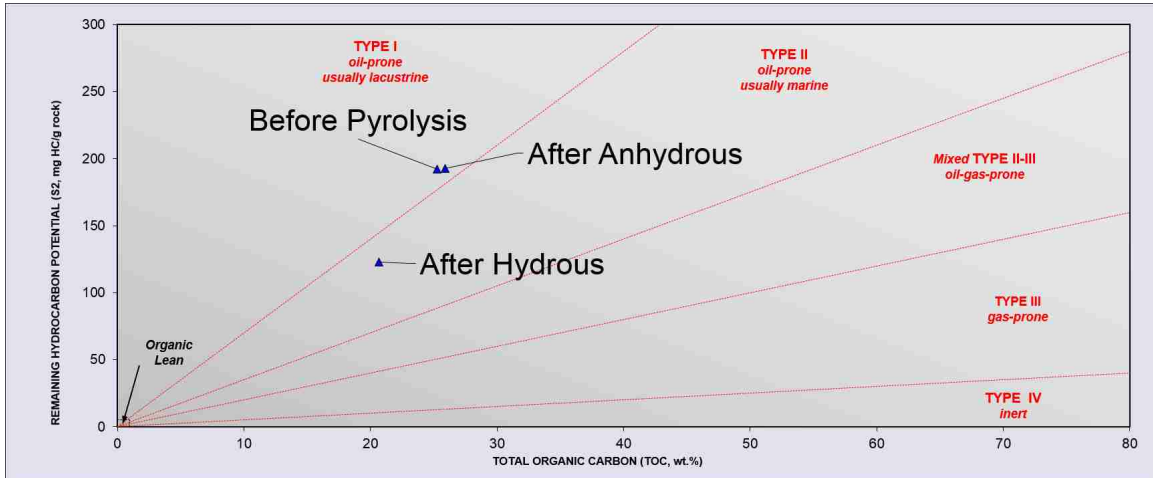
RESULTS

Samples in this study were subjected to numerous tests before and after CSM pyrolysis. When referring to pyrolysis, it is important to differentiate between the long-term 72 hour pyrolysis done at CSM, and the programmed pyrolysis done by Weatherford Labs to determine sample maturity. The pyrolysis done by Weatherford Labs is exclusively for the purpose of testing samples before or after CSM pyrolysis, to determine the change in maturities. Therefore, samples were sent to Weatherford Labs prior to CSM pyrolysis, after anhydrous pyrolysis, and after hydrous pyrolysis. Additionally, no tests were performed on samples after Weatherford pyrolysis, as the samples were destroyed in that process.

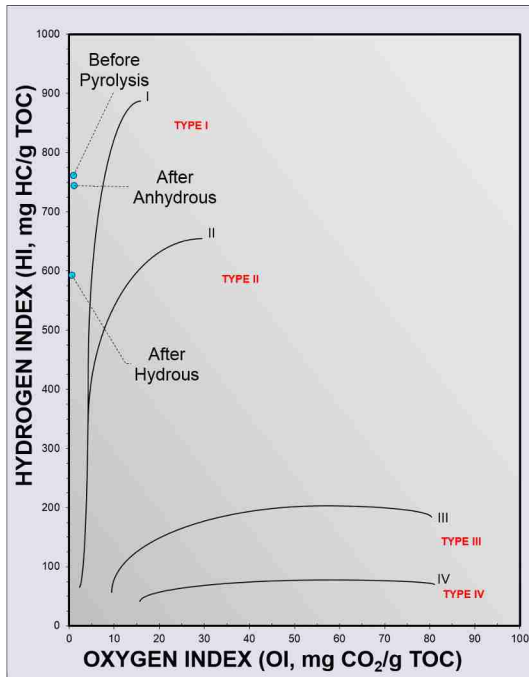
3.1 TOC and SRA Results

Kerogen in the samples is type I, immature, and of lacustrine and/or marine origin, as shown in Figure 3.1(a), Figure 3.1(b), and Figure 3.1(c). Note that for the data presented in Figure 3.1, ‘Before’ refers to the samples as-received before any CSM pyrolysis, while ‘After Anhydrous’ and ‘After Hydrous’ represent Weatherford’s programmed pyrolysis results after those types of CSM pyrolysis. The values from the programmed pyrolysis by Weatherford are also provided in Table 3.1.

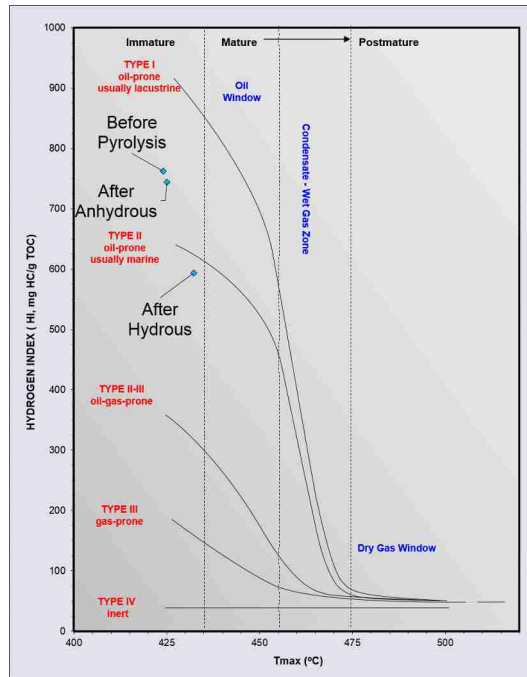
It would have been ideal to take an average of the other samples (45° and 90° , but given the limited size of the samples and the necessary mass to perform different measurements (such as porosity and SEM image acquisition), it was necessary to preserve the other sample orientations for SEM and CT scans. A table of density and porosity values can be found for a routine crushed core analysis done by Weatherford in Table 3.2. However, it is ambiguous as to whether the porosity is accurate, as it is unlikely that the tight, organic rich shale used in these experiments has nearly 10% porosity.



(a) Total Organic Carbon (TOC) vs S₂



(b) HI vs OI



(c) HI vs Tmax

Figure 3.1: Results of Programmed Pyrolysis

Table 3.1: Rock-Eval of Block 003 samples (AR).

Property	Before CSM Pyrolysis	After Anhydrous	After Hydrous
TOC (wt%)	25.27	25.90	20.70
S1 (mgHC/g of rock)	10.01	7.18	21.41
S2 (mgHC/g of rock)	192.37	192.77	122.84
S3 (mgCO ₂ /g of rock)	0.28	0.29	0.13
Tmax (deg C)	424	425	432
HI (mgHC/g of rock)	762	744	593
OI (mgCO ₂ /g of rock)	<1	<1	<1
S2/S3	687	665	945
S1/TOC*100	40	28	103
PI	0.05	0.04	0.15

Table 3.2: Density and Porosity of Block 003 samples (AR).

AR Bulk Density (g/cc)	1.86
AR Press Decay Permeability (md)	1.98E-5
Dry Bulk Density (g/cc)	1.78
Dry Grain Density (g/cc)	1.97
Dry Helium Porosity (% of BV)	9.8
Dry Press Decay Permeability (md)	1.33E-4

Data before pyrolysis is a result of three samples averaged together, of which the standard deviation between values did not go above 1% for all values, except for S2 and subsequently HI, which went to 4 and 6 % standard deviation, respectively. The remaining columns in Table 3.1 for after anhydrous and after hydrous, were taken from 0° oriented samples.

The anhydrous pyrolysis sample has values very similar to those before pyrolysis, such as the TOC, S2, S3 and PI values. However, S1 was reduced, indicating that much more volatile hydrocarbons were released during anhydrous pyrolysis than trapped. Unfortunately, this indicates that for anhydrous pyrolysis to effectively mature the rock artificially and produce better quality hydrocarbons, it is necessary to either heat the oil shale to a higher temperature or push the fluids out, as in hydrous pyrolysis.

Samples subjected to hydrous pyrolysis underwent more significant changes than anhydrous, indicated by values in Table 3.1 and Van Krevlen diagrams in Figure 3.1. S2 values fell considerably, indicating more bitumen to hydrocarbon conversion. Some values increase dramatically for the hydrous pyrolysis, such as S1. This increase makes sense, as the S1 value is a measure of the free/volatile hydrocarbons, but also a measure of kerogen derived bitumen. During pyrolysis, some of the kerogen converted to bitumen, and therefore would increase the overall S1 value, and consequently lower the S2 value. The S3 value is lower from the release of CO₂. Compared to the ‘Before’ and ‘After Anhydrous’ values, the PI indicates that there was less production in mg HC/g rock during Weatherford’s programmed pyrolysis for the ‘After Hydrous’ pyrolysis. The hydrous pyrolysis had a greater effect on the overall maturity of the oil shale compared to the anhydrous.

3.2 XRD Mineralogy Results

It is important to determine the mineralogy of oil shale before and after CSM pyrolysis to determine dominant constituents that could contribute to additional anisotropy. For example, if clays present in the samples were to change drastically, this would interfere with the VTI assumption, as they are a significant part of the horizontal layering of the samples. Additionally, if the mineralogy were to change significantly compared to after pyrolysis, then

it would be much more difficult to make conclusions about the causes in velocity changes associated with hydrocarbon production in oil shale.

Yen [1976] describes Permian age oil shale in southern Brazil as a result of deposition in shallow seas on continental platforms and shelves. It is of siliceous type, darker, and will contain detrital minerals such as quartz, feldspar, and clay. The results of the mineralogy report provided courtesy of Weatherford Labs corroborates this assertion in weight percent (Table 3.3) and volume percent (Table 3.5). Volume percentages were derived by approximating the densities of the constituents (Table 3.4), dividing each constituent by its density, adding up the total volume, and finally dividing the individual constituents by the total volume. ‘Tr’ stands for ‘Trace Amount’, (less than 1% of the total weight or volume percentage, ‘Plag’ stands for Plagioclase Feldspar, and ‘K-Feldspar’ stands for Potassium Feldspar. Because samples only varied by a couple percentage points at most between pyrolysis, we can assume that the mineralogy does not change significantly with pyrolysis, with only about 1-2% being expelled with hydrocarbons. A bar graph of this data is shown in Figure 3.2.

Table 3.3: Mineralogy of Brazilian oil shale samples for Block 003 (weight percent).

Mineral	Before Pyrolysis	After Anhydrous	After Hydrous
Calcite	Tr	0	Tr
Dolomite	1	Tr	1
Quartz	23	22	22
K-Feldspar	10	10	10
Plagioclase Feldspar	18	18	18
Pyrite	10	9	8
Clays	42	38	40

Table 3.4: Assumed densities of minerals in Block 003.

Mineral	Calcite	Dolomite	Quartz	K-Feldspar	Plag.	Pyrite	Clays
Density (g/cc)	2.71	2.84	2.65	2.56	2.68	5.01	2.7

Table 3.5: Mineralogy of Brazilian oil shale samples for Block 003 (volume percent).

Mineral	Before Pyrolysis	After Anhydrous	After Hydrous
Calcite	Tr	0	Tr
Dolomite	0.99	Tr	0.98
Quartz	24.30	23.01	23.13
K-Feldspar	10.93	10.83	10.88
Plagioclase Feldspar	18.80	18.62	18.71
Pyrite	5.59	4.43	5.01
Clays	39.40	43.12	41.28

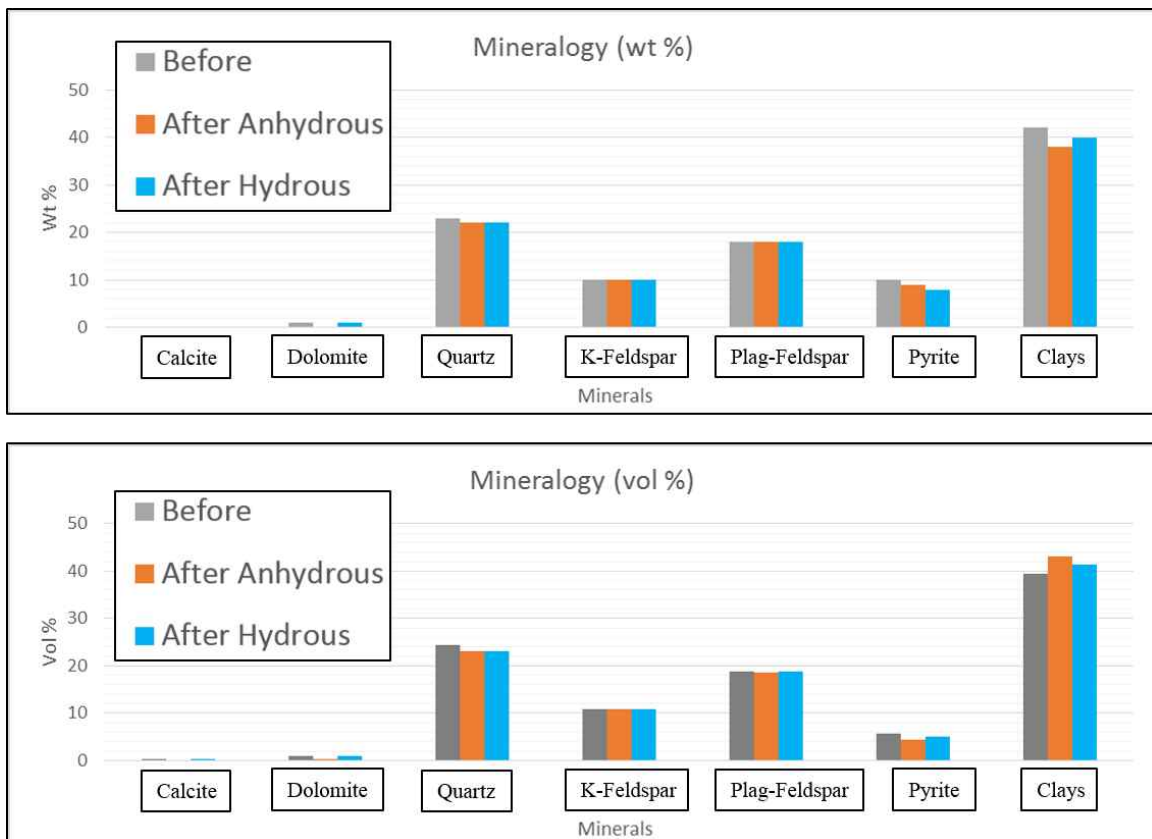


Figure 3.2: XRD mineralogy bar graph.

3.3 Computer Tomography Results

It is important to perform visual inspection at varying levels of resolution on the surface and interior of the samples used. CT scans allow for 3D visualization (Figure 3.3). Scans prior to pyrolysis will help to affirm the bedding plane orientations for stiffness coefficient derivations.

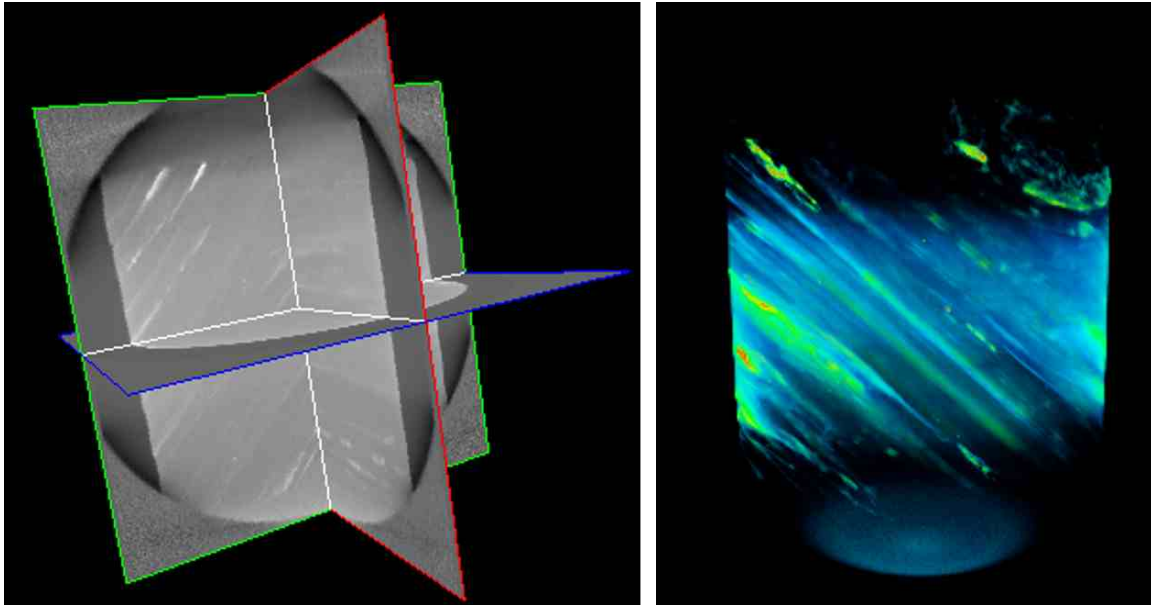


Figure 3.3: Range of 3D CT tomography. Cross sections views (left) which can be moved to view specific parts of the sample, and a 3D volume for overall visualization (right). Sample is approximately 1 inch in diameter in both figures.

While the angle of the layering can be accounted for in the C_{13} stiffness coefficient as shown in equation 2.12, the fact that the angle varies can greatly affect the measurements based on the stiffness coefficients. To illustrate this effect, we have utilized equation 2.12 for bedding angles ranging from 40-50°, assuming a density of 1.86 g/cm³, along with assumed velocities, and plotted the resulting C_{13} and δ values as a function of angle, for as-received samples, in Figure 3.4. Figure 3.4(a) and Figure 3.4(b) shows the dependence of C_{13} and δ as a function of bedding angle, respectively.

The red dots correspond to the values if the actual angle of the bedding throughout the sample was 42° or 48° (calculated using equation 2.12), while the green dot corresponds to

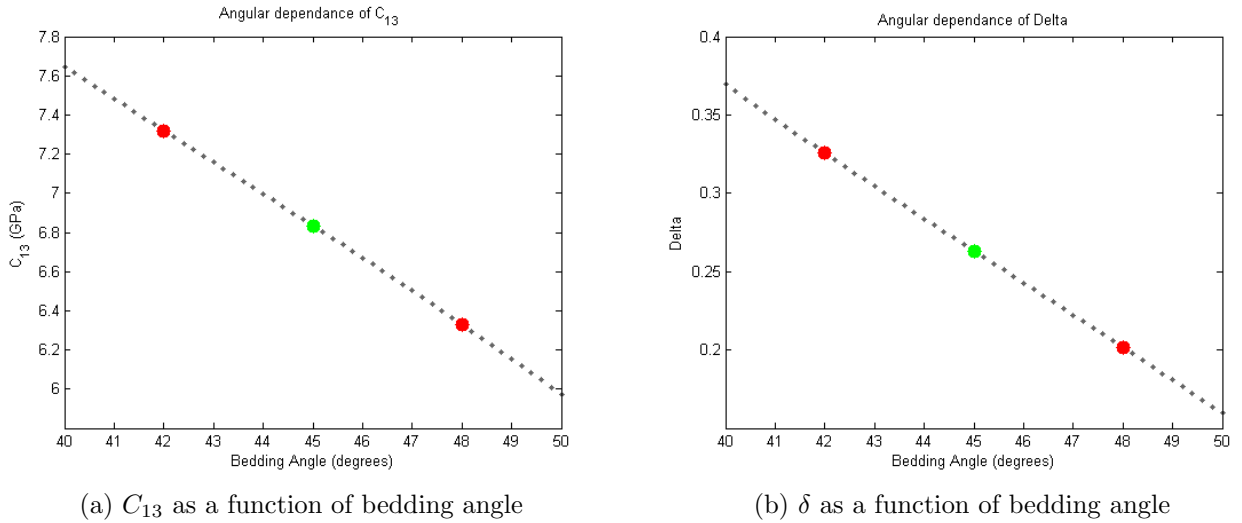


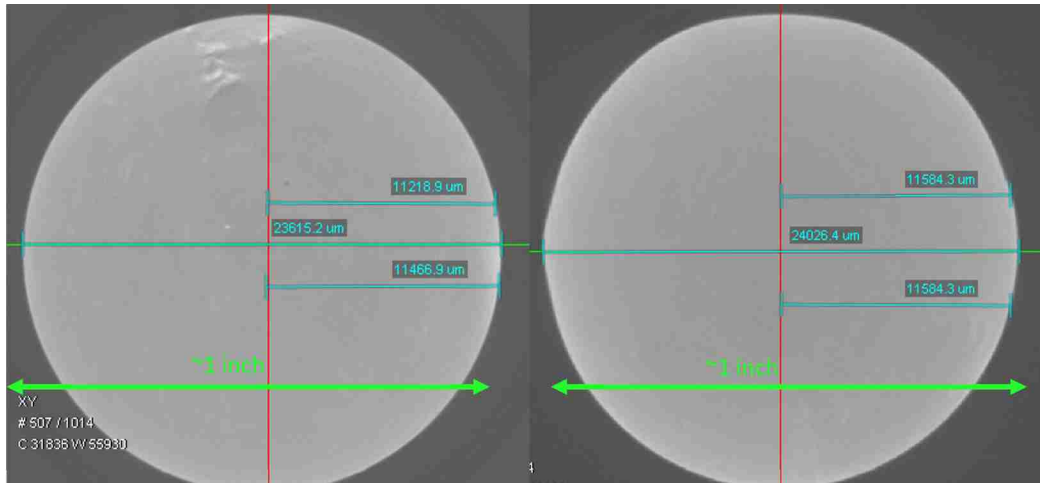
Figure 3.4: C_{13} and δ vs. bedding angle

the assumed 45° of the angled sample. The gray dotted lines are other possible data points at various bedding orientations. Assuming the green dot represents the assumed bedding angle, and either of the red dots represent the actual angle, errors as high as 21% can occur in the measurements for the δ parameter if the bedding angle in the samples is incorrectly assumed to be 45° . Therefore, proper angle calculation is vital.

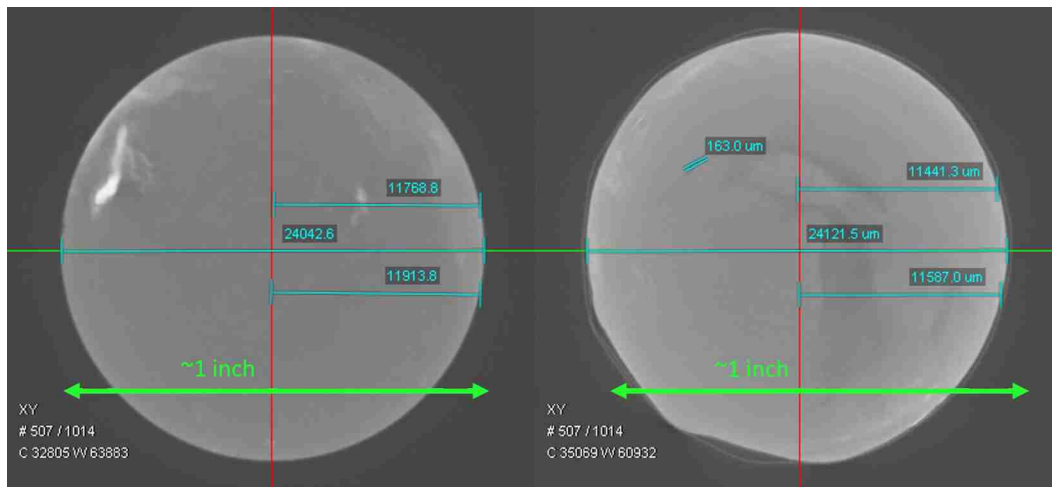
Figure 3.5 is shown below, containing before and after anhydrous top view cross sections (Figure 3.5(a) and Figure 3.5(b)). The top view cross section of the 0° samples do not show all bedding planes. It is important to note however, the dark fracture spot on the after view of hydrous pyrolysis, as well as a small fracture approximately $163\mu m$ wide formed perpendicular to the bedding plane.

For the 45° and 90° samples, bedding planes are visible in top cross section views, (Figure 3.6 and Figure 3.7). There is little difference for anhydrous deformation and fracture development in Figure 3.6(a) or Figure 3.7(a). On the other hand, Figure 3.6(b) and Figure 3.7(b) have comparatively significant fracture development and deformation. It is important to note however that for top views of cross sections that radial deformation is subject to error, especially with the hydrous pyrolysis samples. This is due to the slight variations

in sample height between measurements, shifting the exact placement of the cross section.



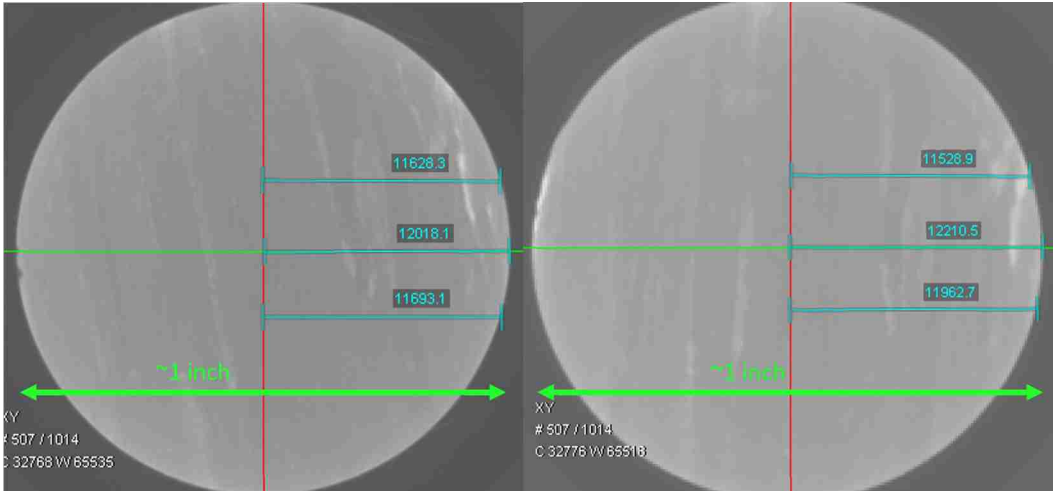
(a) 0° sample before and after anhydrous pyrolysis



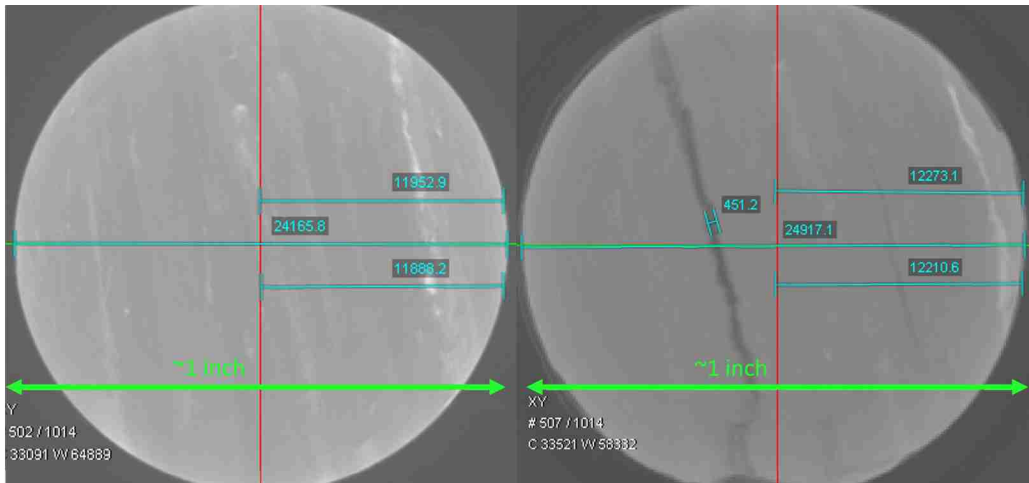
(b) 0° sample before and after hydrous pyrolysis

Figure 3.5: CT scans of 0° top view cross sections before and after

Using the side cross sectional views in Figure 3.8, Figure 3.9, and Figure 3.10, a more accurate radial change can be quantified. As shown in the hydrous samples of Figure 3.8(b), Figure 3.9(b) , and Figure 3.10(b), the ‘ribbing’ effect due to the sample expanding into the sides of the confining jacket causes a wavy looking edge effect. Therefore, it is important to measure changes in the peak and trough of these waves to get a range of expansion. The hydrous samples show a great deal of fracturing, as well as internal bedding deformation.

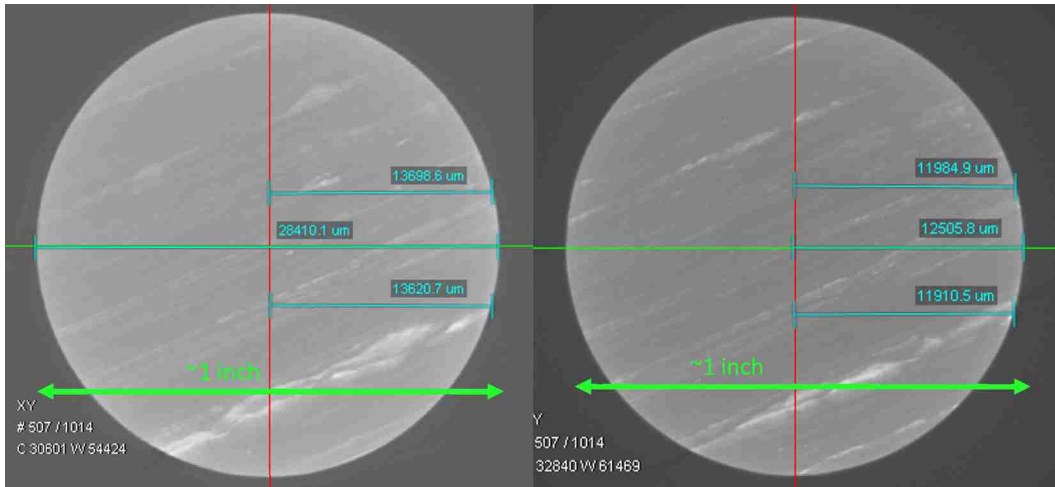


(a) 45° sample before and after anhydrous pyrolysis

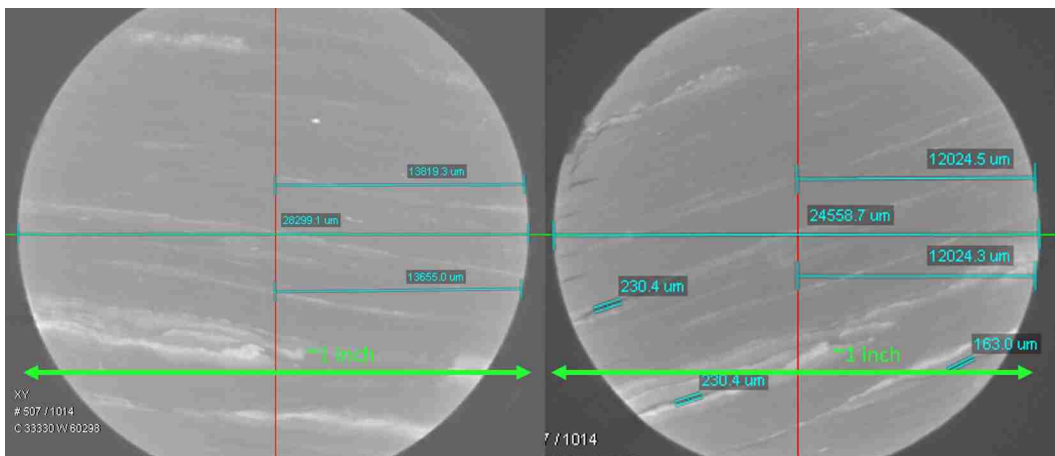


(b) 45° sample before and after hydrous pyrolysis

Figure 3.6: CT scans of 45° top view cross sections before and after



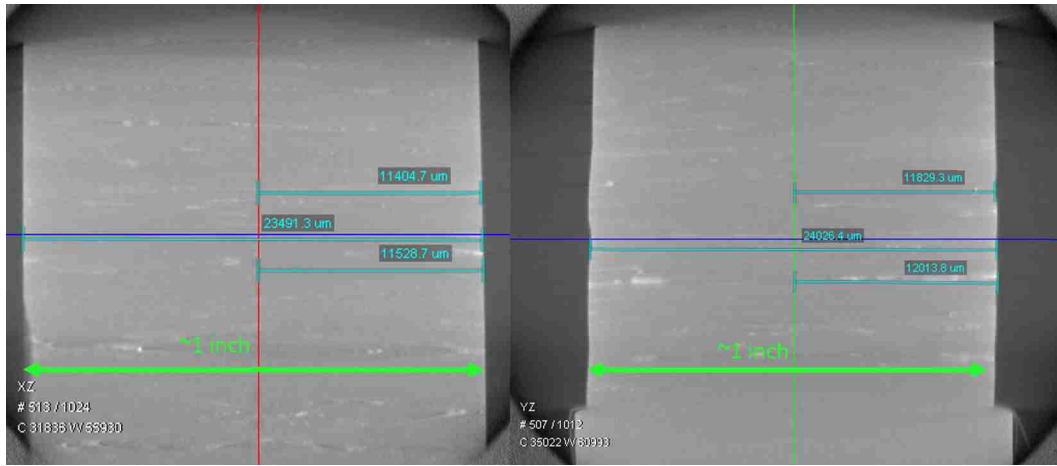
(a) 90° sample before and after anhydrous pyrolysis



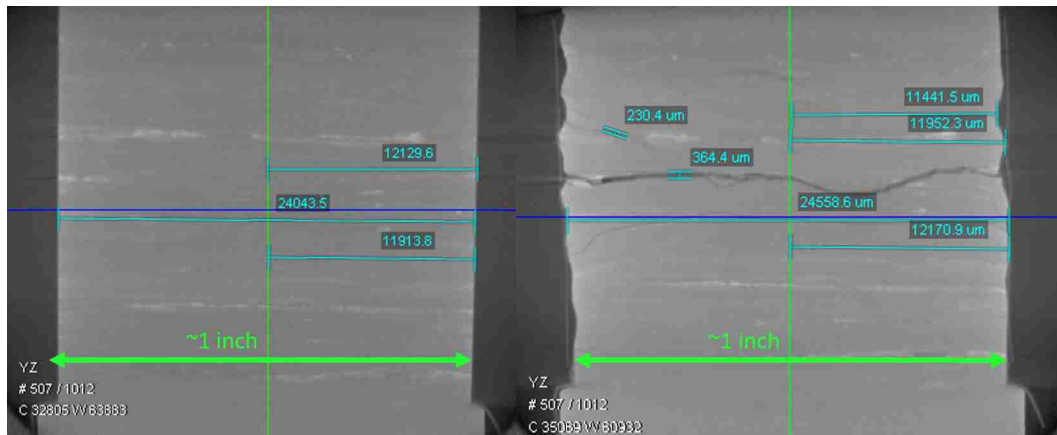
(b) 90° sample before and after hydrous pyrolysis

Figure 3.7: CT scans of 90° top view cross sections

For the anhydrous samples, Figure 3.8(a) and Figure 3.9(a) show some lateral distortions, with no visible fracture planes. The anhydrous pyrolysis of the 90° sample shown in Figure 3.10(a) has error in it's measurements from before pyrolysis, as the length before pyrolysis is over one mm larger, which is highly unlikely especially given the lack of overall sample deformation.



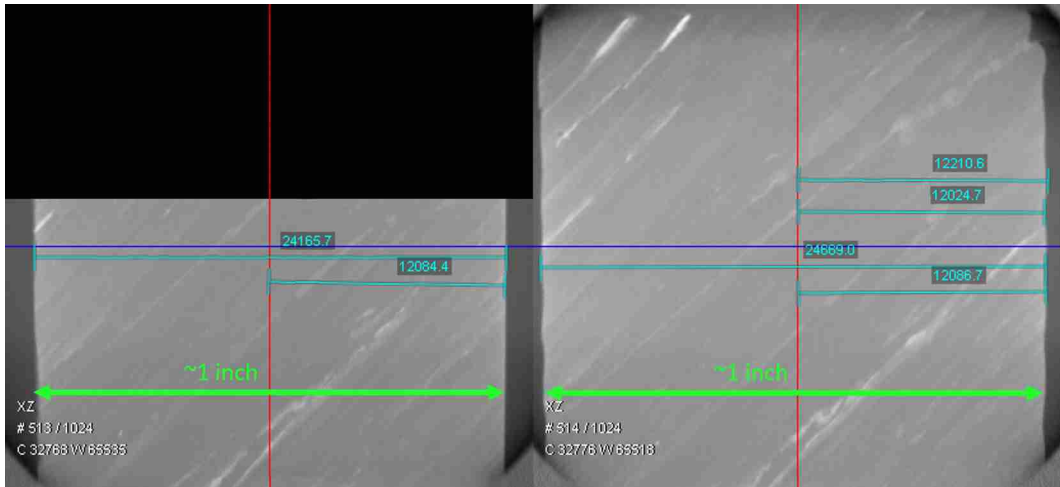
(a) 0° sample before (left) and after (right) anhydrous pyrolysis



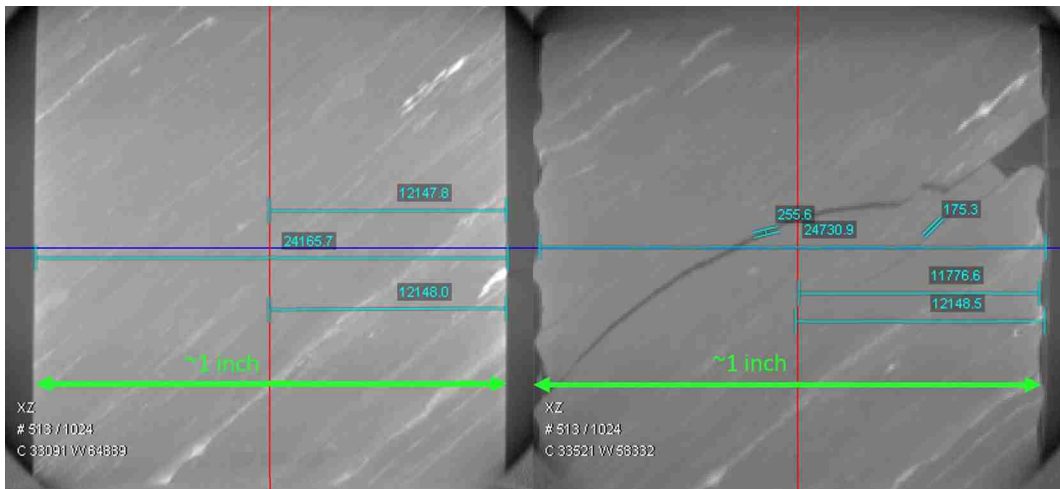
(b) 0° sample before (left) and after (right) hydrous pyrolysis

Figure 3.8: CT scans of 0° side view cross sections

To ensure that the 45° sample was in fact cored at the correct angle to bedding, calculations were performed based off of the CT scans. We use the hydrous 45° sample prior to pyrolysis as an example of how to measure the angle exactly in the bedding plane using micro CT images, and determine the angle the same way a true dip is derived from an apparent

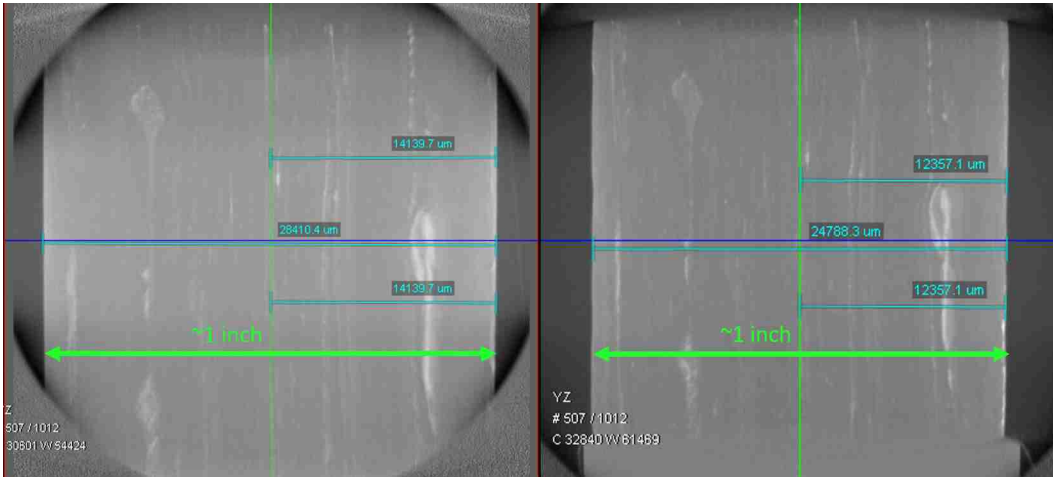


(a) 45° sample before (left) and after (right) anhydrous pyrolysis

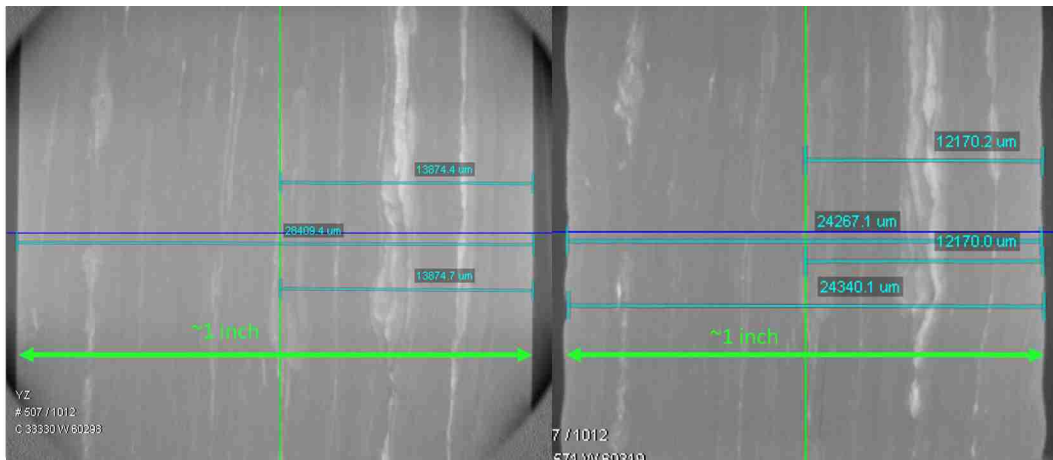


(b) 45° sample before (left) and after (right) hydrous pyrolysis

Figure 3.9: CT scans of 45° side view cross sections



(a) 90° sample before (left) and after (right) anhydrous pyrolysis



(b) 90° sample before (left) and after (right) hydrous pyrolysis

Figure 3.10: CT scans of 90° side view cross sections

dip in larger scale rock strata. First, the angle between the observed cross section and the cross section with the true dip must be determined (Figure 3.11), and this angle was found as 80.1° . Next, it is important to know what the apparent dip of the bed is in the cross section we observe (Figure 3.12). From this information, the true dip was calculated to be 45.02° , close enough to assume a perfect 45° angle. The other CT images likewise proved that we did have 0° and 90° angles on the other samples, giving the three angles necessary to calculate stiffness coefficients based on the VTI assumption.

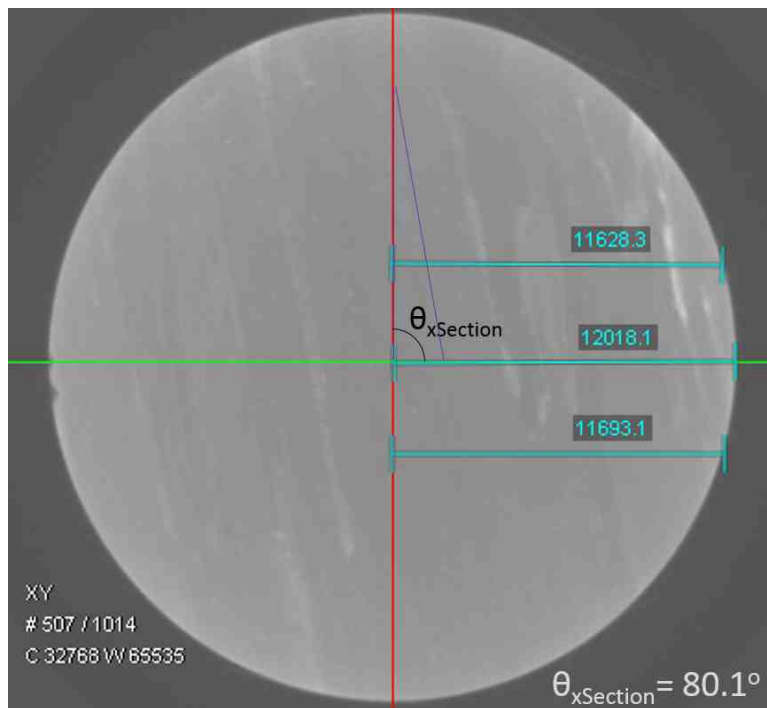


Figure 3.11: Angle between cross section and line perpendicular to bedding plane

3.4 SEM Results

To examine the pore throat size, kerogen composition, and relative grain sizes in the matrix of the rock, image data from an Environmental Scanning Electron Microscope (ESEM) and a Field Emission Scanning Electron Microscope (FESEM) were collected.

A series of images from the ESEM is shown below. Figure 3.13 shows what the sample looks like at the lowest magnification view. Layering and lineaments are observed, with white

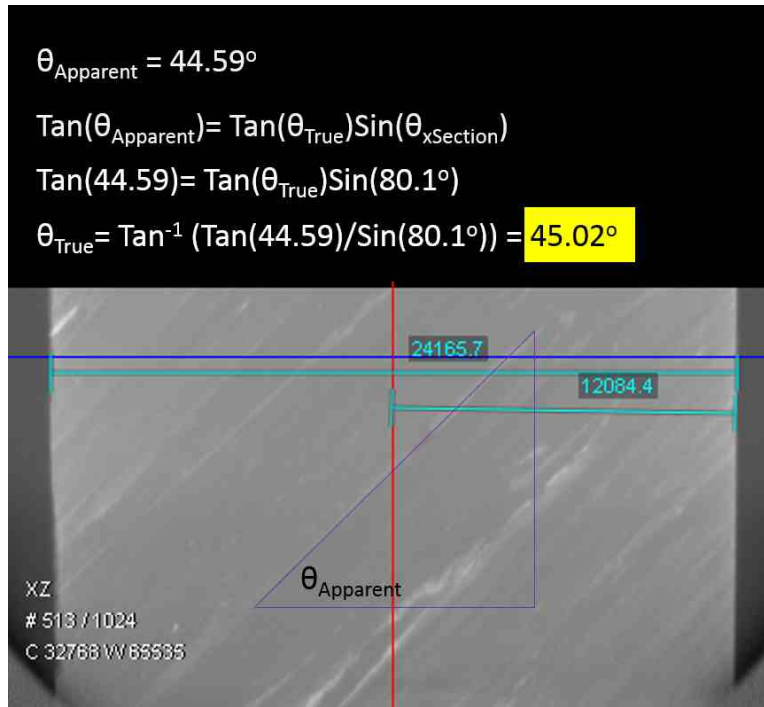


Figure 3.12: Apparent dip used to calculate the true dip of the bedding plane

areas being of higher density compared to darker areas. Looking more closely (Figure 3.14), we see that some of the brighter lineations include white nodules, clay and quartz layering, and organic matter (darkest areas). At 100x magnification Figure 3.15, we can more clearly make out the white nodules as pyrite framboids.

A first look at the samples using ESEM reveals noticeable differences between the effects of hydrous vs. anhydrous pyrolysis (Figure 3.16). Figure 3.16(a) exhibits similar features to before pyrolysis, but with an example of a recently opened pore space. Figure 3.16(b) on the other hand shows the sample surface mostly covered by a layer of bitumen flow. Heavy fracturing is shown, which is likely cracks in the bitumen surface as a result of rapid cooling rather than visible fracture porosity in the sample.

FESEM images also provide more detailed visual inspection for pore sizes. Figure 3.17 shows some pre-existing porosity and pore throat sizes. Anhydrous pyrolysis did not have significant fracture development and kerogen to bitumen conversion compared to hydrous pyrolysis. Figure 3.18 shows some bitumen flow present, but not consistently. Looking closer

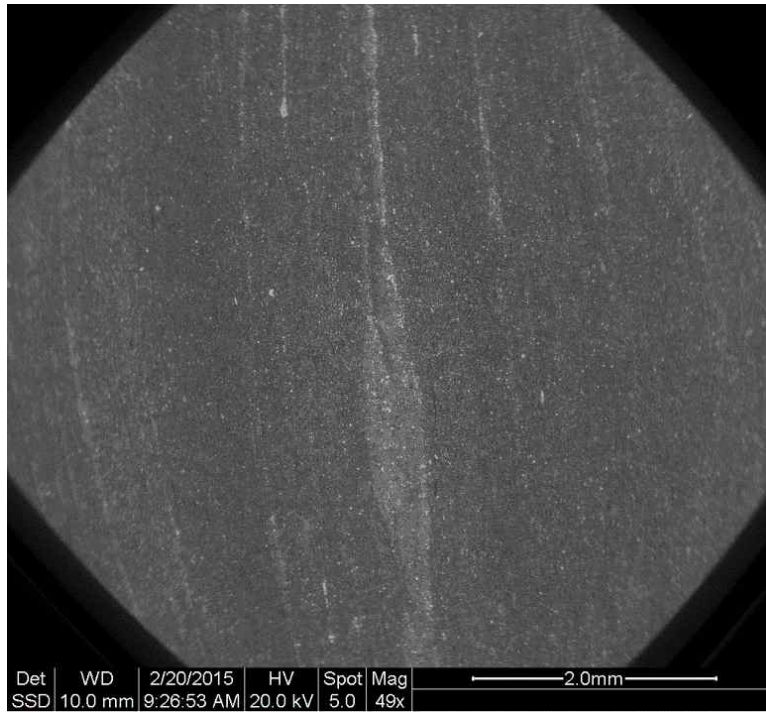


Figure 3.13: Pre-pyrolysis sample ESEM, 49x magnification

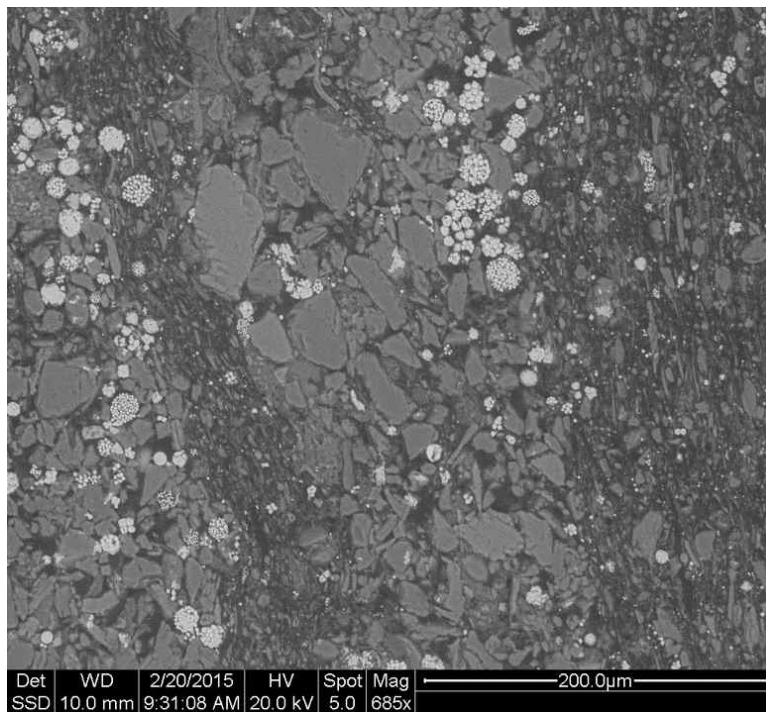


Figure 3.14: Pre-pyrolysis sample ESEM, 685x magnification

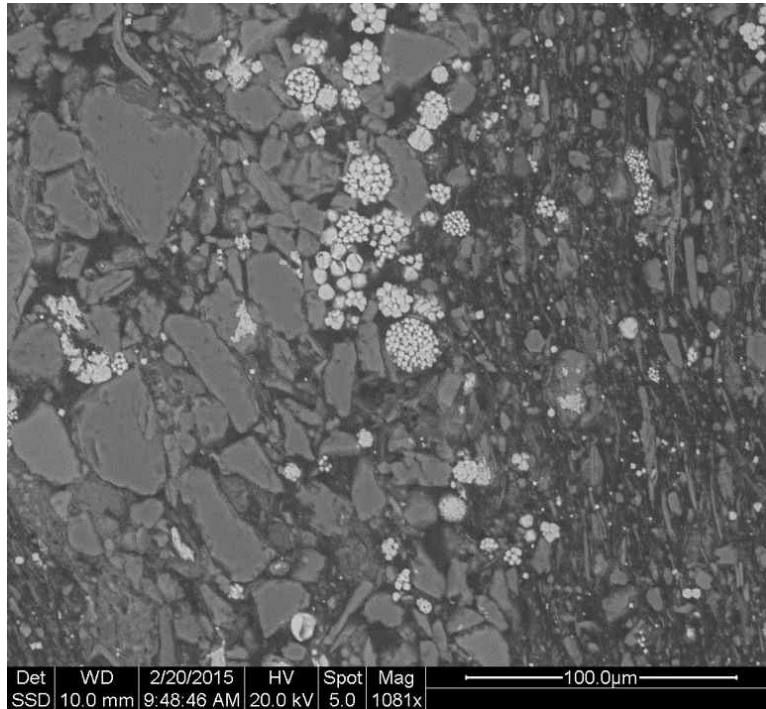
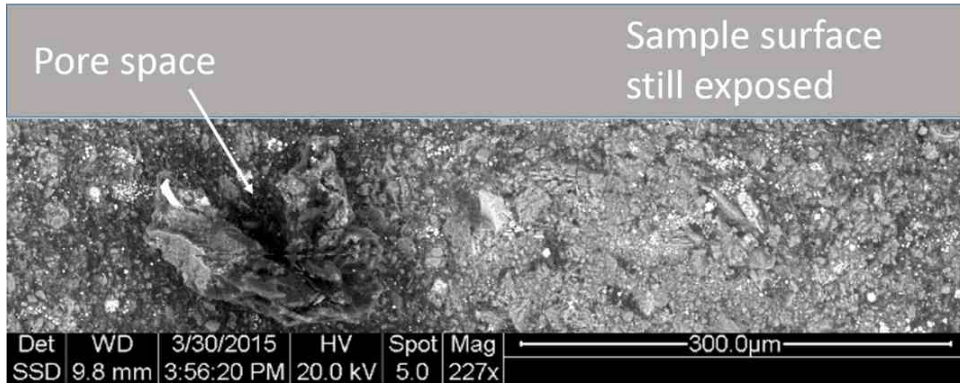


Figure 3.15: Pre-pyrolysis sample ESEM, 1081x magnification

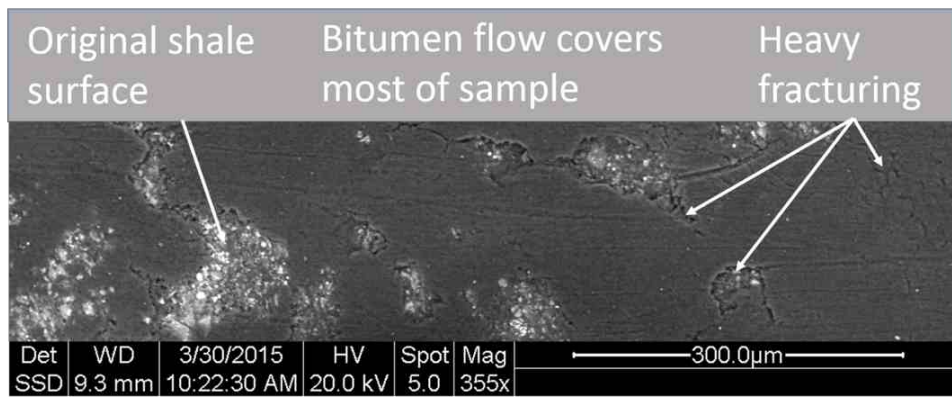
(Figure 3.19), we see a range of pore sizes, which are slightly larger than the pore throat sizes observed in the oil shale prior to pyrolysis.

Hydrous pyrolysis on the other hand shows more fracture porosity development (Figure 3.20). This particular fracture is a few μm in width throughout, shown in Figure 3.21. At higher resolution (Figure 3.22) there is observable fracture porosity and kerogen to bitumen conversion.

Energy dispersive x-ray spectrometer (EDS) was used to confirm the mineralogy seen in the FESEM images (Figure 3.23). Figure 3.23(a) shows the image used, and the points at which data was taken. We see that Figure 3.23(b) has a very high sulfur content, representing the pyrite framboid, and likewise, Figure 3.23(d) shows a high amount of silica and oxygen, which comprises the quartz grains observed. The more difficult data to interpret is over the darker, likely clay and/or organic rich area (Figure 3.23(c)). Several different elements are observed over the clay area, including oxygen, silica, phosphorous, and calcium. Likely, some of these peaks are actually different minerals, but a more refined XRD would be necessary



(a) ESEM 45° sample before and after anhydrous pyrolysis



(b) ESEM 45° sample before and after hydrous pyrolysis

Figure 3.16: ESEM of samples after pyrolysis results from anhydrous pyrolysis (a) and hydrous pyrolysis (b)

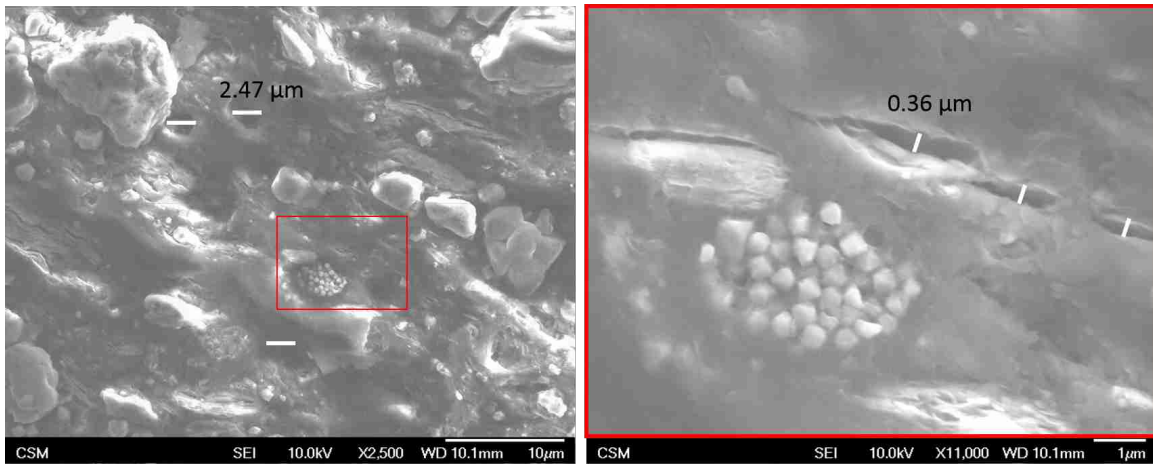


Figure 3.17: Pre-pyrolysis sample FESEM 10 μ m and 1 μ m. Example of pore throat sizes (left), and existing fracture porosity (right)

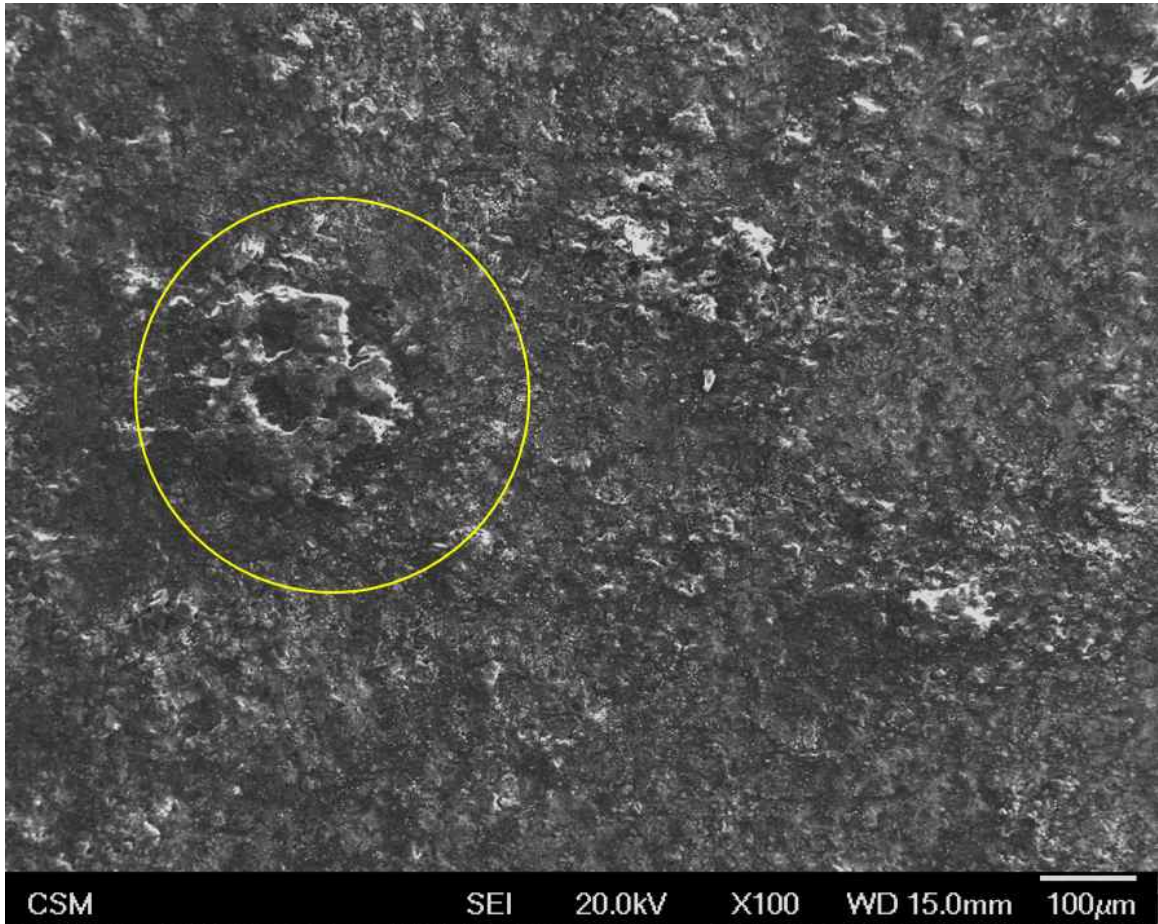


Figure 3.18: Post-pyrolysis (anhydrous) sample FESEM $100\mu m$. Bitumen flow is outlined in yellow.

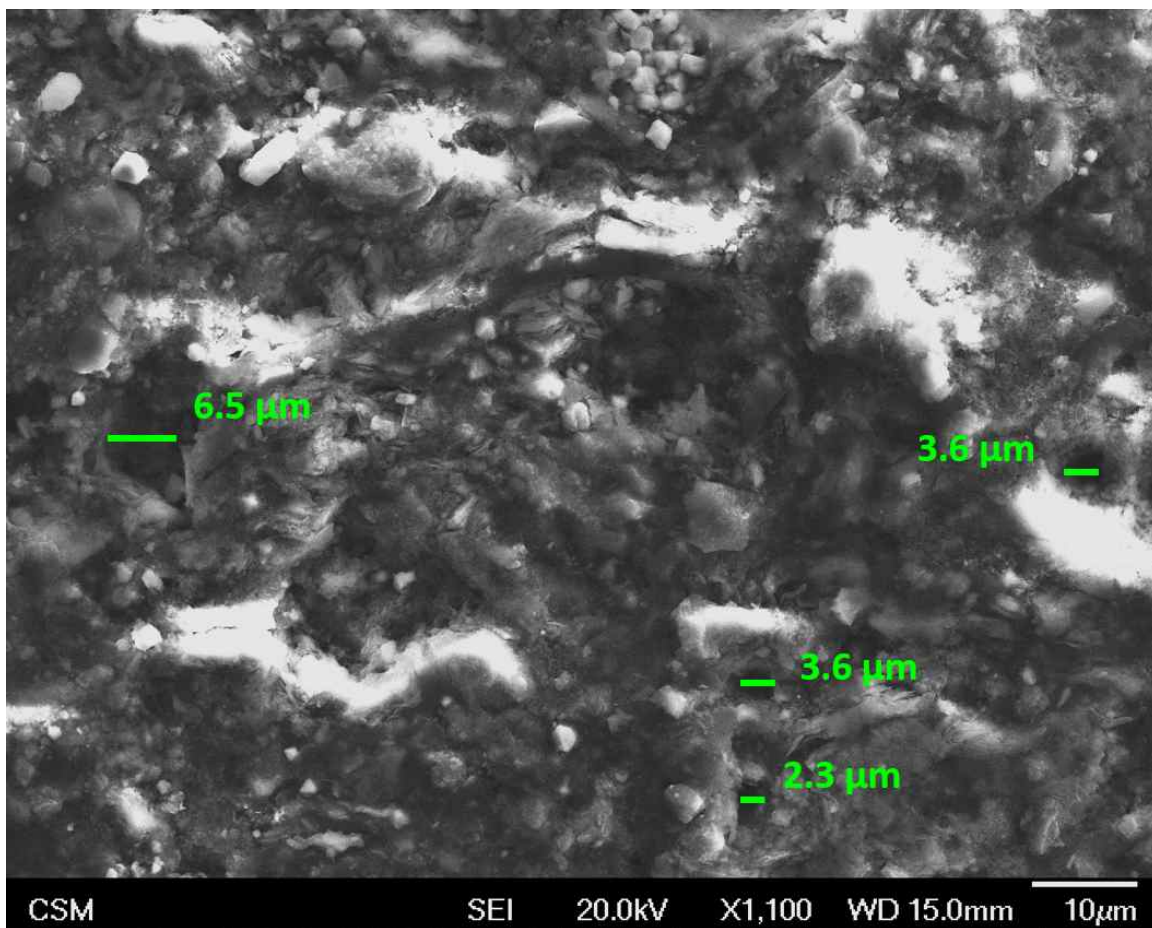


Figure 3.19: Post-pyrolysis (anhydrous) sample FESEM $10\mu m$. Pore sizes range from $2\mu m$ to $6\mu m$.

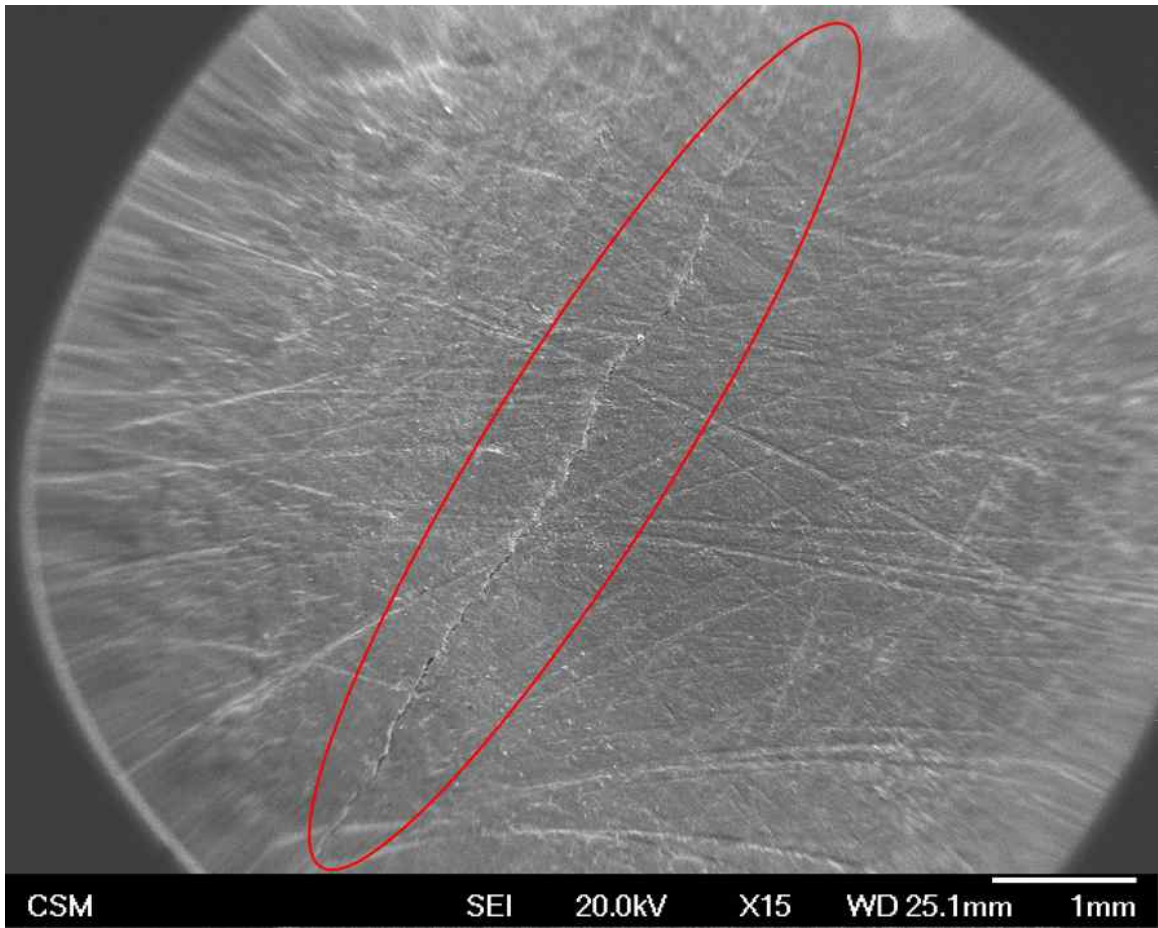


Figure 3.20: Post-pyrolysis (hydrous) sample FESEM 1mm. Fracture is outlined in red.

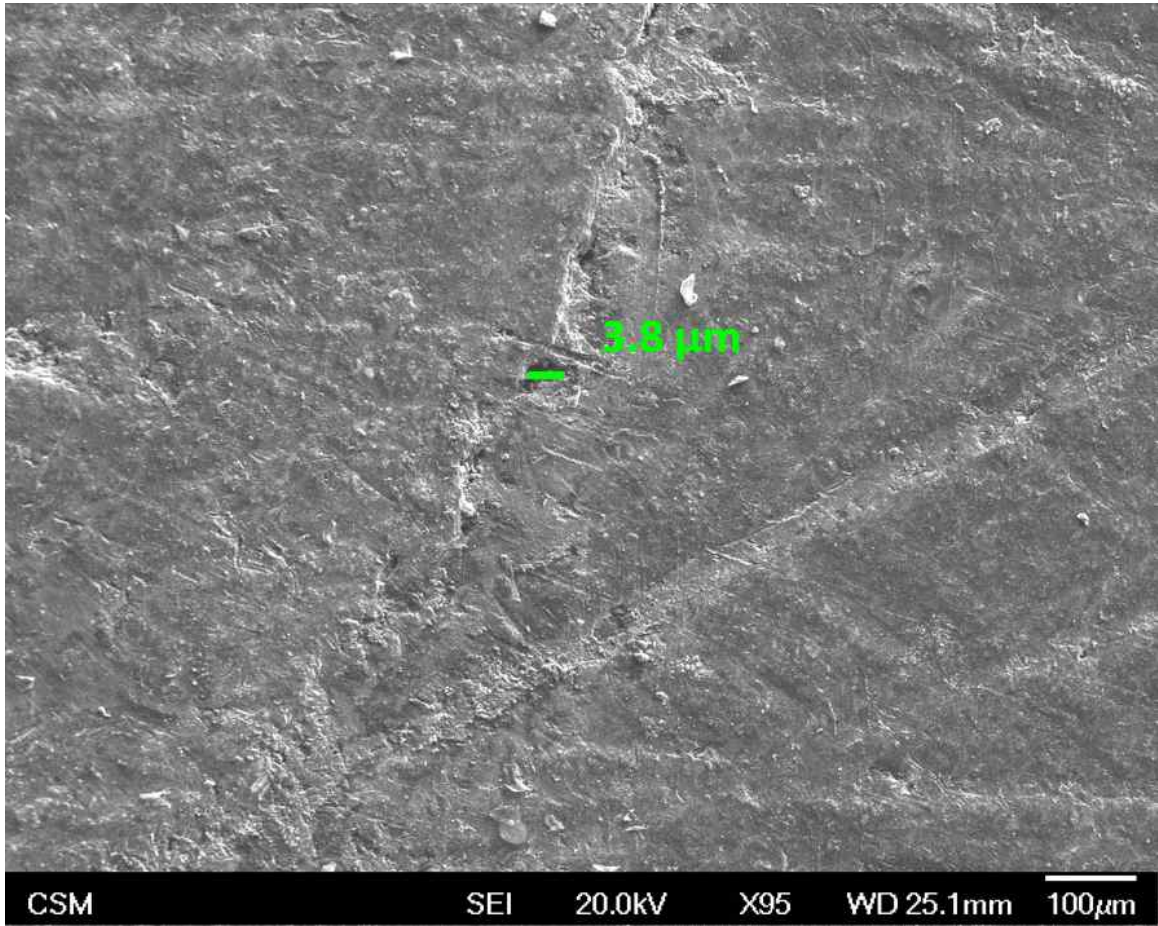


Figure 3.21: Post-pyrolysis (hydrous) sample FESEM 100 μm .

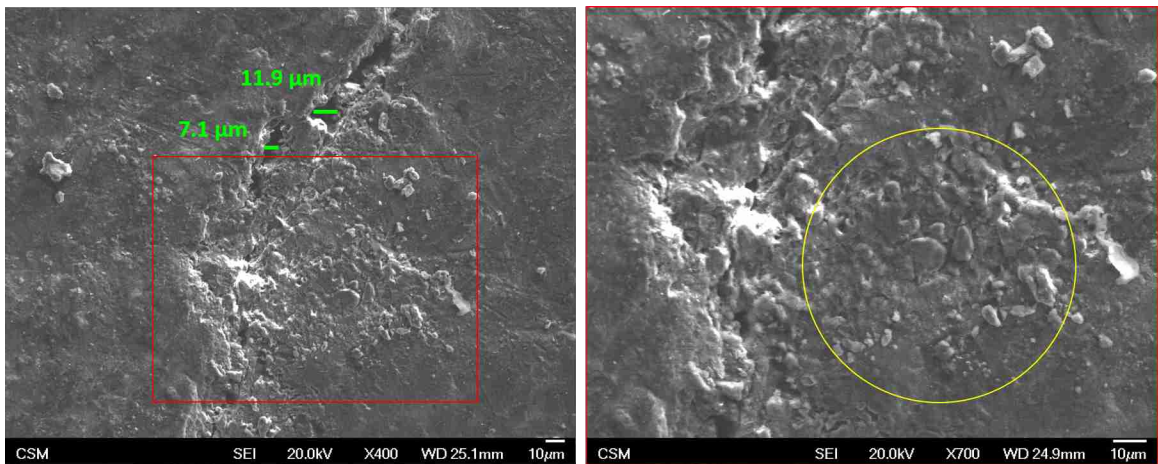


Figure 3.22: Post-pyrolysis (hydrous) sample 10 μm . FESEM 400x magnification with fracture porosity (left), and 700x magnification showing bitumen outlined in yellow (right).

to determine overall composition in the oil shale to compare with the EDS data. We can assume that what we see here is in fact differences between the main constituents of the oil shale: clay, organic matter, quartz, and pyrite.

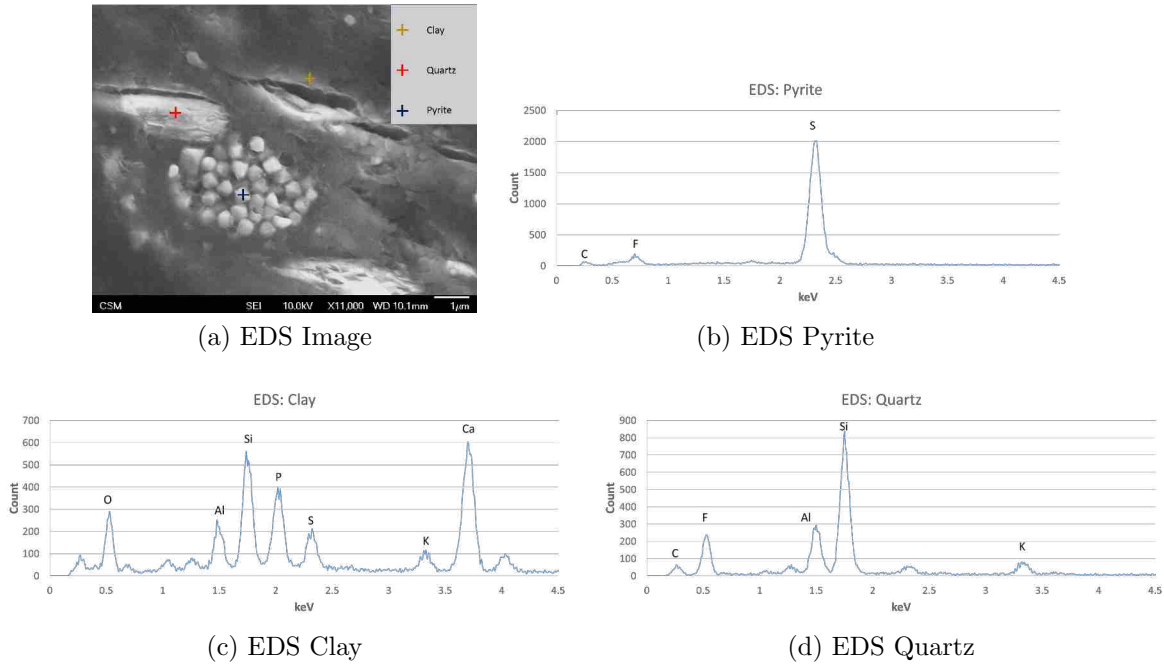


Figure 3.23: EDS showing pyrite (b), clay(c), and quartz (d).

3.5 Waveform Analysis and Results

As discussed in section 2.5, elastic moduli and Thomsen parameters were derived from velocity and density data. Because the mineralogy of the oil shale remained constant throughout pyrolysis, it is assumed for the following calculations that bulk density remains constant throughout the experiment at 1.86 g/cm^3 . The bulk modulus, vertical shear modulus, vertical Poisson's ratio, ε , γ , and δ provided the most relevant data, and are therefore the focus of the results.

Most velocities were picked based on the first arrival of the compressional and shear waveform. Due to the extreme conditions of the experiment, the equipment would occasionally malfunction at higher temperatures. These issues in addition to a finite amount

of rock sample (Block 003) required some extrapolation from real data to have a complete data set. The full data set required having information at each temperature step from the ramp up portion (25°C to 365°C) and the cool down portion (365°C to 25°C), as well as data during the hold portion (365°C for 48 hours). Therefore, for one anhydrous experiment and several of the hydrous experiments, it was necessary to extrapolate some data at higher temperatures and on the cool down portions from existing data found based on trend-lines and/or interpolation from the available data. Compressional velocities are available for all three symmetry orientations (Figure 3.24 and Figure 3.25), and shear velocities are available for samples cored 0° and 90° to the symmetry axis (Figure 3.26 and Figure 3.27).

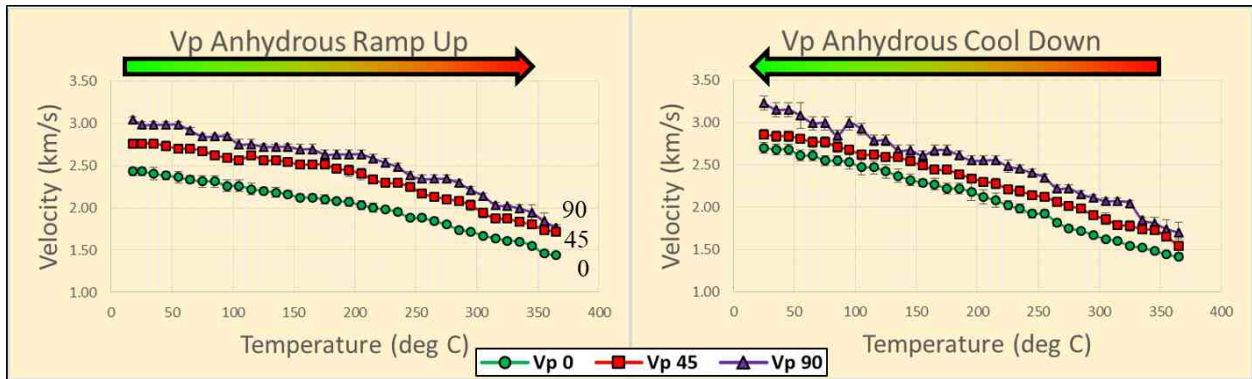


Figure 3.24: Ramp up and cool down plot for anhydrous pyrolysis compressional velocities for samples cored 0°, 45°, and 90° to the symmetry axis.

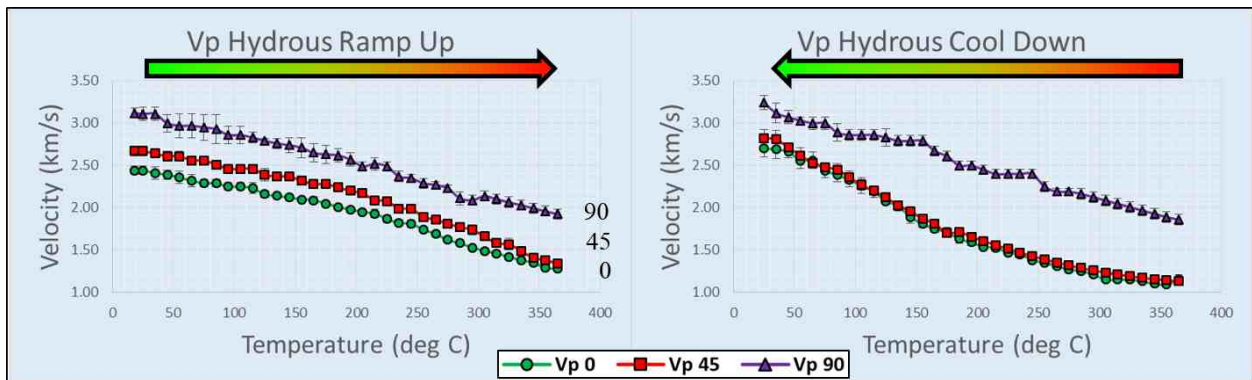


Figure 3.25: Ramp up and cool down plot for hydrous pyrolysis compressional velocities for samples cored 0°, 45°, and 90° to the symmetry axis.

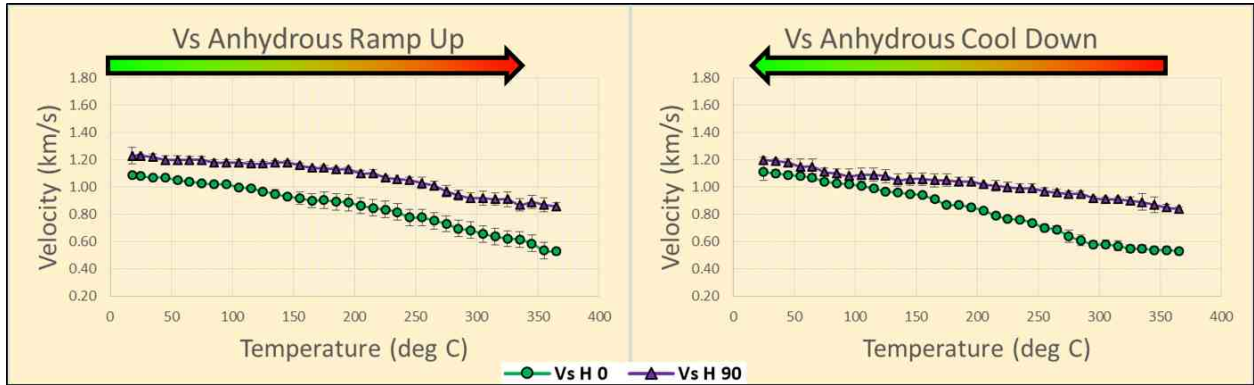


Figure 3.26: Ramp up and cool down plot for anhydrous pyrolysis shear velocities for samples cored 0° , and 90° to the symmetry axis.

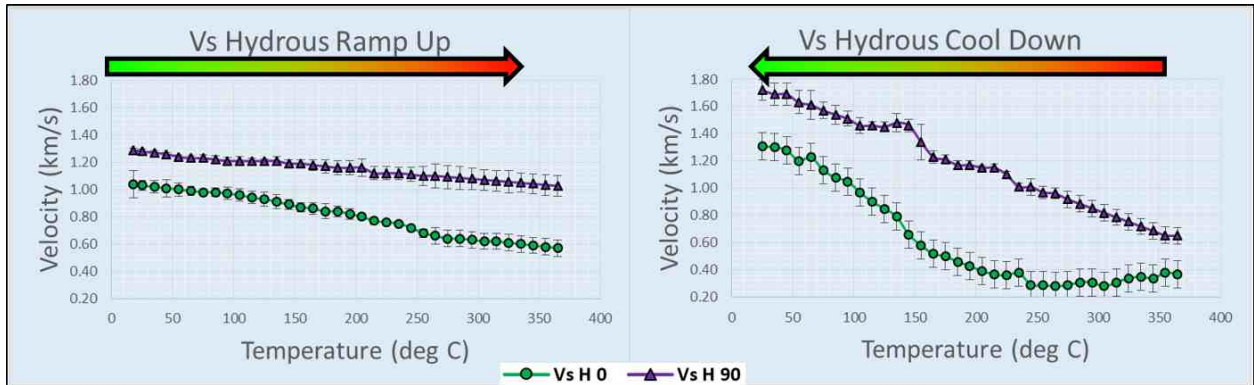


Figure 3.27: Ramp up and cool down plot for hydrous pyrolysis shear velocities for samples cored 0° , and 90° to the symmetry axis.

For the moduli, an overall linear decrease in the data with increase in temperature was observed for both the ramp up and cool down portions of the experiment. It is assumed for the following plots that all moduli are a result of the points within the error bars shown in the velocity plots. The moduli are different measures of a rock's resistance to deformation, and the higher the temperature, the more ductile the oil shales become, and therefore it takes less force to result in deformation. These trends are observed in the bulk modulus (Figure 3.28) and shear modulus (Figure 3.29).

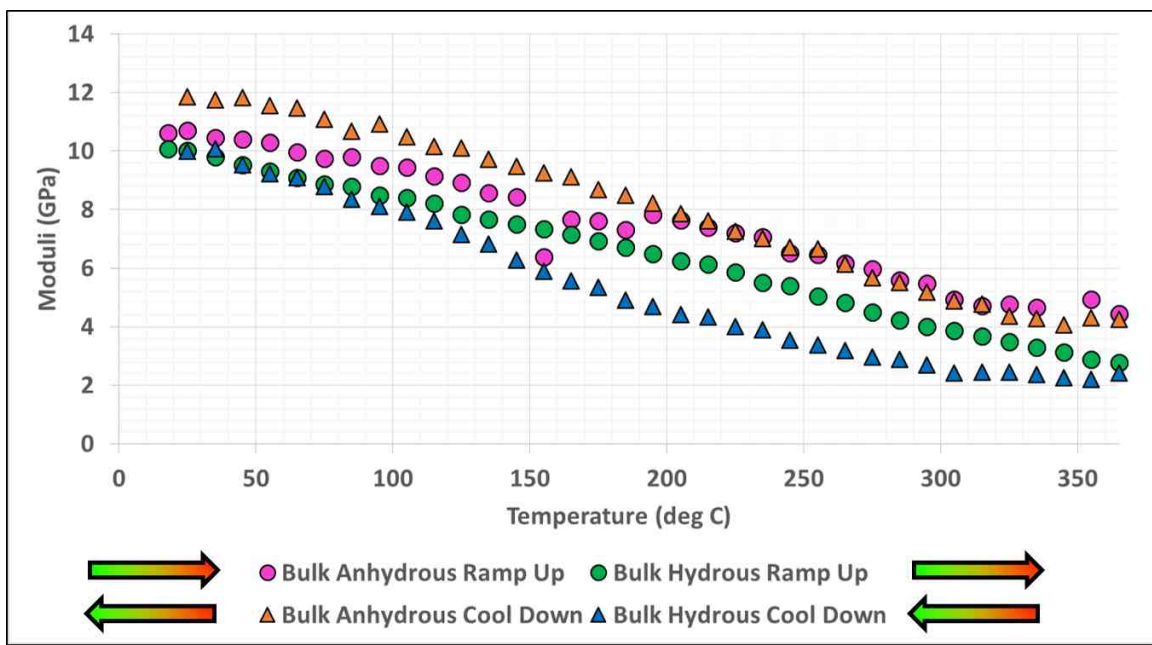


Figure 3.28: Bulk modulus as a function of temperature

There are few differences in the trend-line of the bulk modulus, aside from the hydrous pyrolysis trends being consistently lower than their ramp up counter-parts. For both hydrous and anhydrous experiments, the bulk modulus is lower at higher temperatures during the cool down compared to the ramp up. However, as the temperature decreases back down from 365, the bulk modulus for the cool down portions actually becomes higher than that of the ramp up portion. This can be explained by the fact that during the ramp up portion, the oil shale became more compressible overall. After 48 hours under high temperature, samples became more compressible for both hydrous and anhydrous conditions. During this time,

some hydrocarbons and other organic matter were likely expelled from the samples. For the anhydrous pyrolysis, this resulted in an overall higher bulk modulus upon completion of the experiment, as some of the more compressible organic constituents of the oil shale were removed from the now closed pore spaces in the rock. A similar phenomena is seen in the hydrous experiments, but the crossover does not occur until near room temperature. This can be explained by the brine keeping the pore space open for a longer period of time, resulting in the rock having a lower bulk modulus for a longer duration.

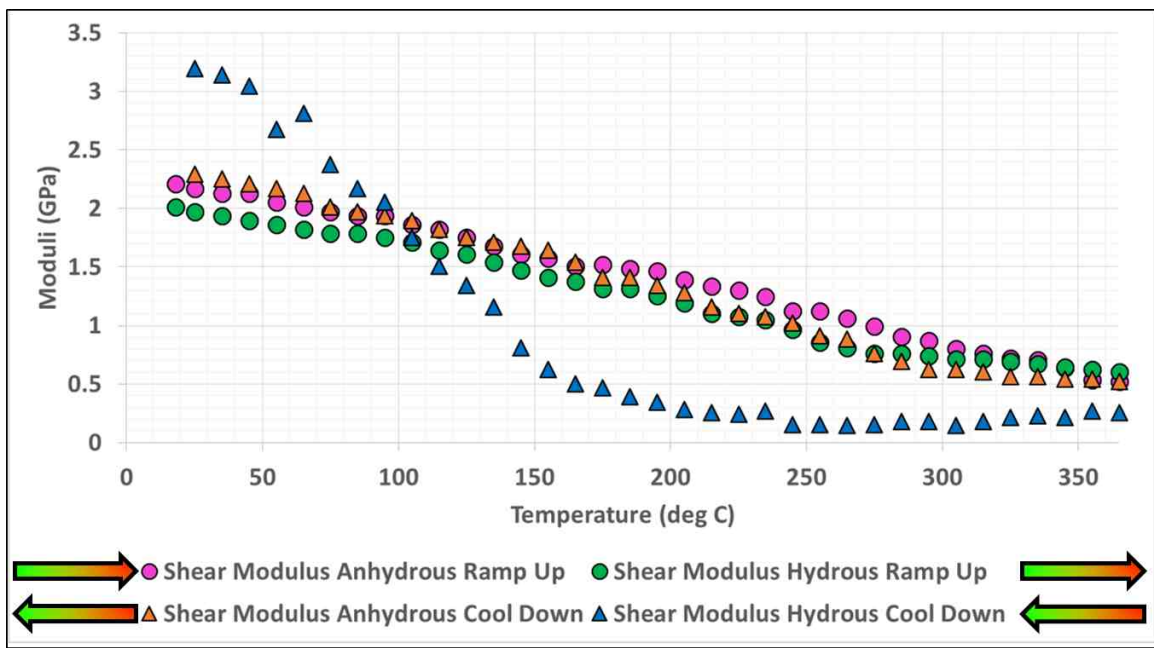


Figure 3.29: Shear modulus as a function of temperature

The shear modulus exhibited the same relative changes seen in the bulk modulus, except for the hydrous experiment. The shear modulus is a measure of shear stress to shear strain, described in section 2.5. The hydrous shear modulus on the cool down phase is much lower initially compared the anhydrous shear moduli and ramp-up portion of the hydrous shear modulus, but increases quite rapidly as temperature reaches approximately 150°C. After this temperature, the amount of shear stress to shear strain is quite a bit higher.

The vertical Poisson’s ratio in Figure 3.30 is a ratio of the axial strain to the radial strain. All samples, hydrous and anhydrous, were slightly shortened in the axial direction

and expanded in the lateral direction. For the anhydrous experiments, it is seen that overall, the Poisson's ratio increases for higher temperatures, approaching the limit of 0.5, indicating that at higher temperatures, these oil shale samples undergoing anhydrous pyrolysis become less compressible in the axial direction. This makes sense, as the radial deformation reached a limit and minimal radial expansion was observed upon completion of the experiment. This could be due to the closure of micro-fractures or pore spaces during pyrolysis, which of course would result in the sample unable to compress any more aside from the development of larger fractures.

For the hydrous pyrolysis however, the Poisson's ratio exhibited little change, and decreased slightly with increasing temperature. The brine allowed for the pore spaces to remain open longer, and in fact replace the denser kerogen material. Therefore, even though brine would be considered incompressible, it caused larger radial deformation in the oil shale sample with increase in temperature. This was observed physically in the samples on completion of hydrous pyrolysis, as they had expanded so far radially that they had deformed and taken the banded shape of the confining jacket.

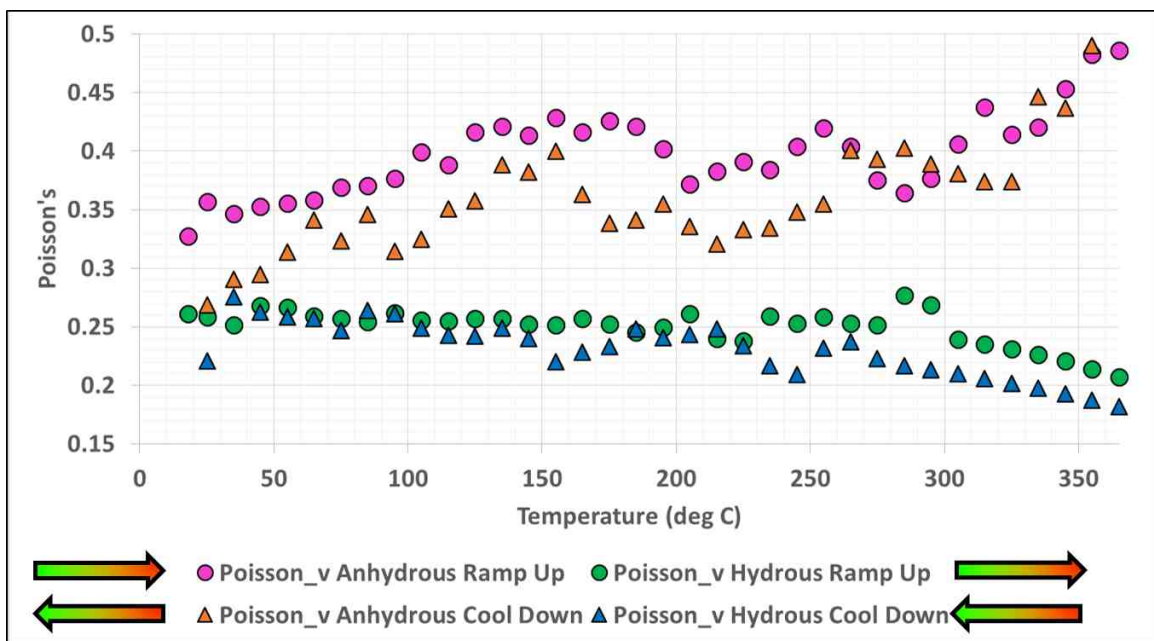


Figure 3.30: Poissons Ratio as a function of temperature

ε is the ratio of the vertical compressional waves to horizontal compressional waves (Figure 3.31). For anhydrous pyrolysis, we see a slight increase as a function of temperature, with a slight overall decrease in the cool down portion. Compared to the anhydrous pyrolysis, the hydrous pyrolysis has a much more dramatic result however, as there is a more prominent increase around 300°C, and increases in the cool down phase. There is an overall increase in this ratio for all samples, but all (except for the hydrous sample on the cool down phase) remain lower than 1, meaning the horizontal compressional wave was still faster for most of the samples compared to that of the vertical. However, in the cool down phase of the hydrous sample, we observe that ε approaches and likely goes just above one, indicating that the compressional and horizontal waves in both directions are approximately equal. This is unlikely however, as velocities in the horizontal direction (parallel to bedding) should always be faster than velocities in the vertical direction (perpendicular to bedding). This is due to the fact that parallel to bedding, the velocity is defined by the fastest layers of the sample, while perpendicular to bedding, velocities are defined by the slowest layers in the sample. It is likely that the dramatic overall increase could be due to fracture development and splitting of the layering in the horizontal direction.

Similarly, γ is a ratio of the vertical shear wave to the horizontal shear wave (Figure 3.32). A similar trend is observed, only the ratio for the hydrous pyrolysis cool down phase had a much higher peak at around 250°. This indicates that the shear wave in the vertical direction becomes much faster than the shear wave in the horizontal direction for a large portion of the cool down phase.

Finally, we observe trends in the δ plotted in Figure 3.33. Oddly, larger changes are observed in the anhydrous pyrolysis compared to the hydrous pyrolysis. Data trends seen were expected for the most part, but quantifiable trends were not known until now. These results will be correlated with other methods (SEM, CT, TOC, and SRA) to explain changes in the waveform derived data in the next chapter.

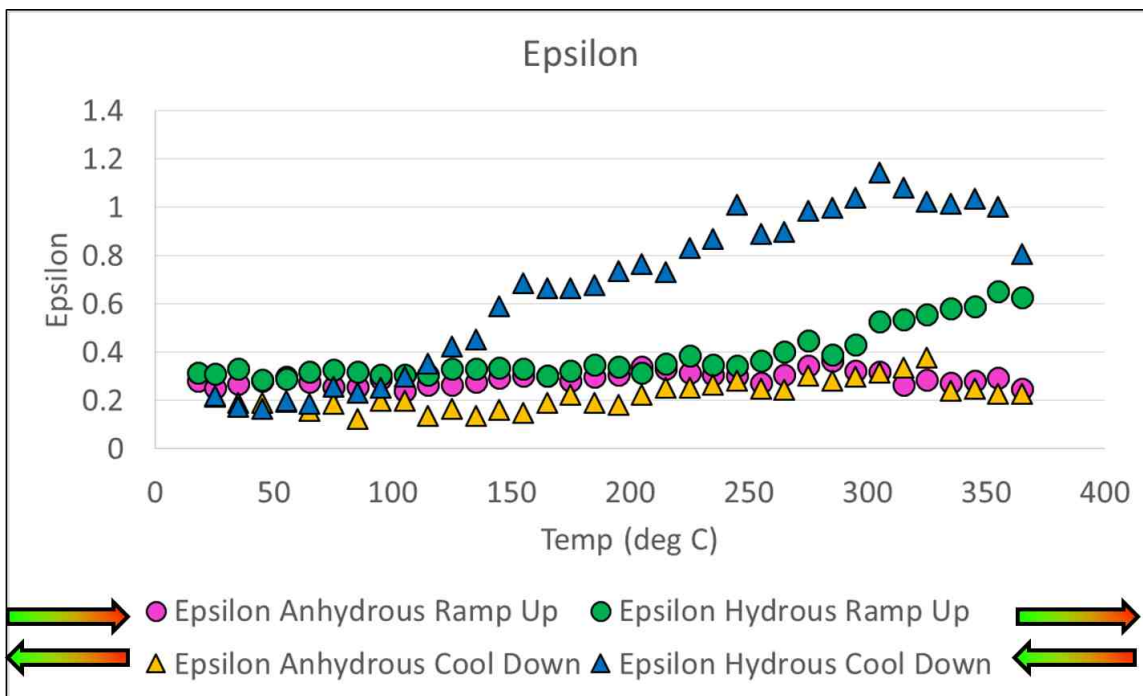


Figure 3.31: Epsilon as a function of temperature

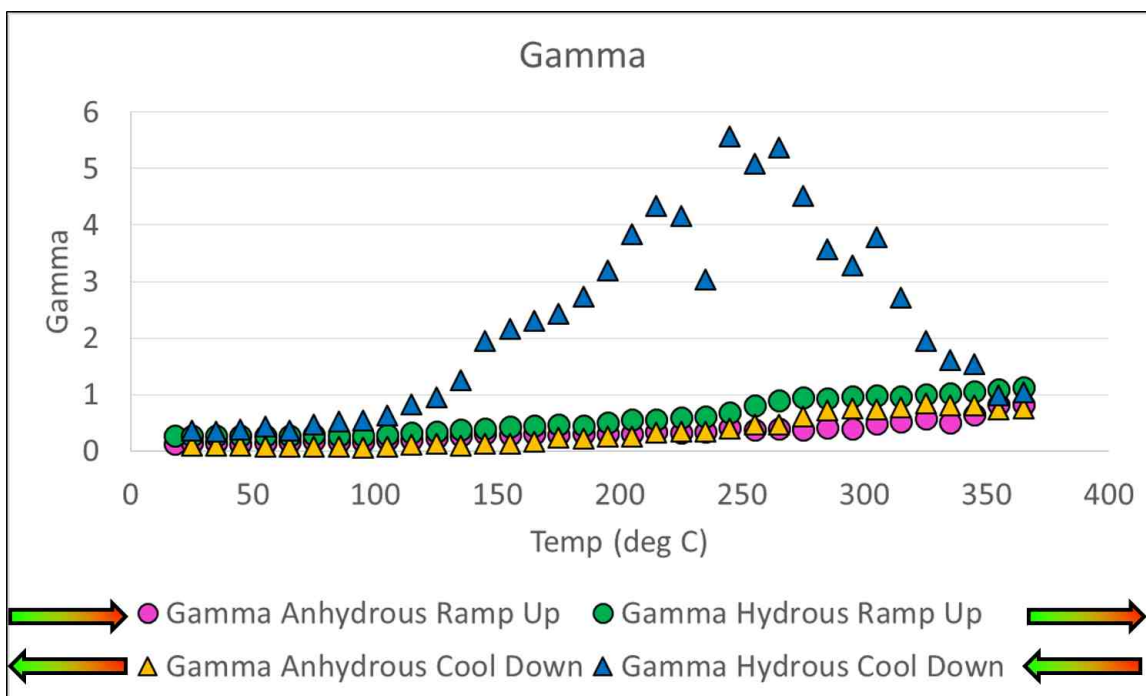


Figure 3.32: Gamma as a function of temperature

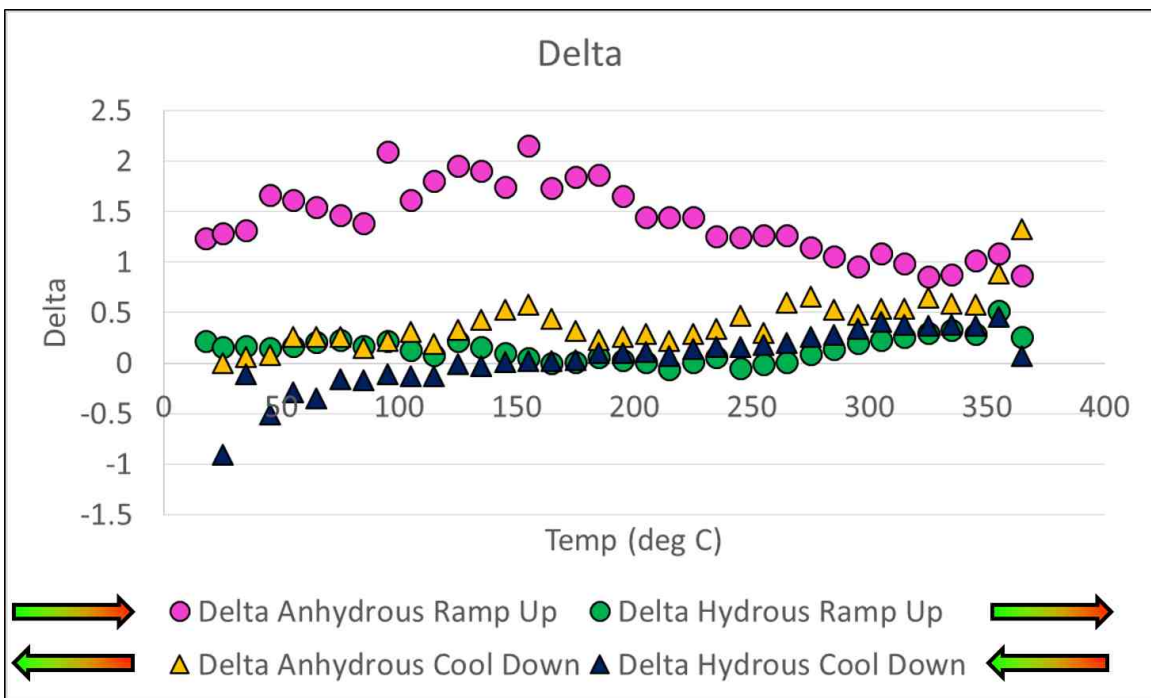


Figure 3.33: Delta as a function of temperature

CHAPTER 4

DISCUSSION

Hydrous pyrolysis reduced TOC and resulted in greater sample deformation compared to anhydrous pyrolysis. As a result of hydrous pyrolysis, TOC was reduced by 5% and samples expanded by approximately 2 mm in the radial direction. Furthermore, bitumen development was seen to be much higher in the hydrous pyrolysis samples compared to anhydrous samples. Based on these initial results, it appears that hydrous pyrolysis results in more efficient hydrocarbon generation. This chapter discusses errors in data, analyzes acoustic data with other results, and finally compares this data to previous work.

4.1 Error Analysis

It was necessary to extrapolate some velocity data to fill in data gaps at higher temperatures, especially for the hydrous pyrolysis (Figure 4.1). While the derived data was based off of observed trends, expected behaviors, and V_p - V_s ratios, it would be more appropriate to determine acoustic properties from an average of several different measurements as opposed to one. This would involve doing acoustic measurements on each bedding angle, with each bedding angle having several representative samples.

For imaging with CT, it was difficult to do comparisons before and after pyrolysis due to the uncertainty in the exact placement of the samples. This problem was prevalent in CT scans in particular when trying to ascertain the exact change in axial and radial length of samples after pyrolysis. CT measurements showed that the sample had decreased by nearly a mm during the hydrous pyrolysis, while the anhydrous pyrolysis did not show significant deformation (Figure 3.10(a)), and had to be measured manually with calipers after pyrolysis to quantify length changes. Quantitative measurements in CT scans proved that samples were cored at proper bedding orientations, but were inaccurate when quantifying the axial and radial length changes.

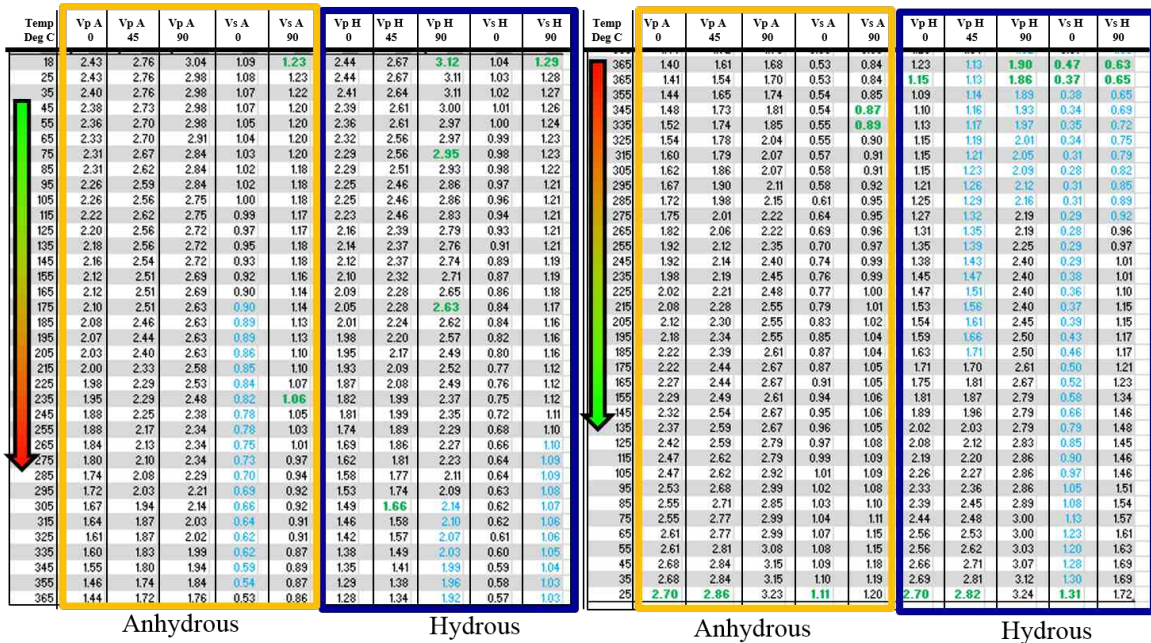


Figure 4.1: Recorded velocity data, with all derived data shown in blue. Anhydrous and hydrous ramp-up is shown in the two left columns, and the anhydrous and hydrous cool-down is shown in the two right columns after 48 hours at 365°C.

SEM images provided insight into the kerogen conversions to hydrocarbons, as well as porosity development. Images before and after pyrolysis show some differences, but more thorough analysis would involve comparing the same areas of the samples to within a few microns of resolution. An ideal SEM analysis would look something like a figure from Allan et al. [2013] shown in Figure 4.2. Kerogen cracking and micro-cracking is observed and easily comparable before and after pyrolysis.

XRD, TOC, and SRA are subject to error because data was based off of very few samples. Analysis prior to pyrolysis was based off of three samples. Due to analysis in CT and SEM, it was not possible to submit all samples to TOC and SRA analysis. As with velocity data, it would be more useful to determine this data from an average of samples.

Velocities were picked based on an average of the fastest possible and slowest possible first arrival times, with maximum error of $\pm 10\%$ in the velocities. Velocity errors were more prevalent in the shear waveforms due to the interference of converted compressional waves.

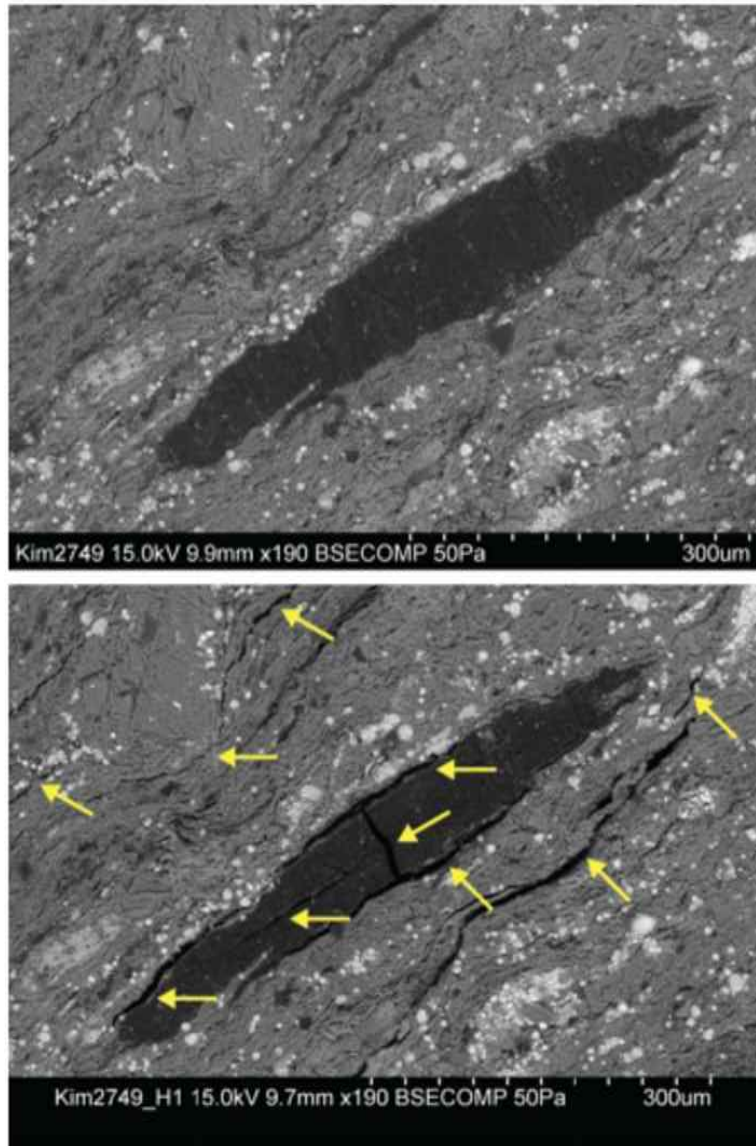


Figure 4.2: BSE-SEM images of kerogen maturation before pyrolysis (top) and after (bottom), from Allan et al. [2013].

As mentioned earlier, some data were extrapolated at higher temperatures, especially for the cool down portion of the hydrous experiments. This is where more data from additional samples would help to either retrieve these missing data points, or at least add confidence to extrapolated values.

4.2 Data Analysis

Data from Chapter 3 explains the changes in velocities seen during the high-temperature, high-pressure experiment. There were no significant differences in the compressional or shear velocities between the ramp-up and cool-down portions of anhydrous pyrolysis, but there were significant differences in the ramp-up and cool-down portions of the hydrous pyrolysis. A summary of observed changes and some causes are shown in Figure 4.3.

In Figure 4.4, CT scans of 0° and 90° samples are compared with compressional velocities of hydrous ramp-up and cool-down. On the cool-down portion, the V_{p45} velocities lie over the V_{p0} velocities, and both sets of velocities have decreased significantly in the 365°C to 100°C of the cool-down compared to the ramp-up portion. This velocity decrease is associated with fracture development during pyrolysis. When the rock cracked, at higher temperatures, the cracks remained slightly open, significantly reducing the velocities. The 90° sample did not have a large fracture along the bedding plane, but did have several small ones. V_{p90} on the cool-down portion showed no significant increase or decrease compared to the ramp-up portion. The shear velocities also decreased for most of the cool-down phase of the hydrous pyrolysis (Figure 4.5). A larger increase in V_s velocities is observed on the cool-down portion of hydrous pyrolysis, which can be explained by closure of small cracks along the bedding plane and a decrease in organic content.

SEM images show additional evidence of hydrocarbon generation and micro-fracture development, which explains the lower velocities on the cool-down portion of the hydrous pyrolysis. New fracture porosity was generated due to higher temperatures and kerogen-to-bitumen conversions (Figure 4.6). Organic matter converting to bitumen and hydrocarbons in existing pore space, as well as open fractures, and the brine used in the hydrous pyrolysis





Velocity (km/s)	Ramp-up 	Cool-down 	Ramp-up 	Cool-down 
Vp 0	Approx. 1.2 km/s slower at 365°C compared to 25°C starting temperature. No kerogen-bitumen conversion	Approx. 1.5 km/s slower at 365°C compared to 25°C end temperature. Minimal kerogen-bitumen conversion	Consistent decrease, slight concavity downwards. Approx. 1.2 km/s slower at 365°C compared to 25°C starting temperature.	Increase at faster rate, concavity upwards. Approx. 1.5 km/s slower at 365°C compared to 25°C end temperature. Significant kerogen to bitumen conversion,
Vp 45	Approx. 1.0 km/s slower at 365°C compared to 25°C starting temperature.	Approx. 1.3 km/s slower at 365°C compared to 25°C end temperature.	Consistent decrease, slight concavity downwards. Approx. 1.25 km/s slower at 365°C compared to 25°C starting temperature.	Approx. 1.6 km/s slower at 365°C compared to 25°C end temperature. Concave up appearance in curve. Similar to Vp 0 due to cracking in bedding plane. Significant kerogen to bitumen conversion
Vp 90	Approx. 1.0 km/s slower at 365°C compared to 25°C starting temperature.	Approx. 1.5 km/s slower at 365°C compared to 25°C end temperature.	Approx. 1.35 km/s slower at 365°C compared to 25°C starting temperature.	Approx. 1.55 km/s slower at 365°C compared to 25°C end temperature.
Vs 0	Approx. 0.35 km/s slower at 365°C compared to 25°C starting temperature	Approx. 0.35 km/s slower at 365°C compared to 25°C end temperature. Lower increase up until 260°C, followed by slightly more rapid increase.	Approx. 0.4 km/s slower at 365°C compared to 25°C starting temperature. Shallow slope at 260°C in velocity decrease.	Approx. 1.1 km/s slower at 365°C compared to 25°C end temperature. Constant velocity to 240°C, followed by rapid increase Velocities higher at end cool-down temperature compared to start of hydrous ramp-up
Vs 90	Consistent decrease. Approx. 0.55 km/s slower at 365°C compared to 25°C starting temperature	Some concavity upwards. Approx. 0.55 km/s slower at 365°C compared to 25°C end temperature.	Approx. 0.25 km/s slower at 365°C compared to 25°C start temperature.	Approx. 0.9 km/s slower at 365°C compared to 25°C end temperature. Velocities higher at end cool-down compared to start of hydrous ramp-up

Figure 4.3: Summary of velocity changes observed in the ramp-up and cool-down portions of anhydrous and hydrous pyrolysis.

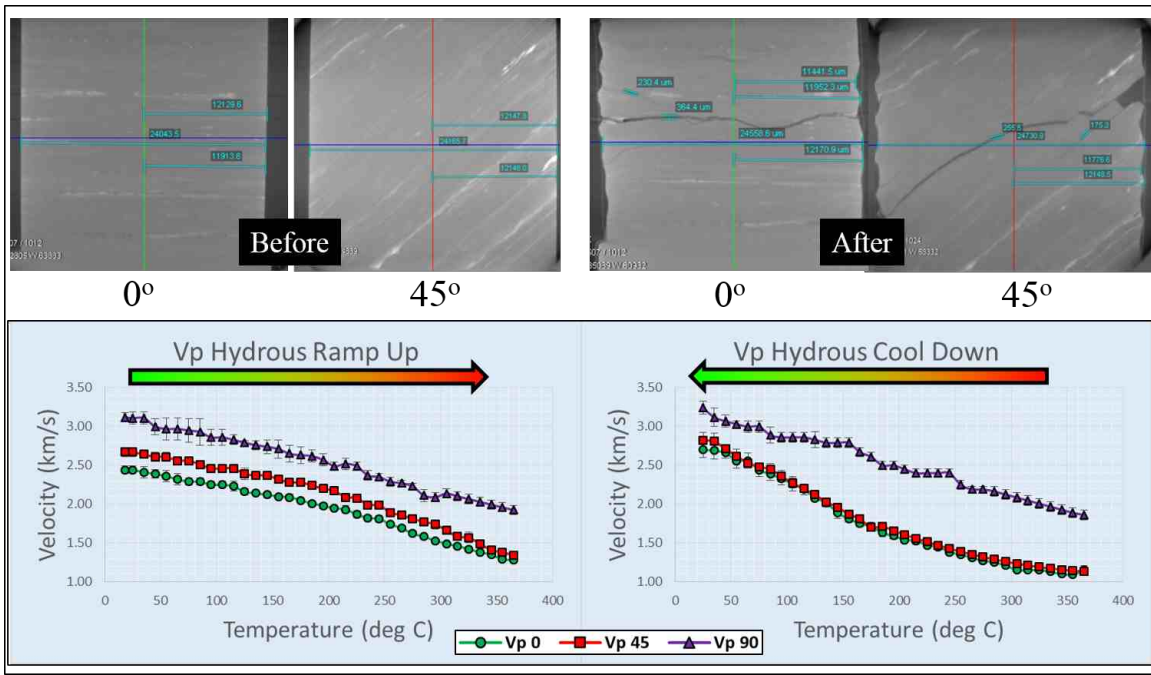


Figure 4.4: Comparison of before and after hydrous pyrolysis CT scans with hydrous compressional velocity measurements. CT scans are from Figure 3.8(b) and Figure 3.9(b) in section 3.3, and velocity plots as a function of temperature are from Figure 3.25 in section 3.5.

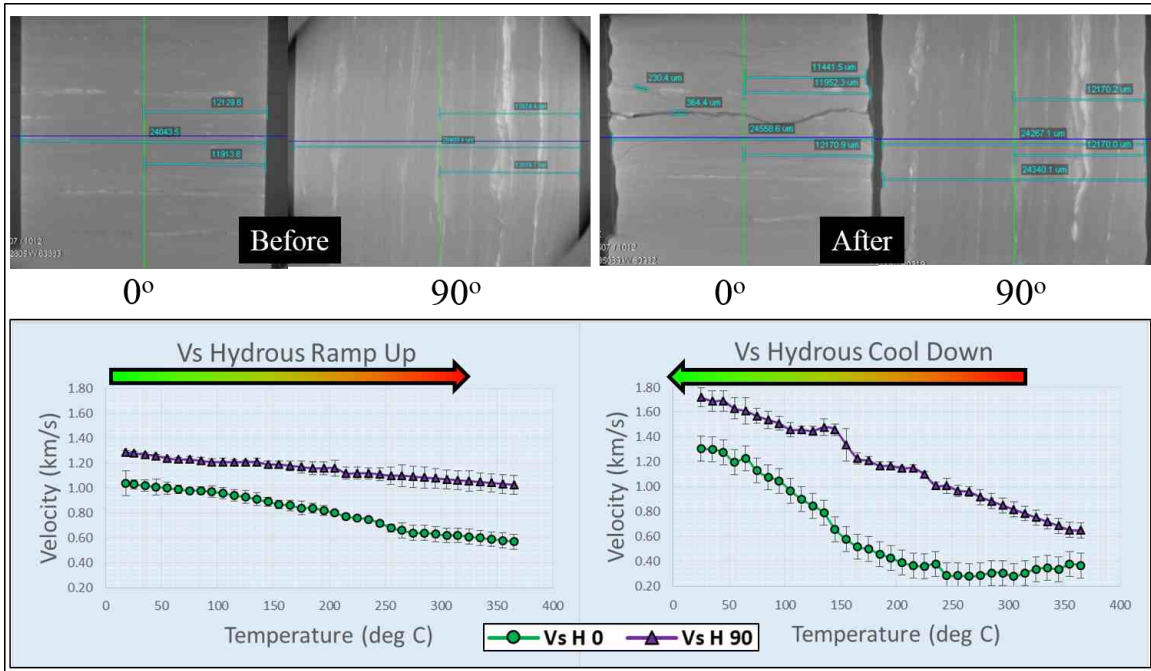


Figure 4.5: Comparison of before and after hydrous pyrolysis CT scans with hydrous shear velocity measurements. CT scans are from Figure 3.8(b) and Figure 3.10(b) in section 3.3, and velocity plots as a function of temperature are from Figure 3.27 in section 3.5.

all contribute to lower velocities, especially after 48 hours at 365°C.

The shear modulus also has results that correlate to data seen in the CT scans (Figure 4.7). The shear modulus is directly derived from the C_{44} stiffness coefficient, which is calculated from the product of the density and square of the shear velocity in the 0° direction. Assuming the density remains constant, then the driving mechanism for the shear modulus change is the change in the shear velocity. Large cracks and deformation account for a significant portion of the overall decrease in the shear modulus at higher temperatures, but the cool-down portion of the hydrous pyrolysis shows a drastic increase at much lower temperatures (<150°C). However, but there is a slight increase in velocities at temperatures above 250°. This could be due to the brine vaporizing at those temperatures.

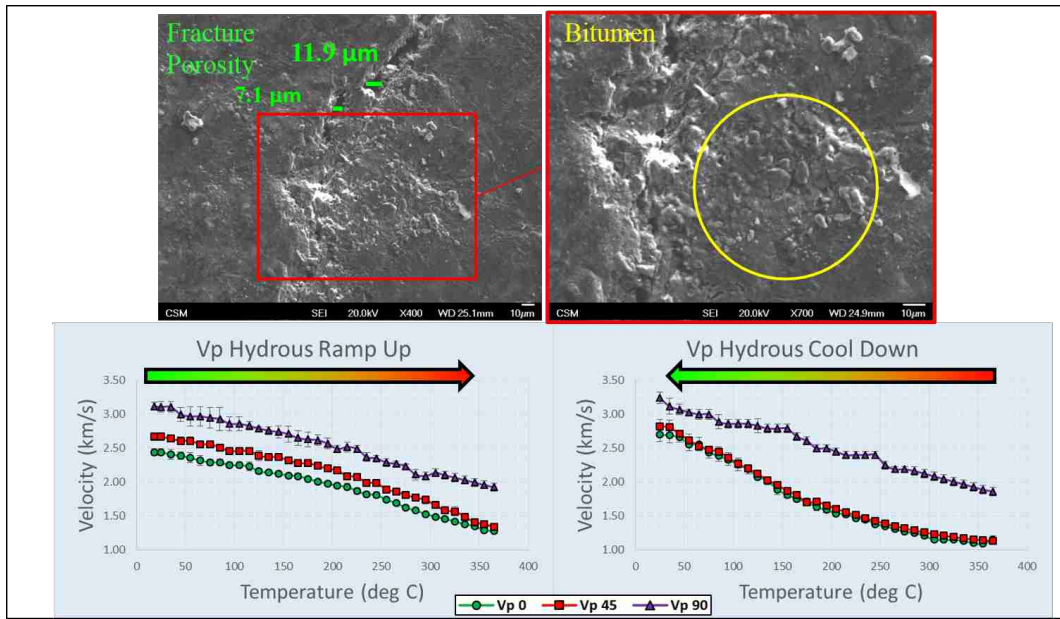


Figure 4.6: Comparison of before and after hydrous pyrolysis SEM with hydrous compressional velocity measurements. SEM images are from Figure 3.22 in section 3.4, and velocity plots as a function of temperature are from Figure 3.27 in section 3.5.

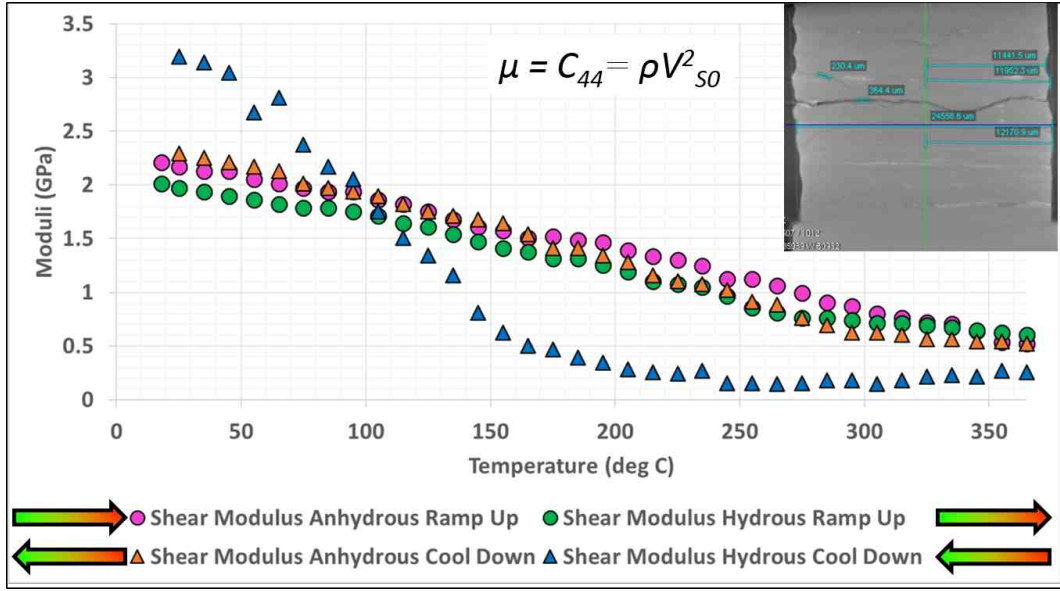


Figure 4.7: Shear modulus shown with 0° oriented hydrous sample CT scan. Shear modulus figure from Figure 3.29 in section 3.5.

4.3 Data Comparison

Velocities are overall lower on the cool-down portion of the hydrous pyrolysis compared with anhydrous pyrolysis, but velocities also increase significantly past 100°C on the cool-down portion (Figure 4.8). Some of this can be explained using a relationship from Mraz et al. [1983], shown in Figure 4.9, where the velocity increases in a rock as organic content decreases. Section 3.1 revealed that after hydrous pyrolysis, the TOC had decreased by approximately 5%. Acquiring additional velocity data from Irati Formation samples of varying TOC before and after pyrolysis would be useful to compliment this data set, as there opposing forces during the high-temperature, high-pressure experiment that affect the velocities: 1) Increasing velocities due to a decrease of organic content and bitumen reaching a glass point (hardening) on the cool-down portion and 2) Decreasing velocities due to increase of heat and fracture generation decreasing velocities. The decrease in organic content, as well as the closing of some fractures under the 800 psi effective pressure and lower temperatures at the end of the cool-down portion would contribute to overall higher velocities towards the end of the high-temperature, high-pressure experiment.

Previous work to evaluate stiffness coefficients and the γ Thomsen parameter is shown in Figure 4.10. Data from Behura et al. [2009] was recorded under unconfined conditions and velocities obtained at a frequency of 3 MHz. Data from Elbaharia [2012] plots the same information, but with an axial confined pressure at approximately 2000 psi. Note that under the VTI assumption, $C_{44} = C_{55}$.

The effects of pyrolysis on the stiffness coefficients C_{44} and C_{66} to γ are presented in Figure 4.10. Data from the cool-down portion of the hydrous pyrolysis (Figure 4.10(b)) in this study is similar to the responses in the stiffness coefficients and gamma Thomsen parameter in previous works from Behura et al. [2009] (Figure 4.10(c)) and Elbaharia [2012] (Figure 4.10(d)). The lack of a similar response in the ramp-up portion of the hydrous pyrolysis (Figure 4.10(a)) could be due to a slightly faster ramp-up time in this study. Overall, these plots show that as temperature increases, shear waves exhibit greater changes due to

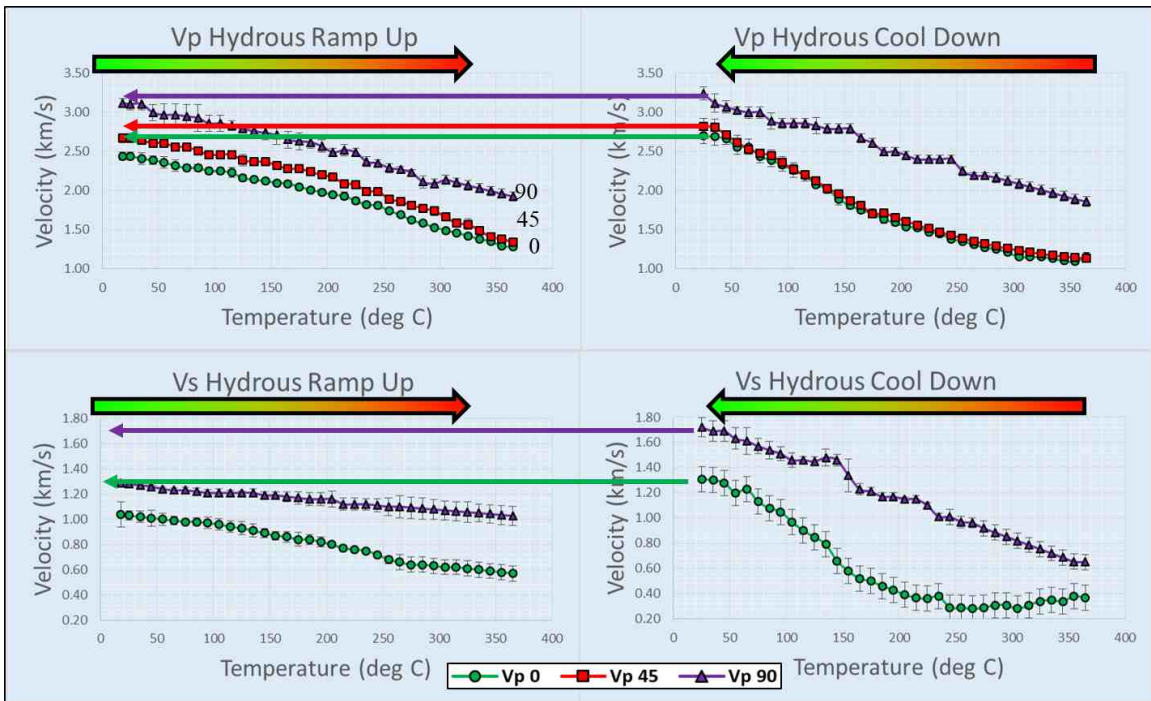


Figure 4.8: Increase in velocities at lower temperatures after hydrous pyrolysis. Arrows indicate the differences between the velocities at the starting temperature and the velocities at the end of the cool-down portion of the experiment, which are consistently higher. Vp and Vs are from Figure 3.25 and Figure 3.27 in section 3.5.

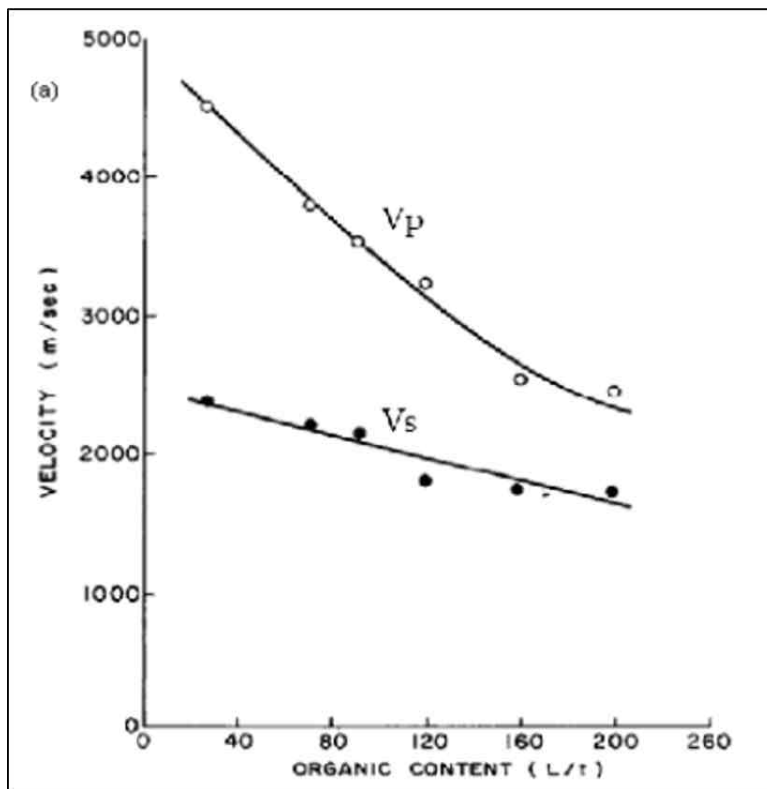
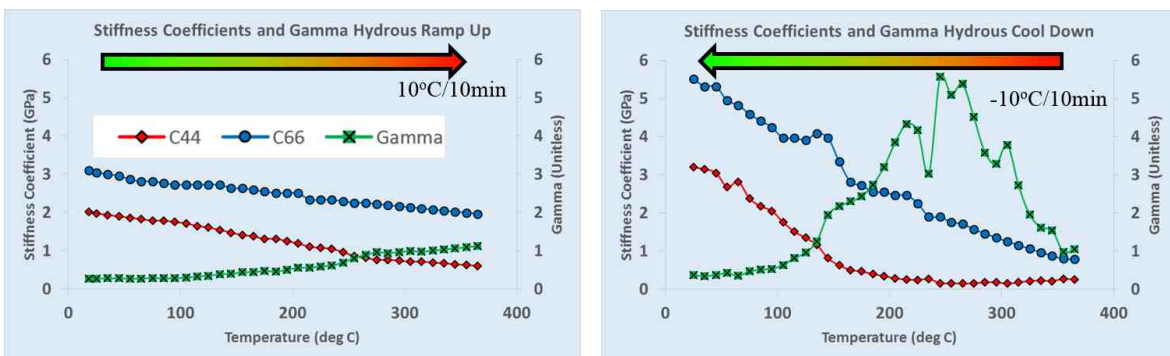
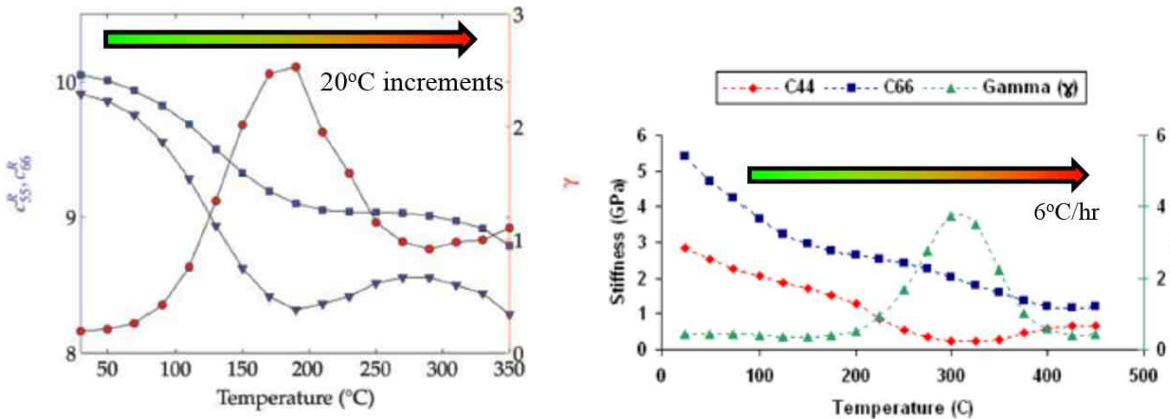


Figure 4.9: Relationship between organic content and velocities, after Mraz et al. [1983].

bitumen and hydrocarbon generation. As temperature increases and fluids are expelled, the change in the shear modulus in the vertical and horizontal directions both approach zero. The lack of an obvious peak in the anhydrous experiment and the ramp-up portion of the hydrous experiment could be attributed to either velocity picking errors and/or too rapid of a temperature increase for hydrocarbon generation. This could explain the very different responses in the hydrous pyrolysis after the 48 hold period at 365°C between the ramp-up and cool-down portions of the hydrous pyrolysis.



(a) C_{44} , C_{66} , and γ from CSM hydrous ramp-up (b) C_{44} , C_{66} , and γ from CSM hydrous cool-down



(c) C_{55} , C_{66} , and γ from Behura et al. [2009] (d) C_{44} , C_{66} , and γ from Elbaharia [2012]

Figure 4.10: Stiffness coefficients C_{44} and C_{66} compared to Gamma (γ) from previous works . From this study, stiffness coefficients and γ from hydrous ramp up (a) and hydrous cool-down (b). From other studies, a 20° incremental temperature ramp-up from Behura et al. [2009] ($C_{44} = C_{44}$) (c), and an incremental temperature ramp-up of 6°C per hour from Elbaharia [2012] (d).

CHAPTER 5

CONCLUSIONS AND RECOMMENDATIONS

Experiments have been performed to characterize oil shale from of the Irati Formation from the state of Paraná, Brazil. Samples were analyzed from Block 003 under as-received conditions. Analysis prior to pyrolysis included XRD mineral identification, TOC and SRA for maturity determination, and SEM and CT scans for imaging of layering, small and large-scale fracturing, and porosity development. High temperature and pressure experiments were carried out to induce artificial maturation within samples, while simultaneously acquiring velocity information to derive elastic moduli and Thomsen parameters. This velocity data was acquired and analyzed for anhydrous and hydrous pyrolysis conditions during both ramp-up and cool-down portions of the experiment. All analysis methods prior to pyrolysis were again performed post-pyrolysis.

5.1 Conclusions

This work resulted in a unique set of acoustic data from the hydrous and anhydrous pyrolysis of Irati oil shale of approximately 25% TOC. The high-temperature, high-pressure experiment has been streamlined, with a more automated temperature controller and data acquisition process. Furthermore, it has been successfully tested to do long term experiments, from several hours to several days. Finally, a manual for the high-temperature, high-pressure experiment at CSM has been written as part of the requirements for this thesis work.

An alternative coupling material that could withstand high temperature was used, as well as the introduction of water into the system to create hydrous pyrolysis conditions. Previous experiments by Elbaharia [2012] used gold foil, which provided consistent coupling, but was costly and unreliable for the high amount of experiments necessary for this work. The copper calibration experiment proved that Krytox couplant was sufficient to measure properties of samples. However, coupling issues arose from the deformation of samples, especially that

of hydrous samples, as evident by lower signal quality and amplitude in all of the hydrous experiments compared to the anhydrous.

Results showed that by implementing a hydrous pyrolysis to oil shale from the Irati formation samples, more kerogen-to-bitumen and bitumen-to-hydrocarbon conversions took place compared to only anhydrous pyrolysis at the temperatures and heating rates used in this study. After hydrous pyrolysis, TOC had decreased from 25 wt% to 20 wt%. Anhydrous pyrolysis is still effective at slower rates and temperatures above 365°, but proved less effective based on the lack of change in TOC and in acoustic data. In the hydrous pyrolysis, the velocities at the start temperature of the ramp-up portion were consistently lower than the same velocities at the end temperature of the cool-down portion. There were little differences in velocities in the anhydrous pyrolysis between the start temperature and end temperature, but the compressional velocities of the hydrous pyrolysis were 10-15% higher and the shear velocities were up to 30% higher at the end of the experiment compared to the beginning. These large increases are due to the kerogen-to-bitumen conversion, where at lower temperatures on the cool-down portion, the bitumen becomes solid, reaching a glass point.

Although current oil shale production in Brazil is performed using mainly surface mining, seismic anisotropy parameters are important for future seismic acquisition for in-situ production. Recording these parameters on other samples from different areas of the Irati formation during pyrolysis will also allow for better characterization of time-lapse seismic that might be acquired. Comparing these parameters with changes in TOC and SRA will help determine if maximum efficiency is achieved during production, either with surface mining and retorting or in-situ production. The high-temperature, high-pressure experiment is a useful process for testing the artificial maturation of oil shale, and the results from this study have shown that hydrous pyrolysis has potential to increase the economic value of oil shale.

5.2 Future Work

It is recommended that more samples be analyzed to have better averaged mineralogy, clay content, and TOC and SRA values. The samples in this study were limited to the provided sample materials. For large scale development of oil shale deposits, much more sampling would be needed to accurately characterize the deposits. It is also recommended that a few samples be used to derive better averaged acoustic measurements.

It would be beneficial to perform these experiments over a longer time period. Some work currently under way involves heating samples to approximately 100°C for 30 days to compare with the samples heated to 100°C temperature in this study. Naturally matured conventional oil reservoirs occur over much longer time periods (millions of years), and at relatively lower temperatures compared to that of production through pyrolysis. Diagenesis occurs near 50°C, catagenesis between 50°C and 150°C, and metagenesis at 150°C to 200°C [McCarthy et al., 2011]. While more extreme temperatures over shorter time periods do convert kerogen to bitumen and hydrocarbons, the organic matter is at risk of becoming over-mature, and therefore does not maximize efficiency during production.

A major challenge of this work is the time consuming nature of which it takes to prepare samples, run the experiments, and analyze the results. It would be beneficial if the confining jacket assembly and transducers could be designed such that they were re-usable. Instead of having to tear apart the confining jacket, it would be useful to have a design in which a sample could more easily be ‘popped’ in and out of the assembly. This would be useful both to save time on sample preparation, but also to have a more consistent seal on the sample to separate pore and confining pressures.

Sample results in this study were compared in terms of anhydrous and hydrous pyrolysis. It would be useful to complement this data set with samples cored at 0° to the symmetry axis sample P and S wave analysis for dry and saturated conditions. To achieve ‘dry’ conditions, samples would be heated to 55°C until mass loss stabilizes (after Allan et al. [2013]). To achieve saturated conditions, it is necessary to place samples in a transfer vessel, and

pressurize with fluids for a few weeks to a couple months. This is also challenging, as samples can fracture as a result of clay swelling and applied pressure.

A summary of suggested projects to compliment this data set and others is given below:

- Determine effects of TOC on maturation (hydrous and anhydrous)
- Perform similar experiments under dry and saturated conditions
- Incorporate higher pressures, and responses as a function of pressure

REFERENCES CITED

- Adam M. Allan, Tiziana Vanorio, and Jeremy E. P. Dahl. Thermal maturation-induced variation of P-wave anisotropy of organic-rich shale. In *SEG Technical Program Expanded Abstracts 2013*, pages 2767–2772. Society of Exploration Geophysicists, September 2013. doi: 10.1190/segam2013-0064.1. URL <http://library.seg.org/doi/abs/10.1190/segam2013-0064.1>.
- Jyoti Behura, Mike Batzle, Ronny Hofmann, and John Dorgan. The shear properties of oil shales. *The Leading Edge*, 28(7):850–855, July 2009. ISSN 1070-485X. doi: 10.1190/1.3167788. URL <http://www.mendeley.com/research/shear-properties-oil-shales-2/>.
- Jeremy Boak. CO₂ Release from In-Situ Production of Shale Oil from the Green River Formation in the Western United States. In *27th Oil Shale Symposium*, pages 1–12, Gold, 2007.
- R.F. Cane. The Origin and Formation of Oil Shale. In Teh Fu Yen and George V. Chilingarian, editors, *Developments in Petroleum Science, 5. Oil Shale*, volume 5 of *Developments in Petroleum Science*, chapter 3, pages 28–60. Elsevier, 1976. ISBN 9780444414083. doi: 10.1016/S0376-7361(08)70043-8.
- Zuleika Carreta Correa Da Silva and Chris Cornford. The kerogen type, depositional environment and maturity, of the Irati Shale, Upper Permian of Paraná Basin, Southern Brazil, January 1985. ISSN 01466380. URL <http://linkinghub.elsevier.com/retrieve/pii/S014663808590018X>.
- John R. Dyni. Geology and Resources of Some World Oil-Shale Deposits: U.S. Geological Survey Scientific Investigations Report 2005-5294. Technical report, U.S. Geological Survey, Reston, Virginia, 2006.
- Mohammad Elbaharia. *High Temperature Characterization of Oil Shales: The Green River Formation*. PhD thesis, Colorado School of Mines, 2012.
- Casimiro Silva Filho, Marcelino Kaizer, Luis Fernando Sosinski, and PETROBRAS SA Skalski, Julio. Environmental and Operational Aspects of an Oil Shale Industrial Plant in Brazil. In *28th Oil Shale Symposium*, Golden, Colorado, 2008.

- Mariano N. Garcia, Federico Sorenson, Juan Carlos Bonapace, Fabio Motta, Christian Bajuk, and Hernan Stockman. Vaca Muerta Shale Reservoir Characterization and Description: The Starting Point for Development of a Shale Play with Very Good Possibilities for a Successful Project. *Unconventional Resources Technology Conference, Denver, Colorado, 12-14 August 2013*, pages 863–899, August 2013. doi: 10.1190/urtec2013-090. URL <http://library.seg.org/doi/abs/10.1190/urtec2013-090>.
- Thomas Hantschel and Armin I. Kauerauf. *Fundamentals of Basin and Petroleum Systems Modeling*. Springer Science & Business Media, 2009. ISBN 3540723188. URL <https://books.google.com/books?id=-vhmCHTZbdwC&pgis=1>.
- B. S. Hart and A. S. Steen. Programmed pyrolysis (Rock-Eval) data and shale paleoenvironmental analyses: A review. *Interpretation*, 3(1):SH41–SH58, January 2015. ISSN 2324-8858. doi: 10.1190/INT-2014-0168.1. URL <http://library.seg.org/doi/abs/10.1190/INT-2014-0168.1>.
- Hollis D Hedberg. Geologic Aspects of Origin of Petroleum. *AAPG Bulletin*, 48, 1964. ISSN 0149-1423. doi: 10.1306/BC743DB7-16BE-11D7-8645000102C1865D. URL <http://search.datapages.com/data/doi/10.1306/BC743DB7-16BE-11D7-8645000102C1865D>.
- B. Lavina, P. Dera, and R. T. Downs. Modern X-ray Diffraction Methods in Mineralogy and Geosciences. *Reviews in Mineralogy and Geochemistry*, 78(1):1–31, February 2014. ISSN 1529-6466. doi: 10.2138/rmg.2014.78.1. URL <http://ring.geoscienceworld.org/content/78/1/1>.
- Michael D. Lewan and Stéphanie Roy. Role of water in hydrocarbon generation from Type-I kerogen in Mahogany oil shale of the Green River Formation. *Organic Geochemistry*, 42(1):31–41, January 2011. ISSN 01466380. doi: 10.1016/j.orggeochem.2010.10.004. URL <http://linkinghub.elsevier.com/retrieve/pii/S014663801000255X>.
- Michael D Lewan, Justin E Birdwell, and U S Geological Survey. Application of Uniaxial Confining-core Clamp with Hydrous Pyrolysis in Petrophysical and Geochemical Studies of Source Rocks at Various Thermal Maturities. i:2565–2572, 2013. doi: 10.1190/urtec2013-267.
- Kevin McCarthy, Katherine Rojas, Martin Niemann, Daniel Palmowski, Kenneth Peters, and Artur Stankiewicz. Basic Petroleum Geochemistry for Source Rock Evaluation. *Oilfield Review*, 23(2):32–43, 2011. ISSN 09231730. URL http://www.slb.com/~media/Files/resources/oilfield_review/ors11/sum11/basic_petroleum.pdf.
- Thomas Mraz, Joel DuBow, and Krishnan Rajeshwar. Acoustic wave propagation in oil shale. *Fuel*, 62(10):1215–1222, October 1983. ISSN 00162361. doi: 10.1016/0016-2361(83)90066-2. URL <http://www.sciencedirect.com/science/article/pii/0016236183900662>.

- Perry Nowacki. *Oil shale technical data handbook*. Noyes Data Corp., 1981. ISBN 0815508352.
- Jialin Qian and Jianqiu Wang. World oil shale retorting technologies. *Combustion*, (November):7–9, 2006.
- Leon Thomsen. Weak elastic anisotropy. *GEOPHYSICS*, 51(OCTOBER):1954–1966, 1986.
- Ilya Tsvankin. Anisotropic parameters and P wave velocity for orthorhombic media. *GEOPHYSICS*, 62(4):1292–1309, July 1997. ISSN 0016-8033. doi: 10.1190/1.1444231. URL <http://library.seg.org/doi/abs/10.1190/1.1444231>.
- Zhijing Wang. Seismic anisotropy in sedimentary rocks, part 1: A single plug laboratory method. *Geophysics*, 67(5):1415–1422, September 2002. ISSN 0016-8033. doi: 10.1190/1.1512787. URL <http://library.seg.org/doi/abs/10.1190/1.1512787>.
- Fuyong Yan, De-hua Han, and Qiuliang Yao. Physical constraints on c_{13} and Thomsen parameter δ for VTI rocks. In *SEG Technical Program Expanded Abstracts 2013*, volume 2, pages 2889–2894. Society of Exploration Geophysicists, September 2013. doi: 10.1190/segam2013-0424.1. URL <http://library.seg.org/doi/abs/10.1190/segam2013-0424.1>.
- T.F. Yen. *Science and Technology of Oil Shale*. Ann Arbor Science Publishers, Inc., 1976. ISBN 0-250-40242-4.
- Malleswara Rao Yenugu. *Elastic, Microstructural, and Geochemical Characterization of Kerogen Maturity for Shales*. PhD thesis, University of Houston, 2014.
- Pedro Victor Zalán, Sven Wolff, and Marco Antonio M Astolfi. The Parana Basin , Brazil. In M.W. LEIGHTON, D.R. KOLATA, D.F. OLTZ, and J.J. EIDEL, editors, *Interior Cratonic Basins*, chapter 33, pages 681–708. ISBN 978-1-58861-432-2.

APPENDIX A - EQUIPMENT SPECIFICATIONS

Information here is not necessary for the overall data interpretation, but is relevant for exact data parameters used in this study to repeat experiments using the same parameters. This involves what settings were used on equipment for XRD, CT, and SEM, as well as equipment specifications. Finally, tables with picked velocities from the high temperature, high pressure experiment are provided to allow for additional derivations if necessary.

A.1 X-Ray diffraction

Equipment for the bulk mineralogy determination included a Bruker AXS D4 Endeavor X-ray diffractometer. Standard scanning parameters for bulk were used: A divergence slit and antiscatter slit of 0.3° , and was scanned at successive angles, starting at 5 degrees, and then changing every 1.05 seconds by 0.02° up to 70 degree 2 theta, for a total of about 3500 steps. A different set of standard parameters were used for clay x-ray diffraction: A divergence slit and antiscatter slit of 0.3° , and was scanned at successive angles, starting at 2 degrees, and then changing every 0.5 seconds by 0.025° up to 30 degree 2 theta, for a total of about 1100 steps.

A.2 Micro CT

The micro computer tomography scanner used was an XRadia MicroXCT 400. Magnification was set at 0.5x. Samples are rotated to have a total of 1800 tomographic images made, with an exposure time of approximately 3-4 seconds per image. The entire process takes approximately three to four hours.

A.3 SEM

The FESEM used was a JEOL 7000 FE-SEM. All measurements were taken under high vacuum conditions (less than 2.8×10^{-4} Pa).

APPENDIX B - VELOCITY DATA

All velocities presented here are the final velocities used for interpretation and plots shown in section 3.5.

Table B.1 shows velocity data during the ramp up portion of the anhydrous pyrolysis experiments.

Table B.2 shows velocity data during the cool down portion of the anhydrous pyrolysis experiments.

Table B.3 shows velocity data during the cool down portion of the anhydrous pyrolysis experiments.

Table B.4 shows velocity data during the cool down portion of the hydrous pyrolysis experiments.

Table B.1: Anhydrous Ramp Up

Temp	Vp 0	Vp 45	Vp 90	Vs 0	Vs 90
18	2.43	2.76	3.04	1.09	1.23
25	2.43	2.76	2.98	1.08	1.23
35	2.40	2.76	2.98	1.07	1.22
45	2.38	2.73	2.98	1.07	1.20
55	2.36	2.70	2.98	1.05	1.20
65	2.33	2.70	2.91	1.04	1.20
75	2.31	2.67	2.84	1.03	1.20
85	2.31	2.62	2.84	1.02	1.18
95	2.26	2.59	2.84	1.02	1.18
105	2.26	2.56	2.75	1.00	1.18
115	2.22	2.62	2.75	0.99	1.17
125	2.20	2.56	2.72	0.97	1.17
135	2.18	2.56	2.72	0.95	1.18
145	2.16	2.54	2.72	0.93	1.18
155	2.12	2.51	2.69	0.92	1.16
165	2.12	2.51	2.69	0.90	1.14
175	2.10	2.51	2.63	0.90	1.14
185	2.08	2.46	2.63	0.89	1.13
195	2.07	2.44	2.63	0.89	1.13
205	2.03	2.40	2.63	0.86	1.10
215	2.00	2.33	2.58	0.85	1.10
225	1.98	2.29	2.53	0.84	1.07
235	1.95	2.29	2.48	0.82	1.06
245	1.88	2.25	2.38	0.78	1.05
255	1.88	2.17	2.34	0.78	1.03
265	1.84	2.13	2.34	0.75	1.01
275	1.80	2.10	2.34	0.73	0.97
285	1.74	2.08	2.29	0.70	0.94
295	1.72	2.03	2.21	0.69	0.92
305	1.67	1.94	2.14	0.66	0.92
315	1.64	1.87	2.03	0.64	0.91
325	1.61	1.87	2.02	0.62	0.91
335	1.60	1.83	1.99	0.62	0.87
345	1.55	1.80	1.94	0.59	0.89
355	1.46	1.74	1.84	0.54	0.87
365	1.44	1.72	1.76	0.53	0.86

Table B.2: Anhydrous Cool Down

Temp	Vp 0	Vp 45	Vp 90	Vs 0	Vs 90
365	1.41	1.54	1.70	0.53	0.84
355	1.44	1.65	1.74	0.54	0.85
345	1.48	1.73	1.81	0.54	0.87
335	1.52	1.74	1.85	0.55	0.89
325	1.54	1.78	2.04	0.55	0.90
315	1.60	1.79	2.07	0.57	0.91
305	1.62	1.86	2.07	0.58	0.91
295	1.67	1.90	2.11	0.58	0.92
285	1.72	1.98	2.15	0.61	0.95
275	1.75	2.01	2.22	0.64	0.95
265	1.82	2.06	2.22	0.69	0.96
255	1.92	2.12	2.35	0.70	0.97
245	1.92	2.14	2.40	0.74	0.99
235	1.98	2.19	2.45	0.76	0.99
225	2.02	2.21	2.48	0.77	1.00
215	2.08	2.28	2.55	0.79	1.01
205	2.12	2.30	2.55	0.83	1.02
195	2.18	2.34	2.55	0.85	1.04
185	2.22	2.39	2.61	0.87	1.04
175	2.22	2.44	2.67	0.87	1.05
165	2.27	2.44	2.67	0.91	1.05
155	2.29	2.49	2.61	0.94	1.06
145	2.32	2.54	2.67	0.95	1.06
135	2.37	2.59	2.67	0.96	1.05
125	2.42	2.59	2.79	0.97	1.08
115	2.47	2.62	2.79	0.99	1.09
105	2.47	2.62	2.92	1.01	1.09
95	2.53	2.68	2.99	1.02	1.08
85	2.55	2.71	2.85	1.03	1.10
75	2.55	2.77	2.99	1.04	1.11
65	2.61	2.77	2.99	1.07	1.15
55	2.61	2.81	3.08	1.08	1.15
45	2.68	2.84	3.15	1.09	1.18
35	2.68	2.84	3.15	1.10	1.19
25	2.70	2.86	3.23	1.11	1.20

Table B.3: Hydrous Ramp Up

Temp	Vp 0	Vp 45	Vp 90	Vs 0	Vs 90
18.00	2.44	2.67	3.12	1.04	1.29
25.00	2.44	2.67	3.11	1.03	1.28
35.00	2.41	2.64	3.11	1.02	1.27
45.00	2.39	2.61	3.00	1.01	1.26
55.00	2.36	2.61	2.97	1.00	1.24
65.00	2.32	2.56	2.97	0.99	1.23
75.00	2.29	2.56	2.95	0.98	1.23
85.00	2.29	2.51	2.93	0.98	1.22
95.00	2.25	2.46	2.86	0.97	1.21
105.00	2.25	2.46	2.86	0.96	1.21
115.00	2.23	2.46	2.83	0.94	1.21
125.00	2.16	2.39	2.79	0.93	1.21
135.00	2.14	2.37	2.76	0.91	1.21
145.00	2.12	2.37	2.74	0.89	1.19
155.00	2.10	2.32	2.71	0.87	1.19
165.00	2.09	2.28	2.65	0.86	1.18
175.00	2.05	2.28	2.63	0.84	1.17
185.00	2.01	2.24	2.62	0.84	1.16
195.00	1.98	2.20	2.57	0.82	1.16
205.00	1.95	2.17	2.49	0.80	1.16
215.00	1.93	2.09	2.52	0.77	1.12
225.00	1.87	2.08	2.49	0.76	1.12
235.00	1.82	1.99	2.37	0.75	1.12
245.00	1.81	1.99	2.35	0.72	1.11
255.00	1.74	1.89	2.29	0.68	1.10
265.00	1.69	1.86	2.27	0.66	1.10
275.00	1.62	1.81	2.23	0.64	1.09
285.00	1.58	1.77	2.11	0.64	1.09
295.00	1.53	1.74	2.09	0.63	1.08
305.00	1.49	1.66	2.14	0.62	1.07
315.00	1.46	1.58	2.10	0.62	1.06
325.00	1.42	1.57	2.07	0.61	1.06
335.00	1.38	1.49	2.03	0.60	1.05
345.00	1.35	1.41	1.99	0.59	1.04
355.00	1.29	1.38	1.96	0.58	1.03
365.00	1.28	1.34	1.92	0.57	1.03

Table B.4: Hydrous Cool Down

Temp	Vp 0	Vp 45	Vp 90	Vs 0	Vs 90
365.00	1.15	1.13	1.86	0.37	0.65
355.00	1.09	1.14	1.89	0.38	0.65
345.00	1.10	1.16	1.93	0.34	0.69
335.00	1.13	1.17	1.97	0.35	0.72
325.00	1.15	1.19	2.01	0.34	0.75
315.00	1.15	1.21	2.05	0.31	0.79
305.00	1.15	1.23	2.09	0.28	0.82
295.00	1.21	1.26	2.12	0.31	0.85
285.00	1.25	1.29	2.16	0.31	0.89
275.00	1.27	1.32	2.19	0.29	0.92
265.00	1.31	1.35	2.19	0.28	0.96
255.00	1.35	1.39	2.25	0.29	0.97
245.00	1.38	1.43	2.40	0.29	1.01
235.00	1.45	1.47	2.40	0.38	1.01
225.00	1.47	1.51	2.40	0.36	1.10
215.00	1.53	1.56	2.40	0.37	1.15
205.00	1.54	1.61	2.45	0.39	1.15
195.00	1.59	1.66	2.50	0.43	1.17
185.00	1.63	1.71	2.50	0.46	1.17
175.00	1.71	1.70	2.61	0.50	1.21
165.00	1.75	1.81	2.67	0.52	1.23
155.00	1.81	1.87	2.79	0.58	1.34
145.00	1.89	1.96	2.79	0.66	1.46
135.00	2.02	2.03	2.79	0.79	1.48
125.00	2.08	2.12	2.83	0.85	1.45
115.00	2.19	2.20	2.86	0.90	1.46
105.00	2.26	2.27	2.86	0.97	1.46
95.00	2.33	2.36	2.86	1.05	1.51
85.00	2.39	2.45	2.89	1.08	1.54
75.00	2.44	2.48	3.00	1.13	1.57
65.00	2.56	2.53	3.00	1.23	1.61
55.00	2.56	2.62	3.03	1.20	1.63
45.00	2.66	2.71	3.07	1.28	1.69
35.00	2.69	2.81	3.12	1.30	1.69
25.00	2.70	2.82	3.24	1.31	1.72